Fluctuations in Au+Au collisions at $\sqrt{s_{NN}} = 200\,\mathrm{GeV}$

Christian Holm Christensen

February, 2003

Niels Bohr Institute
University of Copenhagen

Supervisor:		Censor:	
Jens Jørgen Gaardhøje		Hans–Åke Gustafsson	
	Niels Bohr Institute		Lund University
	Blegdamsvej 17		Department of Physics
	DK–2100 København Ø		Box 117
			SE–221 00 Lund.

Contact information:

Home:	Sankt Hansgade 23, 1^{th}	Institute:	Niels Bohr Institute
	DK–2200 København N		Blegdamsvej 17
			DK–2100 København Ø
	(+45) 35 35 96 91		(+45) 35 32 53 05
Email:	`cholm@nbi.dk`	Homepage:	`http://www.nbi.dk/~cholm`

This document is set by LaTeX, using Computer Modern Fonts.
Figures are created in XFig `http://www.xfig.org` and ROOT `http://root.cern.ch`.

Preface

During the spring semester of 1998, Nille Klausen, Troels Petersen, and I wrote our bachelor thesis on particle spectra measurements in BRAHMS. We tried to estimate how much beam was needed at BRAHMS to make a inverse slope analysis. This brought me into the field of scientific programming[1] by accident, and the BRAHMS experiment in particular.

In the summer of 1999, I spent a month at Brookhaven National Laboratory laying down the ground work for the BRAHMS databases. The work on this large–scale project carried on well into the early spring of 2000[2]. During that work, I got acquainted with state–of–the–art, C++ based, scientific programming tool and analysis framework ROOT.

It was therefore a great pleasure to have René Brun and Federico Carminatti, the creator and a major developer of ROOT, assigned as my supervisors during my 11 week summer student stay at CERN during the summer of 2000. There, I worked on statistical data analysis tools to be used in the ALICE experiment at the LHC which will start collisions of $p+p$ at $\sqrt{s_{NN}} = 4\,\mathrm{TeV}$ in 2007, and Pb+Pb at the same energy in 2008.

From the fall of 2000 and onward, my time has been split between data analysis and development and maintenance of the BRahms Analysis Toolkit (BRAT). The BRAHMS collaboration is small, no more than 60 person all in all, but the amount of code unfortunately does not scale with the number of people but rather with the complexity of the experiment. The development and maintenance of BRAT has therefore taken up a large portion of my time the past 1½ year.

This thesis presents an attempt at measuring fluctuations in Au+Au at $\sqrt{s_{NN}} = 200\,\mathrm{GeV}$ using BRAHMS. The amount of fluctuations in the number of produced charged particles per source in the hot and dense fireball produced at RHIC is extract from the data in an fairly simple model that does not depend on some rather difficult conversion from energy deposited by charged particle in the detectors to the actual number of particles hitting the detector. Unfortunately, the BRAHMS experiment is not well–suited for this kind of measurement, as will be shown in this work.

The document is structured as follows: Chapter 1 contains a brief description of the Standard Model, and confinement and chirality in QCD. Chapter 2 introduces the experimental methods used to probe the QCD, and summarises various proposed signatures of the Quark Gluon Plasma (or deconfined, chiral symmetric phase of QCD). Chapter 3 describes the underlying theoretical considerations of fluctuations in relativistic heavy ion collisions. Chapter 4 gives an overview of the RHIC accelerator and describes the BRAHMS detector. There is also a section of the software used in BRAHMS. Chapter 5 presents the analysis in this work. Chapter 6 is dedicated to simulation studies of the fluctuations in Au+Au at BRAHMS. Chapter 7 presents an attempt to extract the fluctuations in particles produced per source, by fitting the observed data to the theoretical formula. Finally, Chapter 8 summarises the work. The appendices gives various details, and there is a glossary and index of terms an abbreviations at the end of the document.

[1] Back then, BRAHMS was still using Fortran77

[2] See also Section 4.5.

Thanks to everyone.

Christian Holm Christensen
Copenhagen, February 2003

Contents

List of Figures

List of Tables

Chapter 1

Introduction

1.1 The Standard Model

The Standard Model, or SM, is the name physicists have given to the collection of beliefs and theories that we in physics currently believe to describe the world best. It is the framework within and from which the physicist works.

The SM describes almost all forces of nature as interactions between fundamental particles, mediated by other fundamental[1] particles. The particles and interactions are described in terms of quantum fields, that have all the characteristics of quantum objects e.g., they behave like both particles and waves.

One way to envision this, is to think of a bath of water; if one throws in a pebble, a blob will form where the pebble hits the surface, and rings of waves will propagate out from that point — the bath has been excited. Likewise, one can think of the universe as consisting of 'baths' or rather fields, and where a 'pebble' or rather energy, was thrown in one has a quantum particle — the quantum field has been excited. Interaction between particles then take place in these and other fields.

The fundamental particles are divided into *quarks* and *leptons*, and all interactions between these particles are mediated by *gauge bosons*. Table 1.1 lists the particle zoo in brief. For every particle species, there exists an *anti*–particle species, which is the same as the particle, except for a flip of sign for any kind of charge the particle may have. Anti–particle are commonly denoted by a bar over the particle name, or a flip of sign of the superscript sign. So the anti particle to the u quark is an anti–u, written $\bar{u}$, to d the $\bar{d}$, and to e^- the positron e^+.

However, SM has not been able to explain gravity in terms of quantum fields, and there still exists a schism between quantum field theory and general relativity — the theory of gravity.

Quarks are the building blocks of the nucleons, the constituents of the atomic nucleus, and many other more rare particles. Since most of the atoms mass is concentrated in the nucleus, the quarks make up most of the known matter in the universe. Generically, the particles made up of quarks are called *hadrons*.

The particles containing 3 quarks are called *baryons*, and include the nucleons i.e., the much familiar proton (p) and neutron (n). Other examples of more exotic and heavier baryons are Deltas (Δ^{++}, $\Delta^{\pm}$, Δ^0), Lambdas (Λ), and Sigmas ($\Sigma^{\pm}$, Σ^0). However, of the baryons only p is stable[2], and the n is only stable when bound inside the atomic nucleus , hence only n and p is found in abundance in nature.

Particles made of a quark and an anti–quark are called *mesons*, and the interactions of

[1] The term *fundamental* should not be taken too literally; rather the term should be understood as 'fundamental within the standard model, but not necessarily fundamental to Nature.'

[2] p's lifetime is $> 10^{32}$ year, longer than the age of the universe.

Quarks			*Gauge bosons*	
u	c	t	γ	Electromagnetic
d	s	b	$Z, W^{\pm}$	Weak
Leptons			g	Strong
e^-	μ^-	τ^-	graviton†	Gravity
ν_e	ν_μ	ν_τ		

Table 1.1: The standard model particle zoo in brief. †As mentioned, no satisfactory quantum theory for gravity has yet been formulated, and no graviton has been observed in experiment, so therefore the inclusion of the graviton in the zoo is dubious.

baryons can to a large extend be described in terms of these. Mesons include Pions ($\pi^{\pm}$, π^0), Kaons ($K^{\pm}$, K^0, $\overline{K^0}$), and Phis (ϕ). Mesons are short–lived objects and therefore only exists in nature in extreme circumstances, such as in cosmic rays[3]. Table 1.2 summarises some properties of the lightest hadrons.

Particle	*Mass*	*Quark contents*	*Electric Charge*	*Lifetime*
π^+	0.140 GeV	$u\bar{d}$	+1	2.6×10^{-8} s
π^0	0.135 GeV	$\frac{1}{\sqrt{2}}\left(u\bar{u} - d\bar{d}\right)$	0	8.4×10^{-17} s
K^+	0.494 GeV	$u\bar{s}$	+1	1.2×10^{-8} s
K^0	0.498 GeV	$d\bar{s}$	0	0.9×10^{-10} s or 5.2×10^{-8} s
p	0.938 GeV	uud	+1	$> 1.6 \times 10^{32}$ year
n	0.940 GeV	udd	0	887 s
Λ	1.115 GeV	uds	0	2.6×10^{-10} s

Table 1.2: Some hadrons and some of their properties. Only particles are listed — anti–particles are obtained by quark conjugation (for example, the π^- is a $\bar{u}d$ system). Values are taken from [1].

To the leptonic family belongs the familiar *electron* (or e^-), which determines the chemical properties of atoms. There exists two other electron–like particles in the lepton family, the Muon μ and Tau τ, along with three companion particles ν_e, ν_μ, ν_τ, called neutrinos.

1.2 Confinement

*Q*uantum *C*hromo*D*ynamics, or QCD for short, is the theory that describes how *coloured* objects, such as the quarks interact. In QCD, the coupling between the coloured objects are mediated by the gauge boson called the *gluon*. Gluons themselves are coloured, which means that gluons can interact, or couple to one another. This property of QCD, make it radically different from the rest of the theories describing interactions between particles. In particular, the interaction of gluons gives rise to what is known as *confinement*.

As quarks are moved farther and farther apart, it costs more and more energy (see Figure 1.1(a)), since the force[4] is non–vanishing. The textbook analogy is that of a rubber band

[3] The radiation from the universe constantly bombarding the earth, mainly from interactions in the upper layers of the atmosphere.

[4] $F = -\frac{dV}{dr} = -k \approx 1\,\text{GeV/fm}$

— stretching a rubber band requires increasingly more energy. Just as a rubber band will eventually break if stretched too far, so will the interaction of two coloured objects, when moved farther apart, eventually 'break'. What happens is, that as the two objects become more distant, at a certain distance enough energy will be present in the colour field to form a new quark–antiquark pair i.e., a meson.

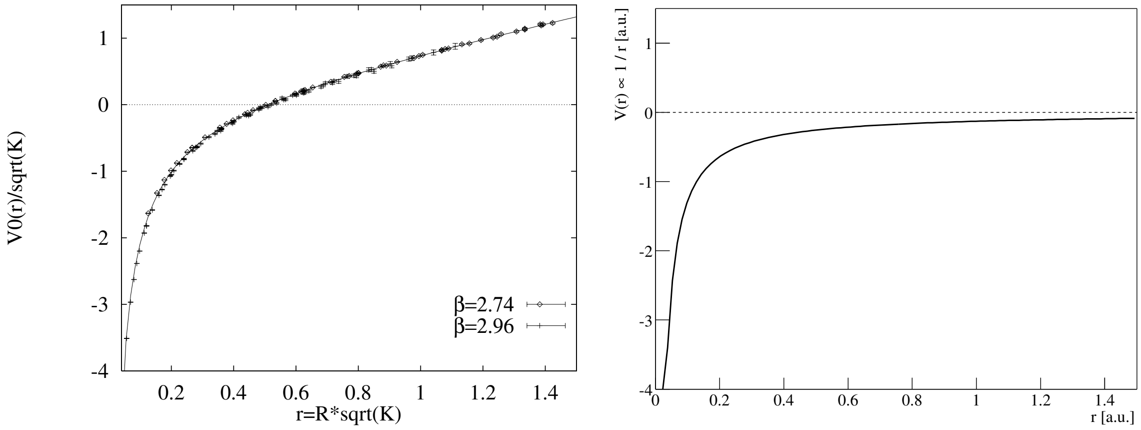

(a) (b)

Figure 1.1: (a) The heavy quark–quark potential, from Lattice QCD. K is the string tension, a theoretical parameter. From [2]. For comparison, (b) show an $1/r$ potential.

This is what is meant by confinement. The quarks in a baryon or meson may never escape the other quarks. This has the unfortunate effect that we can not hope to study the properties of a free i.e., non–interacting, quark [3]. The fact that no coloured particles have been observed in nature, supports this view. A net charged coloured object would allows us to study QCD in more details, however it is as if the rubber band breaks because the colour charge can not exist on localised objects.

This is in contrast to for example Quantum Electro$D$ynamics (QED), that concerns interaction of electric electrically charged particles. In QED, the field boson, the photon (γ) is not itself electric charged, and so γ's can not couple to one another.

The forces of QED (and more generally Quantum Electro$W$eak$D$ynamics, or QWD), and the much familiar force of gravity, lessens with the distance between the interacting particles. For example, it get easier and easier i.e., does not cost as much energy, to remove a rock from the gravitational field of another (larger) body e.g., earth.

In fact, the rubber band analogy can be extended even further. If the two ends of a rubber band are moved close to one another tension in the band disappears, and the two ends do not feel each other. For quarks this is also true. If two quarks are close to one another, the interaction between them is small — if moved really close, they essentially do not interact at all — in a sense they become free, which is termed *asymptotic freedom* [3, 4].

1.3 The QCD Phase Transition and Chiral Symmetry

As hadronic matter is heated and compressed, the interactions between the quarks become stronger, and the typical momentum transfers become very large on very short distances. At a critical temperature T_c the quarks are expected to become deconfined, due to the asymptotic freedom of QCD. In such a state of very dense and very hot quarks, it is expected that quarks an gluons essentially do not interact. Lattice QCD (LQCD) calculations show a sharp increase in the energy density ε, and a more modest growth in pressure P, motivating the idea of a phase transition from hadronic, or confined, matter to a deconfined state. See also Figure 1.2(a). Note however, that LQCD calculations have until recently only been possible at zero baryon chemical potential $\mu_b = 0$ i.e., an equal amount of baryonic and anti–baryonic matter is present. Recently Fedor and Katz [5] have been able to extend LQCD into $\mu_B \neq 0$.

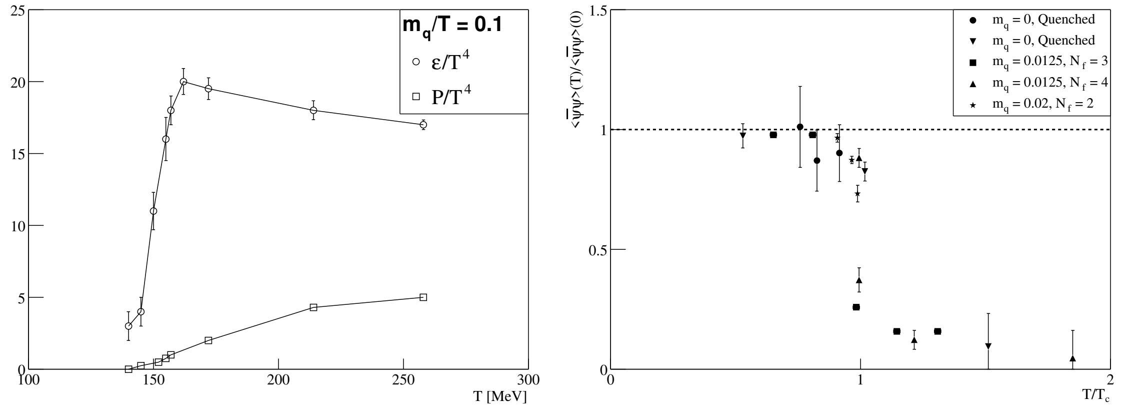

(a) (b)

Figure 1.2: (a) Lattice QCD calculations of energy density ε and pressure P as a function of temperature T, with only two flavours of light quarks (u and d quarks). The critical temperature T_c is here $\approx 150\,\mathrm{MeV}$. Adapted from [6]. (b) Lattice QCD calculation of the quark condensate $\langle\bar{\psi}\psi\rangle$ for various number of quark flavours (N_f) and masses (m_q). Adapted from [7].

In QCD, the symmetry of *chirality* is broken both explicitly and spontaneous. Chirality is the *handedness* of a particle, or the sign of the projection of the spin vector onto the momentum vector of the particle. If the projection of the spin is aligned to the momentum, the particle is said to be right–handed, while if the projection of the spin is anti–aligned, the particle is said to be left–handed.

In QCD, chiral symmetry exists as an approximate explicitly broken symmetry in the limit of massless, or noninteracting quarks (see also Section 2.3.3). The explicit breaking occurs because the quark masses are not exactly zero. However, when the quarks do interact and become confined to the nucleon or meson, the chiral symmetry is spontaneously broken.

The fact that chiral symmetry is broken means, that the π mesons have very low mass, but distinct masses for the π^0 and $\pi^\pm$. However, if the nuclear matter is heated above a critical temperature T_c and/or compressed above a certain density ρ_c, chiral symmetry is expected to be restored (see Figure 1.3). The effects of restoring the symmetry are that the π mesons have degenerate mass. The measure of chirality is the expectation value of the *quark–condensate*[5] $\langle\bar{\psi}\psi\rangle$, or the content of quarks and antiquarks in the vacuum in the nucleon. For low temperatures and low densities $\langle\bar{\psi}\psi\rangle$ is high, meaning that the nucleon vacuum is highly

[5]The vacuum expectation value of a quark–antiquark system. ψ is the quark field, and $\bar{\psi}$ is the anti–quark field.

filled with virtual quarks that interact with the regular (or valence) quarks of the nucleon, but it is expected to drop above the critical temperature T_c [8] (see also Figure 1.2(b)). Section 2.3.3 deals with the possible chiral symmetry restoration in relativistic heavy ion collisions.

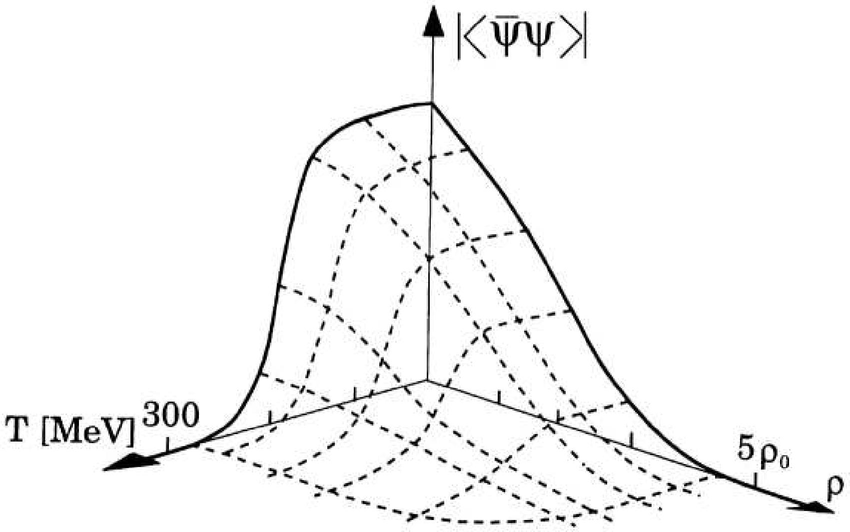

Figure 1.3: $\langle\bar{\psi}\psi\rangle$ as a function of density ρ and temperature T.

The onset of deconfinement and chiral symmetry restoration is expected to occur at roughly the same temperature [9].

If such as phase transition from chiral asymmetric and confined matter does exist, and it can be measured in experiments, it could tell us a lot about the relatively unknown QCD. Therefore hadron colliders are of great interest in these years. The idea is to squeeze the nucleons or nuclei close together to form a hot fireball where the quarks are essentially free to move in a chiral symmetric soup of quarks and gluons — a *Q*uark–*G*luon *P*lasma, or QGP for short.

Chapter 2

Searching for the Quark–Gluon–Plasma

In this chapter, some concepts important in relativistic heavy ion collisions are introduced, and various signatures of the formation Quark–Gluon–Plasma are reviewed.

2.1 Relativistic Heavy–ion Collisions

By colliding heavy ions ($A \gg 1$, A is the atomic weight of the ion) one hopes to achieve energy densities ε, temperatures T, and matter densities ρ above the critical values for the formation of the QGP. Such experiments have been carried out at the *A*lternating *G*radient *S*ynchrotron (AGS) at *B*rookhaven *N*ational *L*aboratories (BNL), *S*uper *P*roton *S*ynchrotron (SPS) at European Organisation for Nuclear Research (CERN), and are currently being carried out at the *R*elativistic *H*eavy *I*on *C*ollider (RHIC) at BNL, and from 2008 will be done at the *L*arge *H*adron *C*ollider (LHC) at CERN. Table 2.1 tabulates various characteristics of the four accelerators. Figure 2.1 shows the trajectories of the various accelerators in phase diagram of nuclear matter.

Accelerator	*Location*	*Length*	$\sqrt{s_{NN}}$	*Type*
AGS	BNL	800 m	5.2 GeV	fixed–target
SPS	CERN	7 km	17 GeV	fixed–target
RHIC	BNL	4.6 km	200 GeV	collider
LHC	CERN	27 km	4 TeV	collider

Table 2.1: Relativistic heavy–ion accelerators.

$\sqrt{s_{NN}}$ is the amount of energy per nucleon available in the centre of mass system of the collision (see also Appendix A). In a collider such as RHIC and LHC it is just the sum of the energy of the two colliding beams, divided by the number of the particles in the beam.

The work at hand deals with data obtained from the gold on gold (Au+Au) $\sqrt{s_{NN}} = 200$ GeV run of RHIC, collected during the summer of 2001 by the BRAHMS experiment. More will be said about RHIC in Section 4.1.

2.2 Collider Physics

In a collider experiment, two beams of charged particles are accelerated by a magnetic field in opposite directions, and brought to collide at fixed locations. Most colliders are ring shaped

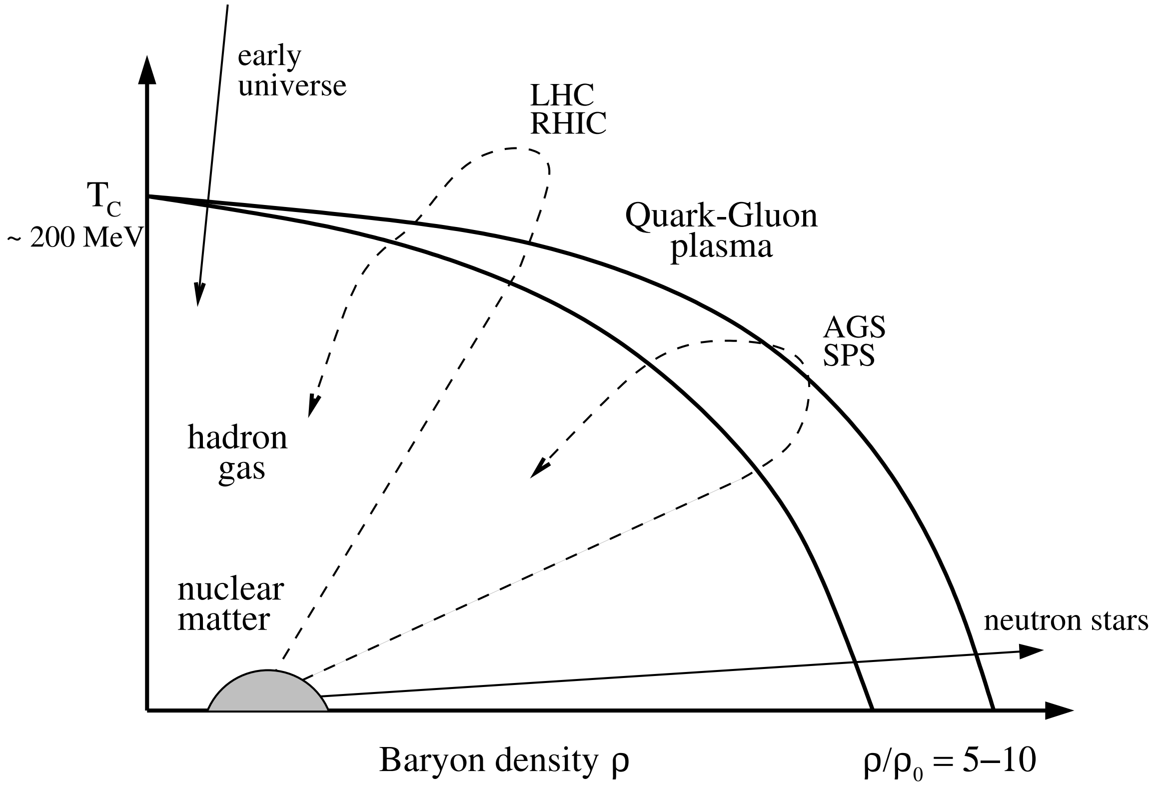

Figure 2.1: The phase diagram of nuclear matter. The arrows indicate how different colliders and natural phenomenon probes the QGP phase.

with one or two beam pipes, but some colliders have other shapes[1]. Often, the beams consists of like particles, so that at the collision point there is no net momentum in the laboratory frame. This means that all of the energy of the colliding beams can in principle be used for particle production, etc.. This should be compared to *fixed target* experiments, where a single beam is accelerated and then shot at a stationary target. In that case, there is a net momentum in the laboratory frame, which can not be used in processes.

When the beams consists of nucleons, such as n or p one speaks of N+N collisions, and if the the beams consists of nuclei, like lead (Pb) or gold (Au) one speaks of A+A collisions. In high energy particle physics collisions of e^- and e^+ have been the system of choice for the past 10 or so years at LEP at CERN due to its relative cleanness. However, to probe new regions of QCD, particle physics will start doing $p + p$ collisions at LHC in the year 2007.

Collisions are characterised by the amount of energy available in the centre of mass frame of the collision, denoted by $\sqrt{s}$, which for symmetric collisions in a collider is equal to $\sqrt{s_1^2 + s_2^2}$ (the root of the sum of the square kinetic energy of the two colliding particles). In A+A one often uses centre of mass energy per nucleon $\sqrt{s_{NN}} \equiv \sqrt{s}/2N$ where N is the number of nucleons in each of the colliding nuclei.

2.2.1 Impact Parameter, Participants and Spectators

When colliding particles of non–vanishing size, like nuclei, the two colliding particles can have varying size of overlap zones. The area of the overlap is determined by the *impact parameter* b, and measures the overlap radius in fm, as shown in Figure 2.2.

[1]For example SLAC in Stanford, California, USA.

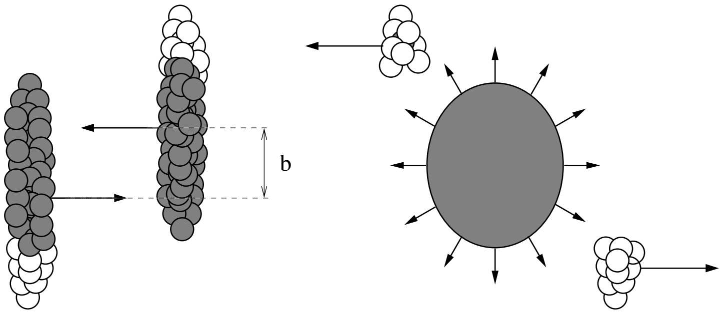

(a) (b)

Figure 2.2: (a) Impact parameter in heavy ion collisions. (b) Spectators and participants.

Because the radius of an ^{197}Au nucleus is approximately 8 fm [10], one finds that $b \in [0, 16]$fm in Au+Au, where $b = 0$ fm corresponds to a head–on, or central, collision, and $b \gtrsim 10$ fm corresponds to grazing, or peripheral, collisions.

As can be seen from Figure 2.2 the colliding nucleons may be categorised into two groups: the *participant* and the *spectator* nucleons. The participants are the nucleons that scatter, or interact in the collision, while the spectators essentially go on unaffected by the collision, and do not contribute to the particle production.

The impact parameter is not a directly measurable quantity — instead one characterises the overlap of the collisions partners by *centrality*. More will be said about centrality in Section 5.3. However, the number of participants as a function of b can be estimated using various models of the nuclear density distribution. Figure 2.3 shows the number of participants in Au+Au as a function of the impact parameter from the HIJING event generator [11, 12].

2.2.2 Transparency and stopping

Often the colliding particles are accelerated to speeds that are a considerable fraction of the speed of light, and so the collisions must be treated relativistically. At RHIC, for example the Au nuclei travel at a speed of approximately 99.995 % of the speed of light, corresponding to $\gamma = 100$. That has the effect that distances in the direction of the velocity, as seen from the laboratory frame and the rest frame of the opposing nucleus, becomes shorter than in the rest frame of the Au nucleus by $\frac{1}{\gamma}$. Hence the Au nuclei, as seen from the centre of mass system, become flat like pancakes; they are Lorentz–contracted.

Due to baryon–conservation, the net number of baryons after the collision, is the same as before. However, during the collision, the colliding baryons and quarks may transfer momenta to each other, or form new particles. That means, that the phase space distribution of the baryons need not be the same after the collision as before.

This leads to two scenarios for the collision systematics. In the first scenario applicable for low energies ($\sqrt{s_{NN}} \approx 10$ GeV), the constituent particles of the colliding nuclei are completely stopped at the collision point. This is called *full stopping*, and is depicted in Figure 2.4. In this hot and dense fireball the nuclei will essentially overlap and possibly undergo a phase transition to deconfined and chiral symmetric matter.

The degree of stopping is the normally defined as the average rapidity loss of the nuclei's nucleons. Transparency, explained below, can then be thought of as 1 minus the degree of stopping.

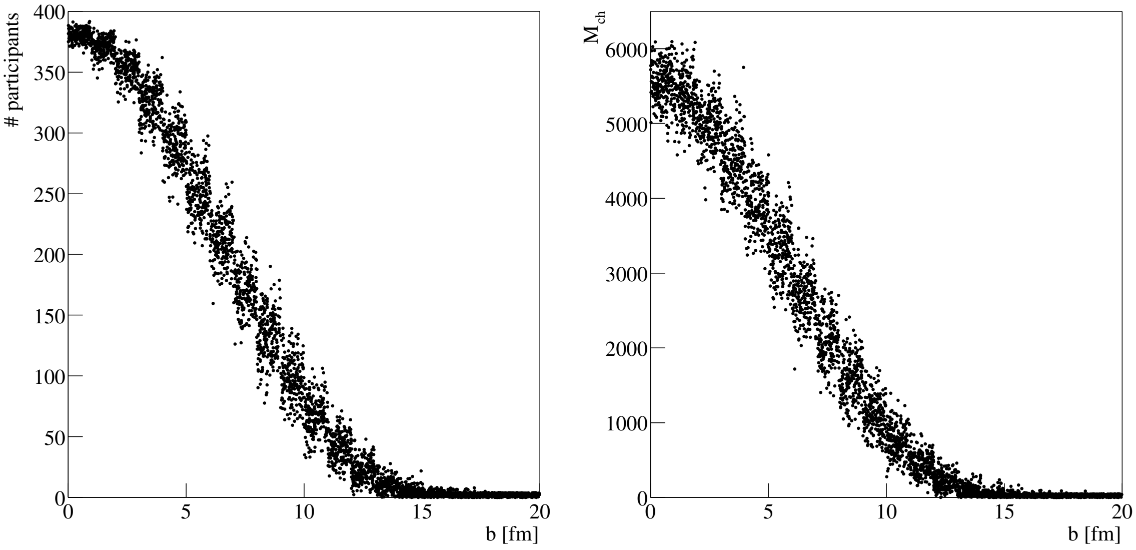

(a) (b)

Figure 2.3: Number of participants (a) and produced charged particles (M_{ch}) (b) versus b estimated from HIJING [11, 12] in Au+Au at $\sqrt{s_{NN}} = 200\,\mathrm{GeV}$.

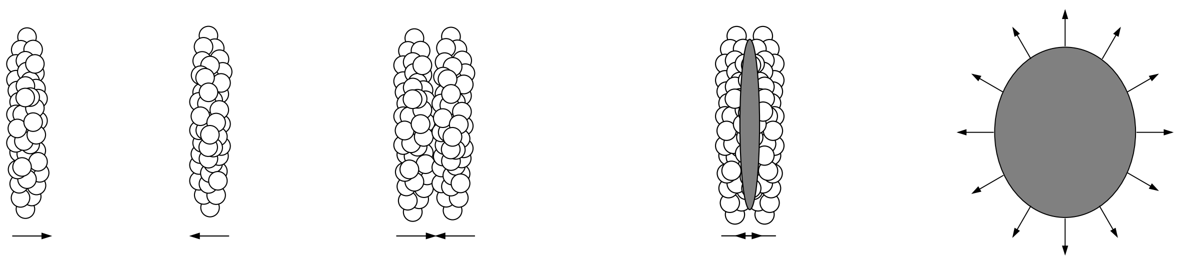

(a) (b) (c) (d)

Figure 2.4: Stopping in heavy ion collisions.

However, at higher energies, the Lorentz–contraction of the colliding nuclei limits the amount of nuclear matter the colliding nucleons (and their constituent quarks) will see during the collision. The time t needed in the rest frame of the nucleon to produce a particle follows from $\Delta E \Delta t < \hbar$ and gives $t \approx 1\,\mathrm{fm}$. In the laboratory frame this is Lorentz–dilated to $t' = \gamma t$. Due to the extremely large γ in relativistic collisions ($\mathcal{O}(100)$) $t' \approx 100\,\mathrm{fm}$; large enough that the two colliding nuclei has long since passed each other before the constituent particles can interact a second time. This is called *transparency* and is depicted in Figure 2.5.

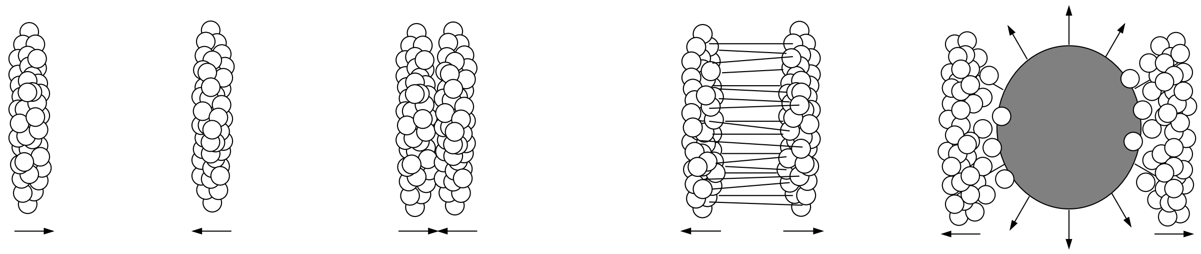

(a) (b) (c) (d)

Figure 2.5: Transparency in heavy ion collisions.

So, in effect the two nuclei become transparent to each other, and each nucleon will only interact a few times, and their constituent quarks will drag out their interaction gluons. Eventually the gluonic zone between the colliding nuclei will have such a high energy density that the colour field will break (like rubber–bands) and produce $q\bar{q}$ in a hot and dense zone, possibly forming deconfined and chiral symmetric matter.

The degree of stopping can be studied via the ratio of $\bar{p}$ to p as a function of the rapidity y. In the fully transparent scenario, the ratio becomes unity over the full range up the rapidity of the beams, due to charge, baryon, and isospin conservation in the collision. In a full stopping scenario, the ratio is affected by the collision nucleons left over in the central region ($y \approx 0$).

BRAHMS has studied this behaviour for $\sqrt{s_{NN}} = 130\,\mathrm{GeV}$ and $200\,\mathrm{GeV}$ and finds a $\bar{p}/p$ of 0.63 [13] and 0.75 [14] at $\eta \approx 0$ respectively (see also Figure 2.7), suggesting that full transparency has not been reached at RHIC energies. The AMPT model from Texas A&M [15] suggests that some rescattering takes place in the initial stages of the collision transporting beam nucleons into the central region, and thus giving a ratio $\bar{p}$ to p less than 1.

2.2.3 Chemical and Thermal Freeze–out

In relativistic heavy ion collisions where an abundance of particles are created in the initial stages of the interaction, there is amble opportunity for the particles to reinteract to produce new particles or transfer momenta.

When the particles no longer reinteract to produce new particles, the system is said to have reached *chemical freeze–out*. That is, the chemical potential of the various species, like protons, pions, kaons, and so on, does not change further, except via secondary interactions in material out of the collision zone (such as the beryllium beam pipe or iron magnets), or decays of short lived particles (such as Λ's).

However, the particles may still interact to transfer momenta. When the particles from the collision essentially no longer transfer momenta, the system is said to have reached *thermal freeze–out*. That is, the mean velocity (or temperature) of the system does not change further.

2.3 Signatures for QGP

The detection of QGP in relativistic heavy–ion experiments is unfortunately not a straight forward matter. The number of produced charged particles in gold on gold collisions at $\sqrt{s_{NN}} = 200\,\text{GeV}$ is around 5000 [16], most of which have interacted after the initial production, thereby washing out many of the characteristics of the original production in the collision. A number of *signatures* for the detection of QGP, have been proposed. An overview in the context of RHIC is given in [8].

2.3.1 Kinematics

The phase transition can be studied by the inversion of Figure 1.2(a), and the associations $T \leftrightarrow \langle p_\perp \rangle$, and $\varepsilon \leftrightarrow \frac{dN}{dE_\perp}$. The temperature is often determined as the inverse slope of the single particle spectrum [17]

$$\frac{d^3N}{dp^3} = \frac{Y}{4\pi T m^2 K_2(\frac{m}{T})} e^{-\frac{E}{T}} \quad , \tag{2.1}$$

where Y is the total yield, m the rest mass of the particle, and p is the momentum of the particles. The idea is to study this inverse slope parameter as a function of varying collision energy. However, the extraction of T and interpretation of this parameter as the temperature of the collision, is strongly dependent on the assumption that the hot fireball of the collision is in thermal and chemical equilibrium. This assumption is far from trivial, as it is questionable whether the system has the time to become equilibrated. However, if the critical temperature is high enough ($> 200\,\text{GeV}$), the thermalisation time maybe as short as $0.4\,\text{fm}$, giving ample time for reaching equilibrium [4]. The STAR experiment at RHIC has published result from the $\sqrt{s_{NN}} = 130\,\text{GeV}$ run [18], and work is underway from BRAHMS for the $\sqrt{s_{NN}} = 200\,\text{GeV}$ run.

The ratio of anti–particle to particle number, like $\frac{\bar{p}}{p}$, $\frac{K^+}{K^-}$ and $\frac{\pi^+}{\pi^-}$ as a function of rapidity, provides extensive information on the kinematics of the collision. Due to charge, baryon, isospin, strangeness, etc. conservation, particles are assumed to be produced in particle anti–particle pairs. Therefore, an excess of particles in these ratios signals that something other than pure kinematics, like pair production, is at play in the collision. The $\frac{\bar{p}}{p}$ near $y = 0$ provides information on how much of the colliding nuclei is left over in the various rapidity regions of the collision zone. All four RHIC experiments have published particle ratios from the $\sqrt{s_{NN}} = 130\,\text{GeV}$ run [13,19–21] and work is underway from BRAHMS for the $\sqrt{s_{NN}} = 200\,\text{GeV}$ run. Preliminary results from $\sqrt{s_{NN}} = 200\,\text{GeV}$ is shown in Figure 2.7 [14].

2.3.2 Dynamics

Identical particle interferometry, where one measures the correlation lengths of identical particles at the time of thermal freeze–out, can provide information on the collision zone size [22], collective flow, coalescence [23], as well as provide probes for droplet formation [24], all of which can provide insight into the dynamics of the hot fireball.

Due to the abundance of quark anti–quark pairs produced close in phase space in the heavy ion collisions, the Fermi sea for u and d quarks is expected to be quickly filled, leaving it energetically favourable to produce $s\bar{s}$ pairs. Hence the observation of strangeness enhancement, is good probe for the formation of a hot and dense phase of nuclear matter, in particular the ratios $\frac{N_{K^-}}{N_{\pi^-}}$ and $\frac{N_{K^+}}{N_{\pi^+}}$ are of particular interest. Work is underway for the $\sqrt{s_{NN}} = 200\,\text{GeV}$ from BRAHMS [14].

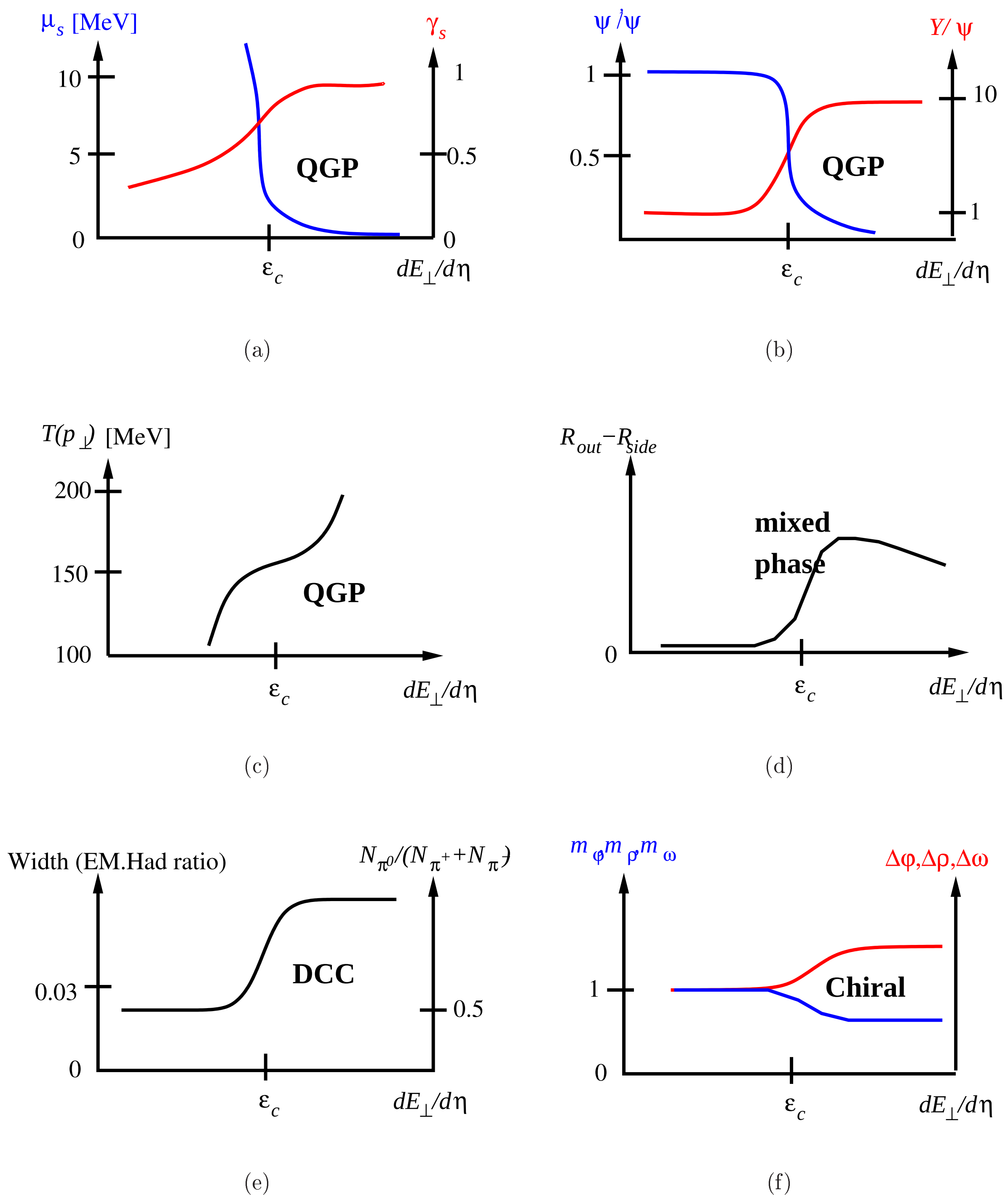

Figure 2.6: Various proposed signatures anno 1996. Adapted from [8]. (a) Strangeness enhancement. (b) Charm suppression. (c) Temperature. (d) Interferometry. (e) Disoriented Chiral Condensates. (f) Chiral symmetry restoration.

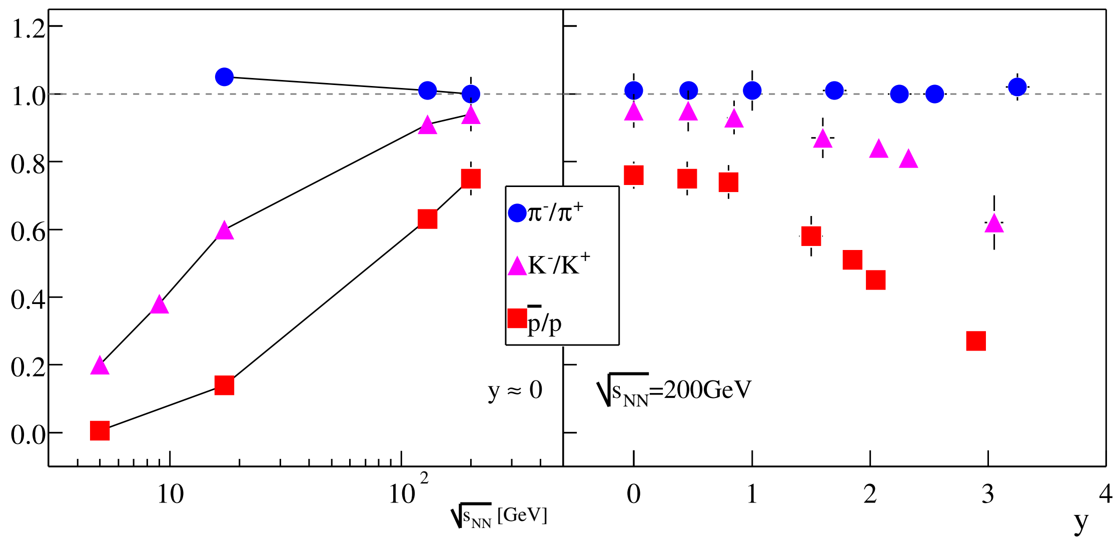

Figure 2.7: Particle ratios at $y \approx 0$ as a function of $\sqrt{s_{NN}}$ and at $\sqrt{s_{NN}} = 200\,\text{GeV}$ as a function of y

On the other hand the production of $c\bar{c}$ (charmonium) is expected to be strongly suppressed in the deconfined phase. This shows up in the suppression of the formation of J/Ψ particles. NA50 of CERN has published results to that effect [25], and it is the intend of PHENIX to look for this signal at $\sqrt{s_{NN}} = 200\,\text{GeV}$ too. However, because the J/Ψ decays into dileptons (pairs of leptons, like $\mu\ \bar{\mu}$), BRAHMS is unable to measure this signal.

Another hadronic signature of QGP that recently received a lot of attention is *jet quenching*, which shows up as a suppression of high $p_\perp$[2] particles. Preliminary results from BRAHMS indicate that this may be the case.

2.3.3 Chiral Symmetry Restoration — Disoriented Chiral Condensates

It is expected that extremely hot and dense nuclear matter, such as in QGP, will undergo (partial) chiral symmetry restoration. Figure 2.8 shows the potential in the linear sigma model [26] under various conditions. Initially, the quark matter is in the asymmetric state of spontaneous and explicitly broken symmetry, as seen in Figure 2.8(a). As the quarks become deconfined, the spontaneous broken symmetry is restored, while the explicit persists, giving a potential as shown in Figure 2.8(b). When the system cools down and becomes less dense, the symmetry is again spontaneously broken, and the potential is once again that of Figure 2.8(a).

This has some rather interesting experimentally effects. As the symmetry is partially restored, the π and ρ meson masses will change. Since the ρ meson decays into dileptons, which do not interact strongly with the surrounding nuclear matter, one can hope to measure the change in the ρ mass, by measuring the invariant mass spectrum of the dileptons. BRAHMS can not currently measure the dilepton spectra well enough for this, but PHENIX, also at RHIC, are designed to measure this. However, BRAHMS is expected to be upgraded in 2004 with a photon detector (PHOS) from ALICE, which will make these measurements possible.

Another interesting phenomenon, is *Disoriented Chiral Condensates* (or DCC) [27]. When the symmetry is again spontaneously broken, the π masses initially 'sit' on top of the local maximum of the potential, and suddenly acquire mass by seeking toward the global minimum.

[2] See Appendix A.

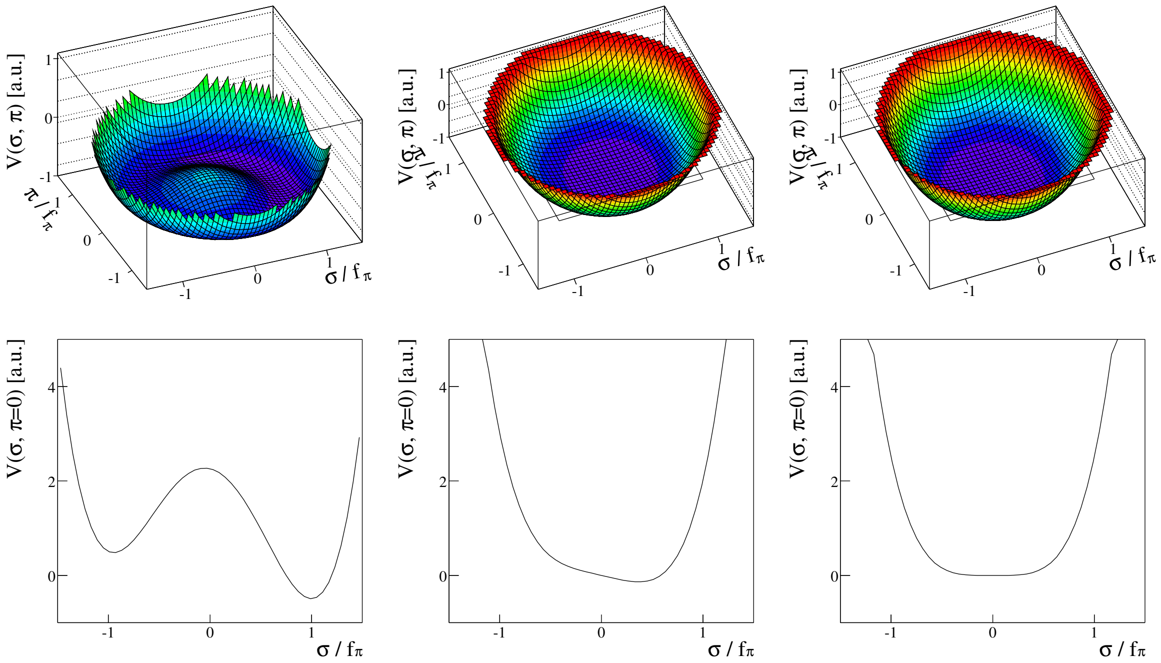

(a) (b) (c)

Figure 2.8: The potential V between particles in a linear σ model [26]. (a) The explicitly and spontaneously broken symmetry, (b) The explicitly broken and spontaneous symmetry (partial restoration), (c) fully symmetric. The lower row are the same as the upper row, with $\pi = 0$. Note that the temperature increases from left to right. The potential is shown with arbitrary units.

Since the π masses (one for $\pi^{\pm}$ and one for π^0) can get to the minimum by a variety of paths down the slope of the potential, there is no reason to believe that π mesons of the 3 different charges will be produced in equal numbers, as is the case in normal nuclear matter. One could therefore expect to see

$$\frac{\pi^0}{\pi^+ + \pi^- + \pi^0} \neq \frac{1}{3} \quad , \tag{2.2}$$

giving a clear signal of chiral symmetry restoration [8]. This can be studied be looking at fluctuations in electric charge asymmetries, such as $\frac{\pi^0}{\pi^{\pm}}$ ratios on an event by event basis.

2.3.4 Droplet Formation

As in a liquid–gas first order phase transition [28], one can expect a large density and energy fluctuations in the hadron gas (HG) to QGP phase transition, if this is of first order[3].

In a mixed phase of hadron gas (HG) and QGP, it has been conjectured that droplets of QGP will be formed, much as bubbles of air in boiling water [29, 30]. These domains of chiral symmetric and deconfined quark matter form as a consequence of a rapid expansion after the initial chiral partial symmetry restoration, and are sitting in a environment of chiral asymmetric and confined matter i.e., an entirely different background (see Figure 2.9). This picture holds equally well if the HG to QGP transition is first or second order, and somewhat for a smooth crossover.

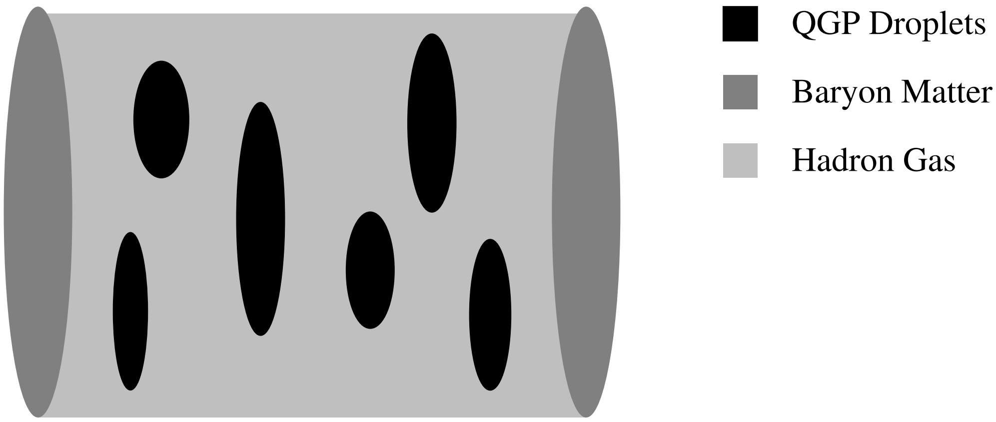

Figure 2.9: Artists view of QGP droplets in a uniform background of hadron gas. The two slabs of baryon matter are the remains of the colliding nuclei. Adapted from [29]

If such droplets are formed in relativistic heavy ion collisions, one can hope to detect these domains by studying the fluctuations of various quantities, such as multiplicity, particle specie ratios, net and gross charge, charge ratios, transverse energy and momentum.

[3]The exact order of the QGP phase transition is a matter of some controversy, but lattice QCD calculations with small u and d masses and a large s indicates a second order phase transition or a smooth crossover [29].

Chapter 3

Theory

Fluctuations in various observables has been proposed as signatures of the Quark–Gluon–Plasma. Here, the measure ω_x, where x is either the charged particle multiplicity M_{ch} or summed deposited energy E, is explored in detail, and a brief overview of other measures is given too.

3.1 Fluctuations and Event–by–Event Analysis

In the past 5 years, there is been an increasing theoretical interest in measuring fluctuations of various kinds as a good method to detect the HG to QGP phase transition in relativistic heavy ion collisions [27, 29–46]. In particular, much interest has been devoted to measures defined in terms of first and second moment of a distribution, while factorial moments, known from intermittency [27], have been less popular [36].

Andrew Jackson once proposed the following analogy why fluctuation and event–by–event analysis are of interest [36]:

> Stick a sheet of paper out of your window on a rainy day. Keeping it there for a long time — corresponding to averaging — the paper will become uniformly wet and one would conclude that rain is a uniform mist. If, however, one keeps the sheet of paper in the rain for a few seconds only, one observes the striking droplet structure of rain.

One of the motivations for studying fluctuations, is the abrupt change in the chiral order parameter $\langle\bar{\psi}\psi\rangle$ as predicted by Lattice QCD (see Figure 1.2(a)). Such discontinuities in the order parameter are generally associated with large density and energy density fluctuations [28], which one can hope to observe in relativistic heavy–ion collisions.

Also, the fluctuations[1] in the temperature and energy of a thermal system, are simply related to the heat capacitance of the system

$$\frac{s_T^2}{T^2} = \frac{1}{C_V(T)} \qquad s_E^2 = T^2 C_V(T) \qquad s_x^2 = \frac{1}{N}\sum_i^N (x_i - \bar{x})^2 \quad ,$$

which are argued to be similar to the fluctuations in $p_\perp$ [44]. The authors of that article also argue that the fluctuations of the $p_\perp$ of pions can be used as a thermometer for the system. It is important to note the above relations are defined on an event–by–event basis.

[1] Please refer to Chapter 3.2 and Appendix A for the definition of fluctuation measures.

3.2 The ω_x Fluctuation Measure

For a sample of N events, where for each event one measures N_i, $i = 1, \ldots, N$ times the variable x_{ij}, $j = 1, \ldots, N_i$, we can define the average and squared spread over all measurements over all events[2] as[3]

$$\bar{x} \equiv \frac{1}{\sum_{i=1}^{N} N_i} \sum_{i=1}^{N} \sum_{j=1}^{N_i} x_{ij} = \frac{1}{N_t} \sum_{i=1}^{N} \sum_{j=1}^{N_i} x_{ij} = \frac{1}{N_t} \sum_{i=1}^{N} N_i \overline{x_i} \tag{3.1}$$

$$s_x^2 \equiv \frac{1}{N_t - 1} \sum_{i=0}^{N} \sum_{j=1}^{N_i} \left(x_{ij} - \bar{x}\right)^2 \xrightarrow[N \gg 1]{} \overline{x^2} - \bar{x}^2 \quad , \tag{3.2}$$

where in the last part of (3.1) we have identified $\overline{x_i} = \frac{1}{N_i} \sum_{i=1}^{N_i} x_{ij}$ as the average over the measurements of a single event, and $N_t \equiv \sum_{i=1}^{N} N_i$ as the total number of measurements.

If the measurement x is made up of contributions from many particles, like for example total multiplicity M, total charged particle multiplicity M_{ch}, total charge C, net charge Q, or total transverse energy $E_\perp$, so that only one measurement of x is done in a single event, one can characterise the fluctuations in x by the ω measure[4]

$$\omega_x = \frac{s_x^2}{\bar{x}} \tag{3.3}$$

If x is measured in various bins of some other observable(s) o, like say pseudo rapidity and polar angle (η, φ) (see Appendix A) and/or centrality, one can further define

$$\omega_{x,o_i o_j} = \frac{C_{x,o_i,o_j}}{\sqrt{\overline{x_{o_i}}\,\overline{x_{o_j}}}} \tag{3.4}$$

where

$$C_{x,o_i,o_j} = \frac{1}{N} \sum_{i}^{N} \left(x_{o_i} - \overline{x_{o_i}}\right)\left(x_{o_j} - \overline{x_{o_j}}\right)$$

is the ij^{th} entry of the covariance matrix C. For $o_i = o_j$ (3.4) becomes

$$\omega_{x,o_i} = \frac{s_{x_o}^2}{\overline{x_o}} \tag{3.5}$$

It is important to realise, that this measure is *not* an event–by–event measure, as it characterises the dispersion of the variable x over the full event sample. However, the dispersion *is* of course related to the underlying physical event fluctuations, that produce the observable x.

The ω_x measure was proposed by Baym, Blättel, Frankfurt, Heiselberg and Strikman, and they have made various calculations of ω_x, including various production mechanism and smearing effects [32]. The measure has been applied to experimental data by the WA98 collaboration [47–49] to M_{ch}, multiplicity of γ-like particles, and total $E_\perp$. The measure has also been applied to NA49 data on M_{ch} [30], and more recently by Jakobsen to BRAHMS $\sqrt{s_{NN}} = 130\,\mathrm{GeV}$ data on M_{ch} [50].

---

[2] $\bar{x}$ and s_x^2 are sometimes respectively refereed to as the inclusive average and squared spread.
[3] See also Appendix A.2.
[4] Sometimes this measure is refereed to as ν or s in the literature.

3.2.1 Characteristics of ω

If the observable x is distributed according to a Poissonian probability function

$$P_\mu(x) = \frac{\mu^x}{x!}e^{-\mu} \quad ,$$

where $P(x)$ is the probability of x, and $\mu = \sigma^2$ [51] is the mean of the distribution, it is trivial to see that the measure ω_x becomes unity

$$\omega_x = \frac{\sigma^2}{\mu} = 1 \quad .$$

Hence, if the observable x is trivially distributed, one would expect ω_x exactly equal to 1.

For a binomial distribution with probability p

$$P_{n,p}(x) = \binom{n}{x} p^x q^{n-x} = \frac{n!}{x!(n-x)!}p^x(1-p)^{n-x} \quad ,$$

with mean $\mu_x = np$ and variance $\sigma_x^2 = np(1-p)$ the fluctuation become

$$\omega_x = \frac{np(1-p)}{np} = 1 - p \quad , \tag{3.6}$$

where p is the probability of obtaining x successes out of n possible.

Consider N sources, each contributing with x_i (e.g., some number of particles) to the measurement x, so that

$$x = \sum_{i=1}^{N} x_i$$

If the number of sources and the x_i of each source are independent, so that

$$\overline{x} = \overline{N}\,\overline{x_i} \quad ,$$

and if the sources are independent, so that $\overline{x_i x_j} = \overline{x_i}\,\overline{x_j}, i \neq j$, we can write

$$\omega_x = \omega_{x_i} + \overline{x_i}\omega_N \tag{3.7}$$

where ω_{x_i} is the fluctuation of the contribution for each source x, and ω_N is the fluctuation in the number of sources, where the averages and spreads are taken over all sources and all events.

3.2.2 Fluctuations in Charged Particle Multiplicity — $\omega_{M_{\mathsf{ch}}}$

Turning now to M_{ch}, Heiselberg [36] notes that the mean number of charged particles in pp collisions can be parameterised as

$$\langle M_{\mathrm{ch}} \rangle = -4.2 + 4.69\left(\sqrt{s_{NN}}\right)^{0.31} \quad , \tag{3.8}$$

integrated over all rapidities, as shown in Figure 3.1(a). KNO scaling in in high–energy ($\sqrt{s} > 2\,\mathrm{GeV}$) pp and $p\bar{p}$ collisions, means that multiplicity distributions scale with the average multiplicity. This in turn implies that all moments of the charged particle multiplicity distribution, and in particular the second moment, scale like

$$\langle {M_{\mathrm{ch}}}^q \rangle \propto \langle M_{\mathrm{ch}} \rangle^q \quad .$$

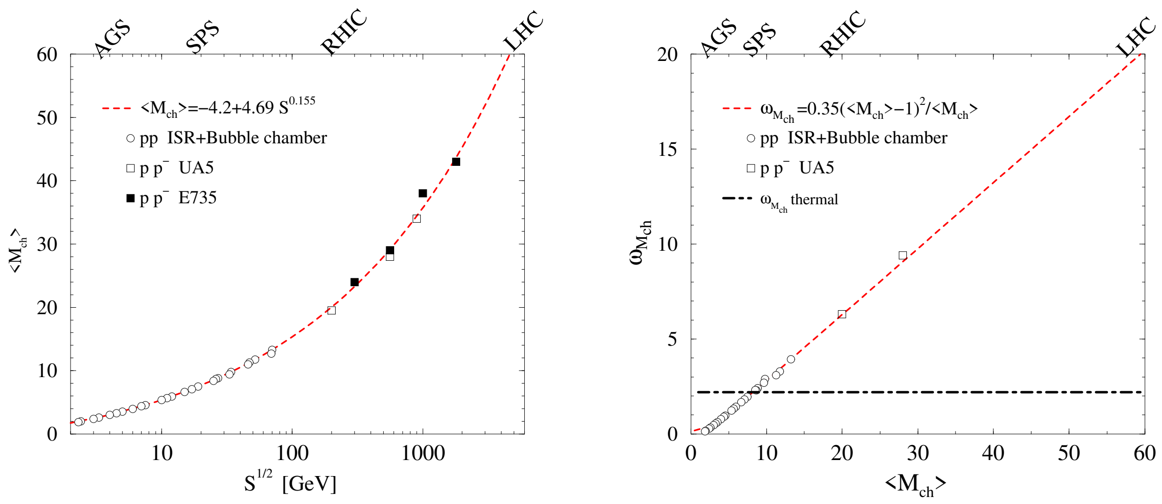

(a) (b)

Figure 3.1: (a) $\langle M_{\mathrm{ch}}\rangle$ parameterisation. (b) KNO scaling of $\omega_{M_{\mathrm{ch}}}$. Adapted from [36].

Thus the fluctuations in M_{ch}, the total charged particle production in $p + p$ collisions (or nucleon–nucleon collisions, denoted N+N), scale linearly with $\langle M_{\mathrm{ch}}\rangle$ as

$$\omega_{M_{\mathrm{ch}}} \approx 0.35\frac{(\langle M_{\mathrm{ch}}\rangle - 1)^2}{\langle M_{\mathrm{ch}}\rangle} \quad \text{for N+N collisions [36].} \tag{3.9}$$

If A+A collisions are superpositions of N+N collisions, that is, all of the physics can be explained in terms of interactions between the colliding nucleons, and no (visible) effect of the nucleons really being bound in nuclei are present, then one would expect that the fluctuations in total M_{ch} would scale as given in (3.9). Evaluating (3.8) at $\sqrt{s_{NN}} = 200\,\mathrm{GeV}$, and using that number to evaluate (3.9), leads to a prediction of

$$\langle M_{\mathrm{ch}}\rangle = -4.2 + 4.69 \cdot 200^{0.31} \approx 20 \tag{3.10}$$

$$\omega_{M_{\mathrm{ch}}} = 0.35\frac{(20-1)^2}{20} \approx 6.3 \tag{3.11}$$

for N+N collisions at $\sqrt{s_{NN}} = 200\,\mathrm{GeV}$, the current RHIC energies.

Now, supposing that in a given collision, there are n_i N+N collisions, labelled by j, each producing $m_{i,j}$ charged particles, so that the total multiplicity becomes

$$M_{\mathrm{ch}\,i} = \sum_{j=1}^{n_i} m_{i,j} \quad .$$

If the sources are independent (uncorrelated)

$$\overline{m_i m_j} = \overline{m_i}\,\overline{m_j} \quad ,$$

and the number of charged particles produced per N+N collision is independent of the number of N+N collisions, then

$$\overline{M_{\mathrm{ch}}} = \overline{m}\,\overline{n} \quad ,$$

and we can write

$$\omega_{M_{\mathrm{ch}}} = \omega_m + \overline{m}\omega_n \quad , \tag{3.12}$$

where ω_m is the fluctuation in charged particles from the individual N+N collisions, and ω_n is the fluctuations in the number of N+N collisions. Heiselberg [36] parameterises the latter as a function of participant number as

$$\omega_n = \frac{n_0}{18}\left(\frac{b_c}{2R}\right)^2 \quad , \tag{3.13}$$

where n_0 is the number of participants at $b = 0$, b_c the impact parameter at a given centrality, and R the nuclear radius. For ^{197}Au, $n_0 = 2 \cdot 197 = 394$ and $(\frac{b_c}{2R})^2 \approx 5\,\%$ this number is ≈ 1.1.

Using (3.12) it is possible, to separate out the contribution to $\omega_{M_{\mathrm{ch}}}$ that stems from sampling over a finite range of impact parameters. The point is, that with decreasing b, more and more potential sources are available, but they need not be utilised; hence ω_n may be non–zero, but (3.12) allows separating out this finite impact parameter resolution (see also Section 5.3.3).

Using an estimate of $\omega_m = 6.2$ as explained above, and the measured multiplicities at $\sqrt{s_{NN}} = 200\,\mathrm{GeV}$ [16], one finds for the 5 % most central events

$$\omega_{M_{\mathrm{ch}}} = 6.2 + \frac{1}{2}\frac{4630}{346}1.1 \approx 13.6 \quad , \tag{3.14}$$

assuming full coverage in phase–space, for Au+Au collisions at $\sqrt{s_{NN}} = 200\,\mathrm{GeV}$.

Of course BRAHMS does not cover the full phase space, but rather $\eta \in [-4.7, 4.7]$ out of roughly $[-5.9, 5.9]$. Integrating Figure 5.6 from -4.7 to 0 and estimating the size of the tail from -5.9 to -4.7 (see Figure B.7), the acceptance ratio is estimated to be 0.99, which then implies

$$1 - 0.99(1 - \omega_{M_{\mathrm{ch}}}) \approx 1 - 0.8(1 - 13.6) = 13.5$$

In the case that the particles are produced by a thermal source, where the mean number of particles in bosonic mode a is

$$\langle m_a \rangle = \frac{1}{e^{\frac{E_a}{T}} - 1} \quad ,$$

one finds [36] that the fluctuation in each state is given by

$$\omega_{m_a} = 1 + \langle m_a \rangle \quad , \tag{3.15}$$

so that the fluctuation in the total multiplicity $M = \sum_a m_a$ becomes

$$\omega_M = 1 + \frac{\sum_a \langle m_a \rangle^2}{\sum_a \langle m_a \rangle} \quad .$$

In [36] this is evaluated for a labelling momentum states of $\pi^\pm$ yielding

$$\omega_{M_\pi} = r\frac{1-r}{1+r} + (1+r)1.11 \quad ,$$

where r is the fraction of $\pi^\pm$ from resonance decays, such as $\rho \to \pi^+\pi^-$. Using an estimate of $r = 0.15$ based on the number given in [52], one obtains $\omega_{M_{\mathrm{ch}}} \approx 1.4$.

Assuming full coverage of phase space, the effect of finite impact parameter resolution is estimated as in (3.14), and gives

$$\omega_{M_{\mathrm{ch}}} = 1.4 + \frac{1}{2}\frac{4630}{346}1.1 \approx 8.8 \quad ,$$

for the 5 % most central events in Au+Au at $\sqrt{s_{NN}} = 200\,\mathrm{GeV}$. Again, correcting for the limited acceptance of BRAHMS, this gives

$$1 - 0.99(1 - \omega_{M_{\mathrm{ch}}}) \approx 1 - 0.8(1 - 8.8) = 8.7 \quad .$$

In the case of a phase transition to chiral symmetric and deconfined quark matter, the fluctuations are expected to many orders of magnitude higher than that from hadronic matter, whether the particle production is governed by KNO scaling or thermal constraints [36]. Heisenberg also notes, that the if the hadronisation of the quark matter is smooth it may very well wash out the fluctuation signal all together.

3.2.3 Fluctuations in Number of Sources — $\omega_n/\bar{n}$

The fluctuation in the number of sources, as seen by the detector, is largely determined by the range of impact parameters one samples in the analysis, and hence depends on the range of centralities used (see (3.13)). The acceptance of the η, φ bins also plays a role in this, as for small bins, very few sources will contribute to the measurement, while for larger bins, more sources are sampled.

For the present analysis[5] with $\Delta c = 1\,\% - 5\,\%$, and $\frac{\Delta\eta\Delta\varphi}{4\pi} < 6\,\%$, there is precious little room to manoeuvre in. This means that the one can expect $\frac{\omega_n}{\bar{n}}$ to be rather small. Using (3.13) for the 2 % most central, and Figure 2.3(a) for $2\bar{n}$ one get

$$\frac{\omega_n}{\bar{n}} \approx \frac{394 \cdot 0.02}{18}\frac{2}{392} = \frac{0.44}{196} = 0.002$$

Here, binary collisions between the Au nucleons is assumed, and hence a participant pair is counted as one source, explaining the factor of 2 in the last factor.

3.2.4 Fluctuations in Deposited Energy — ω_E

When a single detector element has an high occupancy — the probability that the element is hit by at least one particle in an event — the deposited energy in that detector will be a sum of the contributions from each particle impinging on the detector.

For the i^{th} event, assume that n_i sources each produce $m_{i,j}$ particles in the acceptance of a detector, or some bin in phase space, so that the total multiplicity and energy deposited in that detector becomes (i labels the event, while j labels the source and k labels the produced particle)

$$M_{\mathrm{ch}\,i} = \sum_j^{n_i} m_{i,j} \qquad\qquad E_i = \sum_k^{M_{\mathrm{ch}\,i}} e_k \quad , \tag{3.16}$$

where e_j is the energy deposited by the j^{th} particle. Following Section 3.2.1, one finds that

$$\overline{M_{\mathrm{ch}}} = \bar{n}\overline{m} \qquad\qquad \overline{E} = \overline{M_{\mathrm{ch}}}\bar{e} \quad .$$

Rearranging gives

$$\bar{e} = \frac{\overline{E}}{\overline{M_{\mathrm{ch}}}} \qquad\qquad \overline{m} = \frac{\overline{M_{\mathrm{ch}}}}{\bar{n}} = \frac{\overline{E}}{\bar{e}\bar{n}} \qquad\qquad \bar{e}\overline{m} = \frac{\overline{E}}{\overline{M_{\mathrm{ch}}}}\frac{\overline{E}}{\bar{e}\bar{n}} = \frac{\overline{E}^2}{\overline{M_{\mathrm{ch}}}\bar{e}\bar{n}}$$

[5] See Section 5.4.

Again following Section 3.2.1, the fluctuation in E can be rewritten as

$$\begin{aligned}\omega_E = \frac{s_E^2}{\overline{E}} &= \omega_e + \bar{e}\omega_{M_{\text{ch}}} = \omega_e + \bar{e}\left(\omega_m + \overline{m}\omega_n\right) \\ &= \omega_e + \frac{\overline{E}}{\overline{M_{\text{ch}}}}\omega_m + \frac{\overline{E}^2}{\bar{e}\bar{n}\overline{M_{\text{ch}}}}\omega_n = \omega_e + \frac{\overline{E}}{\overline{M_{\text{ch}}}}\left(\omega_m + \frac{\overline{E}}{\bar{e}}\frac{\omega_n}{\bar{n}}\right)\end{aligned} \tag{3.17}$$

Division by $\bar{e}$ then gives.

$$\frac{\omega_E}{\bar{e}} = \frac{\omega_e}{\bar{e}} + \omega_m + \overline{E}\frac{\omega_n}{\bar{n}}$$

Here, ω_e is the fluctuation in the energy deposited by a charged particle, ω_n is the fluctuation in the number of sources, $\bar{n}$ is the average number of sources, and ω_m is the fluctuation in the charged particle production at the sources. In this way, we can express the measured ω_E as a function of the measured $\overline{E}$ with the interesting ω_m as a parameter.

It is also worth noting, that ω_e in principle absorbs all detector inefficiencies and quirks, and fluctuations due to fluctuations in the energy loss of the charged particles impinging on the detector. The latter may come about as a result of the particles that hit the detector are not all minimum ionising (such as slow particles), or simply from the fact that the process of energy loss is a stochastic process. However, using (3.17) it is in principle possible to factor out these contributions to the measured fluctuations in the summed energy deposited ω_E, as long as the assumption of $\overline{E} = \overline{M_{\text{ch}}}\bar{e}$ and holds. That may *not* be the case, if the detector is such that it has a very long Landau tail in the energy spectrum, which will lead to a very large spread, and may hence completely dominate in (3.17).

3.2.5 Fluctuations in Energy Deposited per Particle — ω_e

The term ω_e in (3.17) — the fluctuations in energy deposited per particle impinging on the detector — is in general dependent on the momentum distribution of the charged particles, as low momentum particle deposits far more energy than a high momentum particle (see also Section 6.1.3). However, it is also dependent on the detector characteristics. In particular, it depends on the ability of resolving the energy deposited from a single particle. In an integrating detector, it is generally not possible to resolve the energy deposited from a single particle, hence leading to an additional uncertainty in the spread of the energy deposited per particle e and hence in ω_e.

3.3 Other Fluctuation measures — Φ_x

If, in the measurement x_{ij} corresponds to a single particle observable, like $p_\perp$ or $E_\perp$ one can characterise the fluctuations in that observable as

$$\Phi_x \equiv \sqrt{\frac{\overline{Z^2}}{\overline{N_i}}} - \sqrt{s_x^2} \quad , \tag{3.18}$$

where $\overline{N_i}$ is the average number of measurements of x_{ij} per event, and the mixed event–sample variables are given by[6],

$$z_{ij} \equiv x_{ij} - \overline{x} \tag{3.19}$$

$$Z_i \equiv \sum_{j=1}^{N_i} z_{ij} = N_i \left(\overline{x_i} - \overline{x}\right) \tag{3.20}$$

$$\overline{Z^2} = \frac{1}{N}\sum_{i=1}^{N} Z_i^2 = \frac{1}{N}\sum_{i=1}^{N} N_i^2 \left(\overline{x_i} - \overline{x}\right)^2 \quad . \tag{3.21}$$

In the case that x is trivially distributed (i.e., Poissonian statistics) Φ_x becomes zero. This measure of x fluctuations is a true event–by–event measure, in that it characterises the spread of the observable x in each event relative to the sample behaviour. Note, however, that the Φ_x is a *statistical* measure, and has no meaning in the limit of a few events or few measurements per event of the observable x.

The Φ_x measure was proposed by Gaździcki, Leonidov, and Roland [35] and used by the NA49 at SPS [53, 54], more recently to PHENIX $\sqrt{s_{NN}} = 130\,\mathrm{GeV}$ data [55], and STAR at RHIC proposes to use it too [56]. It has been advocated by various theorists [35, 42, 44] as a good measure when x is $p_\perp$, $E_\perp$ or the charge q, because

1. If A+A collisions are superpositions of N+N collisions, the Φ_x measure is independent of nuclear size and has a constant non–zero magnitude for all A.

2. If, on the other hand, particles are produced uncorrelated in A+A collisions, then Φ_x vanishes.

3. Since Φ_x is independent of the number of sources, if these are identical, it is insensitive to varying collision conditions, as long as the underlying production mechanism does not change.

The $\Phi_{p_\perp}$ is purely dynamical, since the statistical fluctuations have been removed by the last term in (3.18). However, for charge fluctuations Φ_q, is not very large and therefore Mrówczyński proposes another measure [42]

$$\Gamma \equiv \sqrt{\frac{\overline{Z^2}}{\overline{N_i}}} = \Phi_x + \sqrt{s_x^2} \quad ,$$

which preserves the statistical fluctuations.

Other authors [46] propose a measure that is similar to ω_x, but have the same event–by–event characteristics as Φ_x. One often seen measure is[7]

$$w_x^2 \equiv \overline{\overline{x_i}^2} - \overline{\overline{x_i}}^2 = \frac{1}{N}\sum_{i=1}^{N} \overline{x_i}^2 - \left(\frac{1}{N}\sum_{i=1}^{N}\overline{x_i}\right)^2 \equiv s_x^2 + w_d^2 \quad ,$$

where the last equal sign defines w_d^2 which is the quantity of interest. This is just the squared spread over all events of the average x per event. It is related to Φ_x as [46]

$$\Phi_x \approx \frac{w_d^2 \overline{N_i}}{2 s_x^2}$$

[6] In the literature, one often sees $\overline{z^2}$ as the last term on the right hand side, but it is evidently the same as s_x^2. Also sometimes the notation $\langle\cdot\rangle$ is used for the average over events. Here, $\langle\cdot\rangle$ is reserved for the first moment of a probability density function.

[7] This is often termed σ_x but here, σ is reserved for the second moment of a probability density function.

Unlike the Φ_x measure this measure is not invariant to number of particles produced as can be seen from the expression above. Therefore, it is sensitive to the size of the production system, or the number of sources. However, the interesting quantity w_d^2 is more easily identified, and since it is any spread that is not of statistical nature, easily interpreted.

3.4 Considerations on Fluctuation Measures

Each of the variables described above has its own domains of interest, merits and defects. The ω_x measure as used in this work, is a statistical measure. As such it only makes sense in the limit of a very large event sample. The merit of the ω_x measure lies in that x can be practically anything, including the somewhat difficult measurements owing to many particles impinging on a single detector. Of particular interest are particle multiplicities and ratios of particle numbers like $\frac{\pi^0}{\pi^+ + \pi^- + \pi^0}$, $\frac{\pi^+}{\pi^-}$ and $\frac{h^+}{h^-}$, where h is the sum over all hadron species. Also, since it is scaled by the average of the observable x, ω_x has the advantage that it is directly comparable between experiments. However, the interpretation of ω_x is not necessarily a straight forward business.

Measures like Φ_x and w_x^2 separate out the event–by–event fluctuations from the statistical fluctuations explicitly, making the interpretation much easier. However, x need to be rather well–defined for a single particle for the measures to make sense. Interesting observables are $p_\perp$, baryon or electric charge, charge ratios, and the like. Also, as [46] notes, the Φ_x is dependent on the observed multiplicity, and hence comparisons between experiments may not be straight forward. In the case of BRAHMS where there is a very limited acceptance of identified particles per event, the average over single particle observables like $p_\perp$ as used in Φ_x and w_x^2 may not be well–defined, and hence the measure is not appropriate.

3.5 Determining the Fluctuation in Particles Produced per Source

The analysis carried out by Jakobsen [50] was based on the total charged multiplicity in the TMA[8] detector of BRAHMS. In that work, Jakobsen finds that the fluctuations measured are not distinguishable from purely statistical (Poissonian) fluctuations, as shown in Figure 3.2. The very large relative error in this analysis, is reminiscent of the various corrections and transformations used in determining M_{ch}.

This work tries to take a alternate route to achieve the same goal: measuring ω_m. As the steps involved in going from read ADC counts to charged particle multiplicity becomes increasingly difficult with each step taken, this work uses the sum energy deposited in the detector[9], rather than the charged particle multiplicity. Also, the Silicon Multiplicity Array (SMA[10]), rather than the Tile Multiplicity Array (TMA) is used, as silicon has much better energy resolution than scintillating plastic.

Note also, that (3.17) depends on M_{ch}, n and e being uncorrelated. At face value, that does no seem as unreasonable assumption. However, from SPS [22, 23] and RHIC [57, 58] it is know that there is a lot of inter–particle correlations and collective movement in relativistic heavy ion collisions, rendering the assumptions non–trivial.

What (3.17) does then, is to provide the base line to compare to. That is, if the particle production in A+A collisions is a simple matter of trivial statistics, the parameterisation of

[8] See Section 4.3.1
[9] See Section 5.3.
[10] See Section 4.3.2

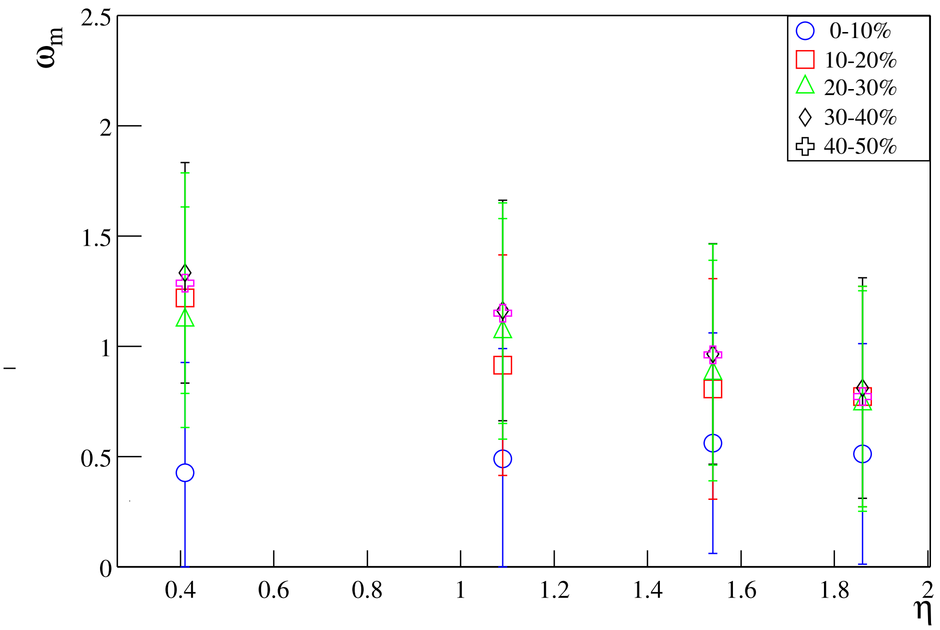

Figure 3.2: ω_m determined from the charged particle multiplicity as observed in the TMA, at $\sqrt{s_{NN}} = 130\,\text{GeV}$. The percentage shown in the legend, is the centrality cut. Adapted from [50].

(3.17) will give good results. What we are looking for in A+A collisions, when searching for QGP, is something that is *not* trivial statistics. Hence good correspondence (3.17) to data is not to be expected — the goal is to show that the simple picture of (3.17) does not hold.

Chapter 4

The BRAHMS Experiment

This chapter introduces the Relativistic Heavy Ion Collider (RHIC) at Brookhaven National Laboratories, and the BRAHMS experiment. Particular emphasis is put on the global detectors: TMA, SMA, and BB as these are the detectors used for the present work. Section 4.5 explains the database software used in BRAHMS, which was developed primary by the author.

4.1 RHIC

The RHIC accelerator is located on Long Island, USA, at Brookhaven National Laboratories, some 50 miles from Manhattan. The full complex consists of a gold ion source, a Tandem van de Graff, a booster, the AGS, and finally the RHIC storage ring. On their way to RHIC the Au ions are accelerated and stripped of electrons at various stages up to an injection energy of 10 GeV per nucleon, as indicated on Figure 4.1.

Four bunches of Au ions are split into two beams before injection into RHIC; half the bunches are sent clockwise around the ring in the blue ring, while the other half is sent counter clockwise around the ring in the yellow ring. In RHIC the bunches are finally accelerated to 100 GeV per nucleon by Radio Frequency (RF) cavities.

The beams steered by the superconducting magnets[1] of RHIC, cross each other at 6 locations around the ring, but are only steered to collide at 4 of these intersections, where the 4 RHIC experiments are located.

STAR, located at 6 o'clock, is a large cylindrically symmetric detector with a Time Projection Chamber inside a large solenoid magnet, making it an ideal detector for particle densities, ratios, and event–by–event studies in a limited region of phase space. PHENIX, at 8 o'clock, uses calorimeters and a muon arm to look at dilepton signals, as well as particle densities and ratios. PHOBOS, at 10 o'clock, is a small silicon detector experiment with 2 spectrometers with limited particle identification, and a large barrel of highly segmented detectors to measure charged particle densities, reaction plane, and possibly do event–by–event studies. BRAHMS, the second small experiment at RHIC, is located at 2 o'clock. The following section gives an overview of the BRAHMS detector.

4.2 The BRAHMS Detectors

The design goal of the BRAHMS detector is to cover a wide range in rapidity y and transverse momentum $p_\perp$, with excellent particle identification. This allows for measurement of the particle ratios, inverse slope T, and net baryon density, over a large fraction of phase space.

[1] RHIC is the first heavy ion accelerator to utilise superconducting magnets for acceleration and storage.

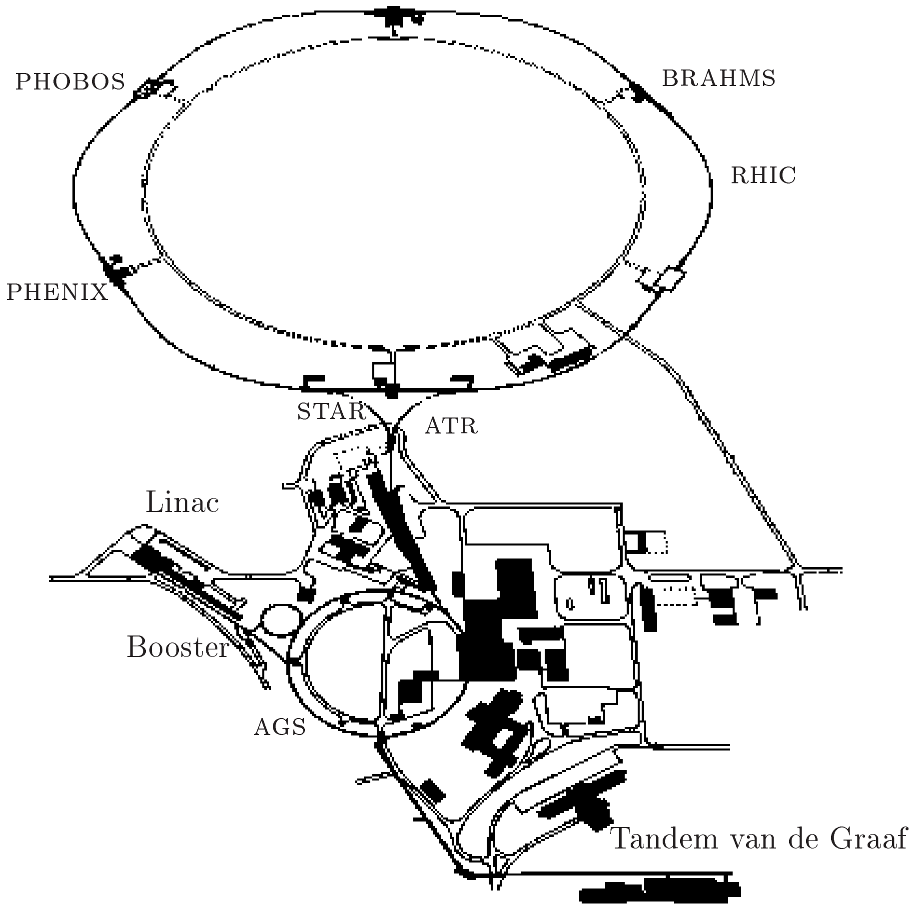

Figure 4.1: RHIC overview

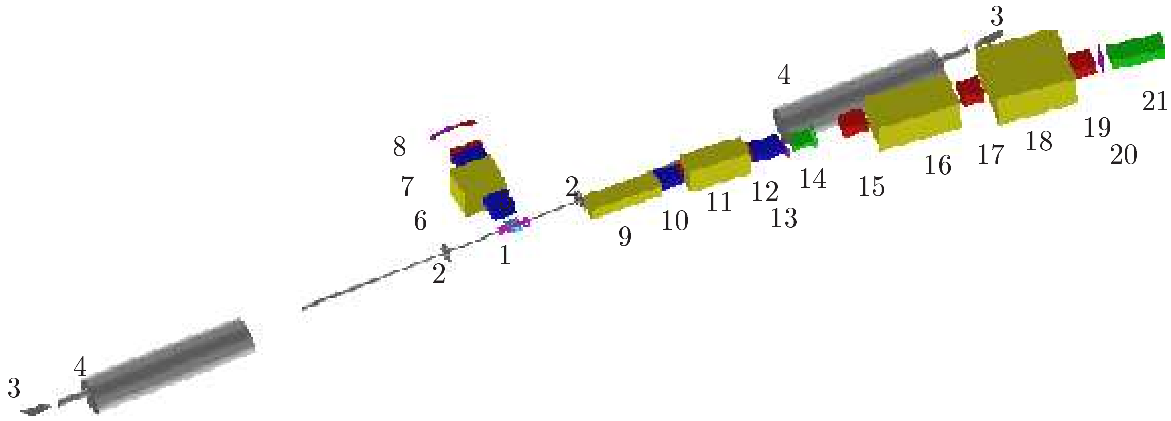

Global		*MRS*		*FFS*				*BFS*			
1	TMA & SMA, $\mathcal{O}$	5	TPM1	9	D1	13	TOF1	15	T3	19	T5
2	BB	6	D5	10	T1	14	C1	16	D3	20	TOF2
3	ZDC	7	TPM2	11	D2			17	T4	21	RICH
4	DX	8	TOFW	12	T2			18	D4		

Figure 4.2: BRAHMS overview.

The BRAHMS (*B*road *RA*nge *H*adron *M*agnetic *S*pectrometer) consists of 4 global detectors and two independent spectrometers, or rather 3 spectrometers, of which 2 are semi–independent. Figure 4.2 shows an overview of the detector.

The global coordinate system of BRAHMS is a right handed Cartesian coordinate system, with it's origin $\mathcal{O}$ at the nominal collision point (see point 1 on Figure 4.2) with the positive z axis pointing along the beam axis in the direction of the Forward Spectrometer. Hence, the positive y axis points vertically upward and the positive x axis points into the Mid–Rapidity Spectrometer.

Further, local coordinate systems are defined for each detector; their origins at the logical centre of the detector volume, the z axis lying in the xz plane of the global coordinate system pointing away from the collision point. Hence, the positive y axis points upward, as for the global coordinate system and the x is in the xz plane of the global coordinate system orthogonal to the local z axis. The transformation from the global coordinate system to the local coordinate systems is therefore given by a translation, followed by a rotation around the y axis.

Since the analysis presented here is based on only the global detectors in BRAHMS little will be said of the spectrometers.

4.3 Global Detectors

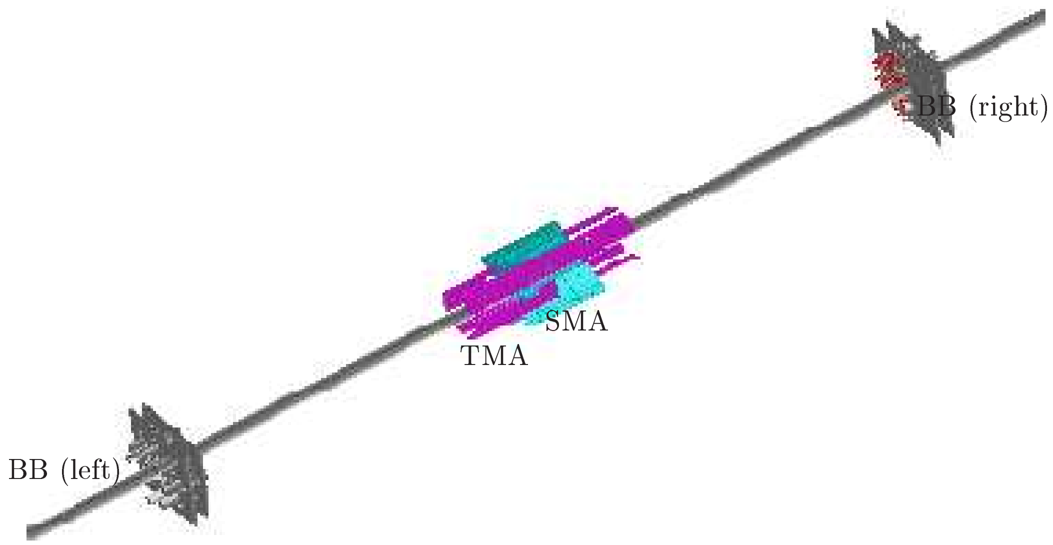

Figure 4.3: BB, TMA & SMA

4.3.1 The Tile Multiplicity Array — TMA

The TMA detector is a hexagonal barrel of scintillating plastic tiles, each 12 cm × 12 cm × 5 mm. The barrel is 1 m long, and is located at a distance of 13.6 cm from the centre of the beam line. Each side of the hexagon, a *row*, is segmented into 8 tiles, except for two of the rows which are only partially populated, so as not to put too much material, and hence sources for secondary interactions, in front of the spectrometers. Figure 4.3 shows the position of the TMA in respect to the rest of the global detectors. See also Figure 4.2, point 1, for an overview.

The TMA covers a pseudo rapidity range of $[-2, 2]$ when the interaction occurs at the nominal interaction point. However, the interactions used for the present analysis are distributed in $z \in [-20\,\mathrm{cm}, 20\,\mathrm{cm}]$, giving a larger η coverage of $\approx [-2.2, 2.2]$.

Light emitted in a tile, as a result of ionisation from the passage of charged particles, are collected in a optical fibre and sent to a *P*hoto *M*ultiplier *T*ube (PMT), where the signal is amplified, digitised and sent to the *D*ata *A*cq*uisition (DAQ) [59]. The digitised detector count is usually called the ADC count, or even just ADC. The digitised signal is then translated into a value of deposited energy, which in turn is translated into the number of particles hitting the tile in a given event, known as single detector multiplicity; see also Section 5.3 for more details.

Since the individual tiles cover a rather large portion of phase space, the mean number of particles hitting a TMA element is around 17. This makes the occupancy, or the probability that the element is hit by at least 1 particle in a given event, almost 100 %. Hence the conversion from detector count to multiplicity is far from trivial. This process will be elaborated on in Section 5.3. More information on the TMA can be found in [60].

4.3.2 The Silicon Multiplicity Array — SMA

The SMA, like the TMA, is a hexagonal barrel, positioned close to the beam pipe, inside the TMA. It consists of 25 silicon $4\,\mathrm{cm} \times 6\,\mathrm{cm} \times .3\,\mathrm{mm}$ detectors, each segmented along the z–axis into 7 active strips, giving a pitch of 0.86 cm. The detectors are placed 5.31 cm from the beam line, centred at $z = 0$, and spanning from $z \approx -22\,\mathrm{cm}$ to $z \approx -22\,\mathrm{cm}$, giving a coverage in η of approximately $[-2.5, 2.5]$, when the interactions is somewhere in $[-20\,\mathrm{cm}, 20\,\mathrm{cm}]$. The φ coverage of the SMA is similar to that of the TMA, in that the sides of the barrel that face the spectrometers are only partially occupied, to have as little as possible material in front of the spectrometers.

When charged particles traverse the silicon semiconductor, electron–hole pairs are created. An electric field across the semiconductor transports the electrons and holes to the anode and cathode, thereby inducing an electric charge on the cathode, which is then collected, and amplified by an on–board chip, and sent to the DAQ for event construction and, eventually, storage. Again, the signal from the SMA is ADC counts, which is translated into an total deposited energy signal, which maps to a charge particle multiplicity. That is, from the sum energy signal in the SMA, it is possible (at least on the average) to reconstruct the number of charged particles that hit the individual SMA elements in a given event; see also Section 5.3 for more details.

The average number of hits in a SMA is around 2.5, much lower than in the TMA (see also Figure 5.4(d)), making it an excellent detector for detecting charged particle multiplicity in a wide η and φ range. However, the occupancy is still high, around 92 %. More information on the SMA can be found in [60].

4.3.3 The Beam–Beam Counters — BB

Located at $z \approx \pm 2.2\,\mathrm{m}$ are two arrays of Čerenkov radiators, each connected to a PMT. These counters, which have intrinsic timing resolution of $\approx 50\,\mathrm{ps}$ are mainly used for triggering and timing measurements, as well as determination of the collision point, or the primary vertex' z–coordinate v_z.

The BB counters covers a η range of approximately $[\pm 3, \pm 4.3]$ for an collision at the nominal interaction point. This means that most particles hitting these detectors have $\beta \approx 1$. However, since the particle density in this region is high, good multi–hit identification for all kinds of collisions, is achieved by having two kinds of detectors; one kind with a large coverage for peripheral events, and one with small coverage for central events.

For the work at hand, Section 5.2 gives more details on the primary vertex determination using the BB counters.

4.3.4 The Zero Degree Calorimeters — ZDC

Located further down stream at $z = \pm 18\,\mathrm{m}$, behind the steering magnets (DX), are the two Zero Degree Calorimeters. Since the DX magnets will sweep away charged particles coming from the collision zone, the ZDC detect neutrons near $0°$. These detectors are mainly used for triggering, but a crude primary vertex determination (v_z) is also possible, which is used for minimum bias analysis of the TMA, SMA, and BB data, with a $\Delta v_z \approx 3\,\mathrm{cm}$.

4.4 The Spectrometers

The spectrometers are basically built up as follows: Two detectors, designed for measuring straight line charged particle trajectories (tracking detector), are placed around a conventional dipole magnet, allowing for a combined momentum and charge measurement (p/q). After this a time–of–flight (TOF) detector is placed to allow for velocity measurements. In the case of the two spectrometers in the Front Spectrometer, where the particles have high momentum, a Čerenkov detector is placed behind the TOF detector, to extent particle identification to high momenta.

Matching up the tracks measured in the two tracking detectors in the mid–plane of the intermediate dipole magnet, allows one to determine the angle of deflection of the charged particle, and hence the momentum[2] p of the particle can be determine. The direction the particle is bent immediately gives the sign of the charge q of the particle. The dipole magnets can be operated at various field strengths and polarities to allow measurement in a wide range of p.

Since the distance from the collision point to the TOF detector is know, the good time resolution of that detector gives a good measure of the velocity β of the particle.

Having measured both the moment p, charge q and the velocity β of a charged particle, it is possible to reconstruct the full four–momentum p_μ of the particle, this gives a complete description of the dynamics and kinematics of the particle.

The three spectrometers are mounted on platforms that allow them to be rotated around the global y axis. Different polar angle (ϑ) ranges have been chosen to maximise the rapidity coverage of BRAHMS.

4.4.1 The Front Forward Spectrometer — FFS

Along with the BFS (see Section 4.4.2) this spectrometer compromises the Front Spectrometer (FS).

The tracking detectors in this spectrometer are the two Time Projection Chambers (TPC), T1 and T2, placed around the dipole magnet D2. Another dipole magnet D1 is placed in front of T1 to sweep away particles with a low momentum or with the opposite charge sign than the one investigated. The time–of–flight detector in this spectrometer is TOF1, consisting of 40 scintillating plastic slats. A threshold Čerenkov detector C1 is placed after TOF1 to better resolve the velocity of the closely spaced $\pi^\pm$ and $K^\pm$, and $K^\pm$ and $p/\bar{p}$ particles.

[2] What is measures is in fact $\frac{p}{q}$, but using the direction of the bending in magnet, $\frac{p}{|q|}$ can be determined, and the PID detectors give $|q|$ so that p is positively identified.

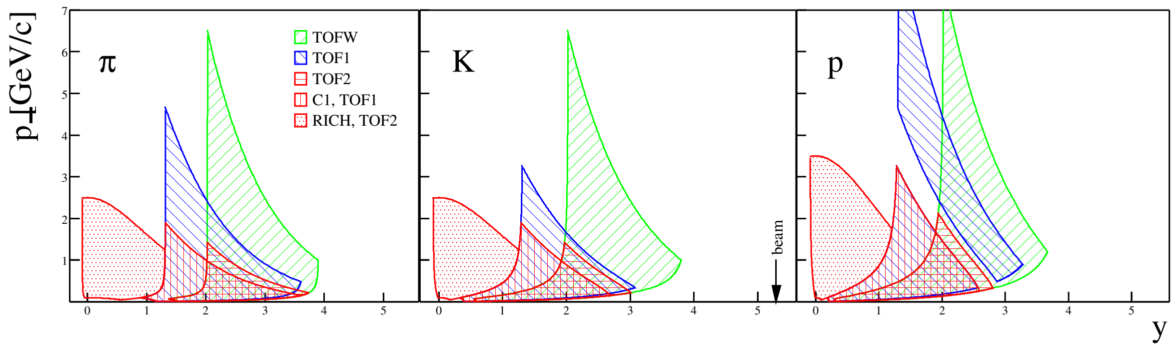

Figure 4.4: Acceptance of BRAHMS

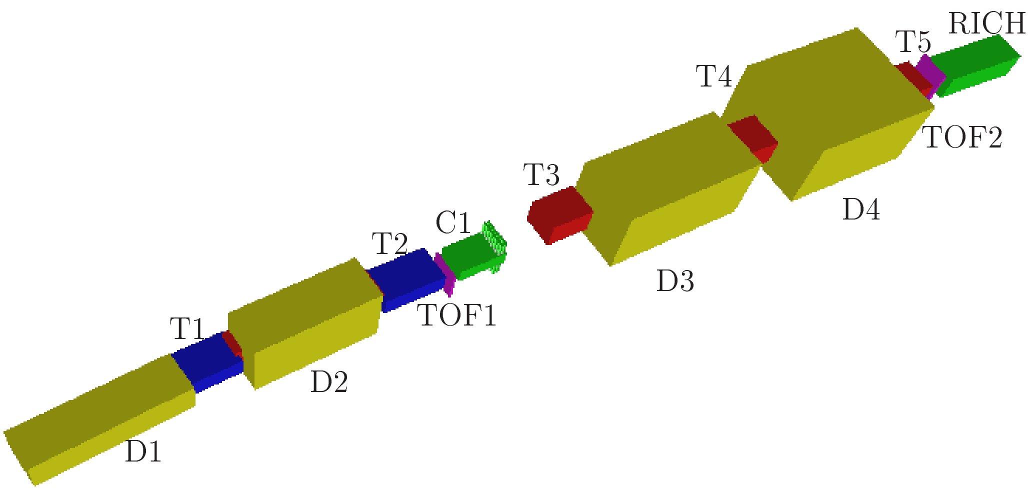

Figure 4.5: Forward Spectrometer — FFS and BFS

The FFS platform can be positioned at angles from 2.3° to 30° giving a large acceptance in rapidity y and transverse momentum $p_\perp$, as can be seen from Figure 4.4.

4.4.2 The Back Forward Spectrometer — BFS

Along with the FFS (see Section 4.4.1) this spectrometer completes the Front Spectrometer (FS).

In the Back Forward Spectrometer, there are three tracking detectors T3, T4, and T5, all of which are conventional Drift Chambers (DC), and two conventional dipole magnets, D3 and D4. This gives two measurements of the charged particles momentum. The TOF detector is TOF2, segmented into 32 scintillating slats. To better resolve the species of the charged particles at high momenta, a Ring Imaging Čerenkov (RICH) counter is located at the end of the spectrometer.

The BFS platform has less ϑ coverage then the FFS; it covers from 2.3° to 15°, but still gives a formidable coverage in rapidity y and transverse momentum $p_\perp$ (see Figure 4.4).

4.4.3 The Mid–Rapidity Spectrometer — MRS

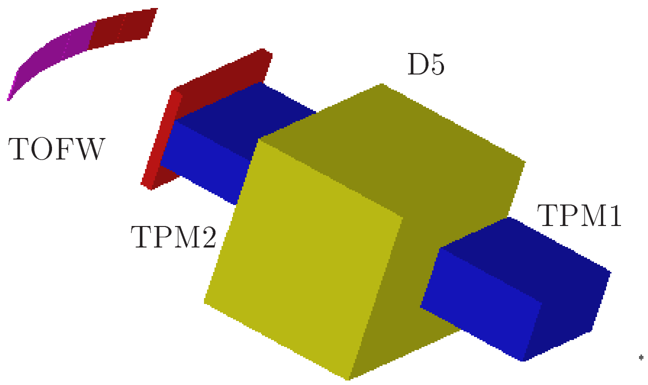

Figure 4.6: The Mid–Rapidity Spectrometer

Consists of two TPCs, TPM1 and TPM2, positioned around the dipole magnet D5, and a time–of–flight detector TOFW. The MRS can cover from $\vartheta \approx 90°$ to $\approx 30°$, thereby just overlapping with the FFS. As there is no filtering magnet in front of TPM1 — as in the FFS — both positively and negative charged particles can be identified in the same setting. The coverage in phase space is shown in Figure 4.4.

4.5 The BRAHMS Databases

During data acquisition and later on in offline analysis, various state information and calibration parameter values need to be stored and kept for future use and reference. To this end BRAHMS exploits well known database technologies in a simple but robust way.

A software package has been implemented for easy access to calibration, geometry, and run information stored in a database. The packaged is designed so that every part is customisable, replaceable and robust. This is realised in an *object oriented* way by exploiting the *polymorphisms*.

The package consists of three layers:

Server Layer: The state information and calibration parameter values are stored on a canonical server, with possible mirror servers and temporary drop–ins, to ensure consistency across the collaboration, which is spread out over Europe and USA. The server serves the actual data to the interface layer. The server can be a *Relation Database*, like MySQL[3], PostGreSQL[4], Oracle[5], SapDB[6] — the only requirement is that there exists an ROOT interface to the server in question; or a ROOT remote file server via HTTP or designated protocol.

Interface Layer: In this layer, the package consists of polymorphic classes for transparent access the server layer, as well as in–memory representations of the data stored in the servers. The polymorphism allows a user to drop–in and replace any part of the server layer with minimal changes in the user setup. This allows for a rigid testing environment with minimal pollution of the production environment, giving increased security of integrity of the data stored on the servers.

Client Layer: User code is served the data from the databases via managers — that is, the data is managed by a class, so that the manager can update the data as needed, and to ensure that all parts of the user code use the same data. This means that the user code need not worry about the actual storage and tags on the data on the servers, but can rely on the managers to serve the appropriate data. This is realised by exploiting ROOTs *Extended Run Time Type Identification* (ERTTI).

Figure 4.7 illustrates this three layer design[7].

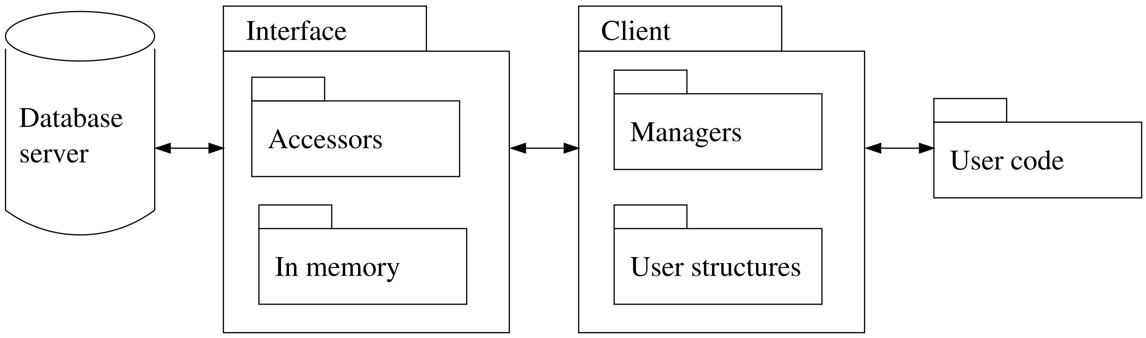

Figure 4.7: Layers of the database software package

The implementation of this design in BRAT [62] has been successfully used for the analysis of the $\sqrt{s_{NN}} = 130\,\mathrm{GeV}$ and $200\,\mathrm{GeV}$ runs.

4.5.1 On the Server Side

The Main Database

On the database server, a special database, henceforth termed the 'main database', is setup. The table layout of that database is shown in Figure 4.8

[3] http://www.mysql.com
[4] http://www.postgresql.org
[5] http://www.oracle.com
[6] http://www.sapdb.com
[7] The diagrams in this section are all UML [61] diagrams.

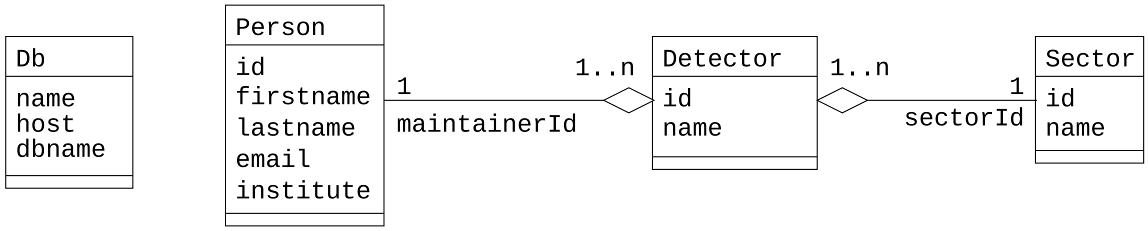

Figure 4.8: Tables in the main database

This database provide identification of other databases, where they are to be found, and what they are named on the (possibly) remote host. Combined with the protocol name of the connection to the main database, this information provides a tagged URI[8] allowing the interface layer to uniquely resolve the reference. Hence, in the user layer, all that needs to be specified is a mnemonic name, like 'calibrations', 'runs', or 'geometry'.

The main database also stores information on collaborators in BRAHMS. This information is used to mark calibrations and the like with an `author` mark, so that in case of problems or trouble it is possible to track down the source. The `Person` information is also used to tag detectors with a `maintainerId`.

Finally, the main database stores information on the `Sector`s and `Detector`s in BRAHMS. The detector information provides a unique numerical identification `id` to be used for look–ups in other databases, such as the calibration or geometry database. Again, the numerical Id's need not be known in the user layer — mnemonic names are indexed for easy look–up. The `id` of a detector or sector, along with the main database protocol, host name, and database name provides the URI for the client layer to uniquely resolve the reference.

The sector information is useful in conjunction with the geometry database. As explained above, the BRAHMS experiment consists of 4 sectors: the global, front forward, back forward, and mid rapidity sectors. Hence, the sector information can be used, so that relative co-ordinates are stored in the geometry database. This has the advantage that the geometry database does not have to be fully updated every time the spectrometers are moved, as the relative coordinates are likely to be unchanged.

Calibration–like Databases

For data that needs to be updated frequently and revisited from time to time, a scheme for calibration–like databases has been developed. The table layout is shown in Figure 4.9.

The `Parameter` table provides information on a generalised parameter. It is identified by a unique numerical identifier, a mnemonic name, and an external reference identifier. The external reference is usually to a detector in the main database, but could equally well refer to something else — it is up to the interface and client layer to correctly resolve those references.

In general, one parameter refers to an array of like parameters. For example, one parameter could hold all the gains of the TMA. The rationale is that only very seldom, will one channel of a multichannel detector be calibrated alone. Hence, the extra logic to handle single channel updates was deemed a too high a price to pay.

The `typeName` field contains information on what type of data[9] the values of the parameter can take, and the `comment` field is there to provide a short human readable description of the parameter. The `policy` field will be explained below.

[8]Uniform Resource Identifier

[9]integers, real numbers, characters, bitmaps, and so on.

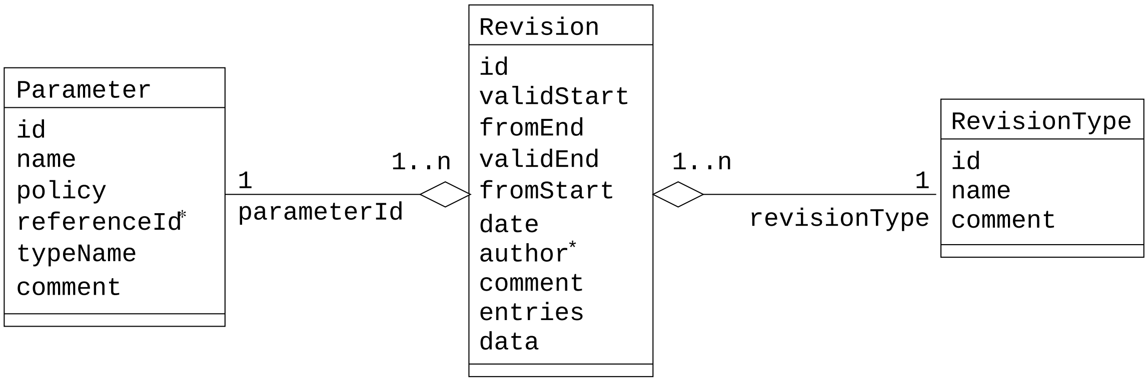

Figure 4.9: Tables in a Calibration–like database. The two fields marked with '*' are external references to the main database.

The actual values of the parameter are not stored in the `Parameter` table, but rather in the separate `Revision` table. This is because the parameter may have different values at different times. For example, the pedestal of a TOF channel may have one valid value at one point, and another 1 week, or even 20 minutes later. The period in time where one set of values are valid for a given parameter is termed a *validty interval* and is stored in the fields `validStart` to `validEnd`. The fields `data` and `entries` contains the actual values and number of values in the revision respectively.

The fields `fromStart` and `fromEnd` contain information on what data was used to make the revision, and `date` says when the data was submitted to the database. The `author` field is an external reference to the `Person` table in the main database, allowing for easier trouble shooting. The `comment` field is used for a short human readable comment to the revision, like for example "This needs to be redone", "Wouldn't use this for production", or "This gives a sigma(t) of less than 10 picoseconds!"

Sometimes it is desirable to revisit or create new values for a given parameter. The system has been designed so that new entries can be added to the `Revision` table as needed, but entries can never be deleted. However, because only one set of values may be valid over a validity period, it may be necessary to split validity periods into 2 or 3 new validity periods. In that way, one is always sure to get one answer to the question "what is the value of element i of parameter p at the time t"?

However, to not lock the system into a too rigid structure, the concept of various types of revisions have been developed. In essence, a user may tag a revision with an entry in the `RevisionType` table, and thereby bypass the strict 'one value per validity interval' rule described above. This not encouraged either by the developers or by the system, but the possibility exists should the need ever arise.

It could very well happen that there exists no revision in the database for a given parameter at a given time. This is when the `policy` field of the `Parameter` table comes into play. This field essentially says whether to look back in time to find the newest valid revision, look forward to find oldest, valid revision, or send the client level an error condition. In this way, one need not be deadlocked into situations that require a bootstrap — one can use an older/newer revision until it is possible to bootstrap[10] i.e., create a revision for the period at hand.

It should be noted that the above scheme is flexible and general enough for all kinds of data to be stored in it. For example, acceptance and correction maps could be stored in a

[10] The term 'bootstrap' comes from the ludicrous idea of trying to lift oneself by ones boot straps. Baron von Münchausen told a story of how he once rescued himself *and* his horse from a deadly swamp by lifting himself by his pony tail — of course he is known as the world greatest liar.

database like the above, as well as articles, figures, and the like. However, the scheme is most useful for data that changes over time, and sometimes need to be updated.

4.5.2 Interface, Client and User Layer

Interfaces

In the interface layer, several classes for accessing data on the servers have been defined. These are shown in Figure 4.10. All access goes through abstract interfaces like *BrMainDb*

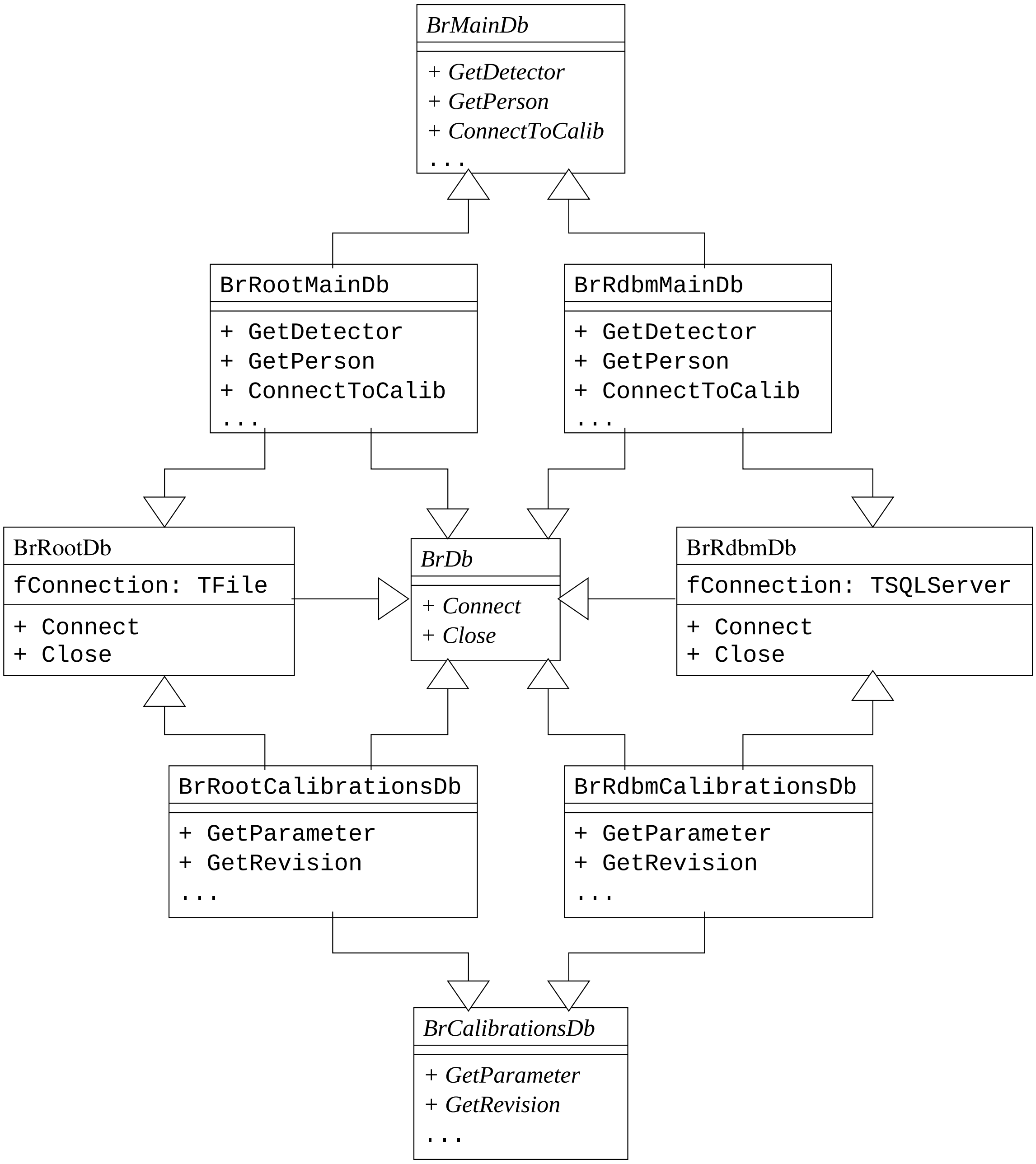

Figure 4.10: Database interfaces. Only the main and calibration interfaces are shown. Names in *italic* denote abstract definitions, and arrows indicate inheritance.

and *BrCalibrationsDb*; the actual interface is selected by the protocol name specified in the connections. In this way, the user can easily change the back–end via a simple change of argument. The connections to databases other than the main database is facilitated by for example *ConnectToCalib* in the *BrMainDb* interface. These methods look up the host and database name in the `db` table of the main database, based on a mnemonic name passed to the interface.

In the interface layer, there also exists in–memory representations of the database tables as explained in the previous section and shown on Figure 4.8 and Figure 4.9. These classes have the same names as the tables with a `BrDb` prefix.

Managers

To insure that all classes use the same data, a set of managers for the database data have been developed. An example, using the calibrations database is shown in Figure 4.11.

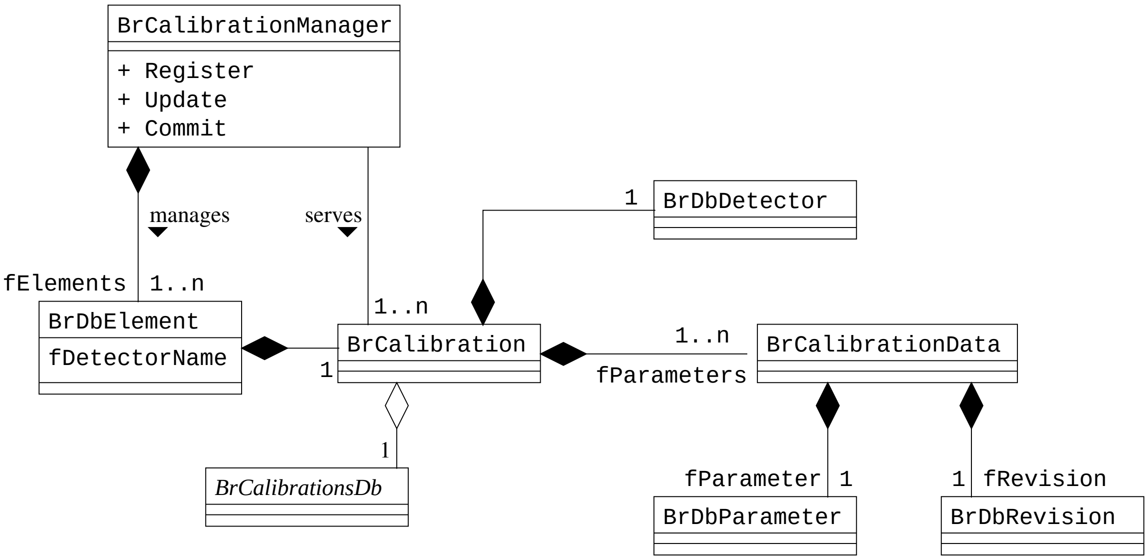

Figure 4.11: Database managers. Only the calibration manager is shown.

The method `Register` is used to register detectors for use with the manager, so that the manager will fetch or store the data needed for that detector when the `Update` or `Commit` messages respectively, are sent to the manager. The class `BrDbElement` is used to associate a detector with a `BrCalibration`, and `BrCalibrationData` associates a `BrDbParameter` with the current valid `BrDbRevision`.

User Code

The user code defines specialised `BrCalibration` classes that a given detector will use. Figure 4.12 shows an example for the SMA.

The `BrCalibration` sub–class `BrSiCalibration` contains a set of `BrCalibrationData` objects; one for each parameter that the detector uses. In Figure 4.12 the `fPedestal` parameter is shown. User code like `BrSiRdoModule`[11] registers and uses the sub–class of `BrCalibration` to get or set the parameters that it needs. It obtains a handle on the data by sending a request message to the `BrCalibrationManager`. It does not own the data; instead the manager owns the data, so that all pieces of user code gets the same handle to the data.

[11]The code that does the first level reconstruction for the SMA.

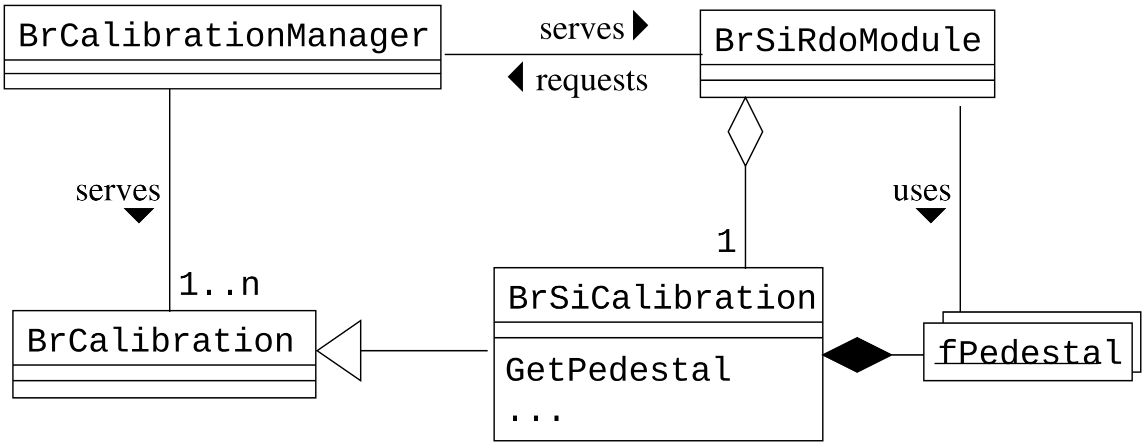

Figure 4.12: User code example. The class `BrSiRdoModule` uses the pedestal values from the `BrSiCalibration` object, served via the *BrCalibrationManager*.

4.5.3 Comments

The design is completely implemented in an Object–Oriented way, making it robust, easy to maintain, and expandable. The advantage of the rather complex interface system as shown in Figure 4.10, is that the system is easily extended, and if a given back end becomes obsolete, it can easily be replaced without the user ever noticing the change. Further, the design is robust enough to handle a large range of use cases.

Chapter 5

Analysis

In this chapter, the main body of the this work is presented. The first section (Section 5.1) explains the event selection based on the hardware triggers setup during the $\sqrt{s_{NN}} = 200\,\text{GeV}$ Au+Au run. Section 5.2 describes how the z–coordinate the primary interaction point is determined by using the beam–beam counters. From there, the Section 5.3 describes the procedure to obtain the energy deposited and multiplicity in the TMA and SMA, as well as the collision centrality. In Section 5.4 the measured fluctuations in charged particle multiplicity and energy deposited in the SMA is presented. Chapter 7 uses the results from this chapter to attempt to extract the interesting fluctuation in the number of produced particles per source.

5.1 Triggers and Minimum Bias

In BRAHMS, four physics triggers were set up for the $\sqrt{s_{NN}} = 200\,\text{GeV}$ Au+Au run. These are tabulated in Table 5.1.

#	*Description*
1	Coincidence of the two BB arrays, with at least 3 hits in both arrays.
3	Energy threshold in the TMA.
4	Coincidence of the two ZDC arrays above 1 neutron threshold.
5	Coincidence of the two BB arrays, with a narrow time gate, selecting primary vertex z–coordinates $\in [-20\,\text{cm}, 20\,\text{cm}]$
6	Coincidence of triggers 3 and 5.

Table 5.1: Physics triggers for the $\sqrt{s_{NN}} = 200\,\text{GeV}$ run.

Trigger 6 is setup to select as central events as possible. It selects from 0 % to approximately 15 % with full efficiency, and then drops abruptly to up to 35 % (see also Figure 5.1). This is the trigger used for most of the analysis based on the spectrometer arms FFS, BFS and MRS.

Trigger 4 selects most collisions. Spectator neutrons are detected in the calorimeters sitting down stream from the interaction region, signalling some interaction took place, even if it was only Coulomb dissociation. Since the trigger 4 is abundant, it was scaled down by a factor 20 to 100 during the $\sqrt{s_{NN}} = 200\,\text{GeV}$ run, meaning only the 20^{th} to 100^{th} trigger 4 event was written to storage.

Trigger 4 with the additional requirement of at least one hit above threshold in the TMA (see also Section 5.3, (5.2)), is what defines the *minimum bias* event sample in BRAHMS. This requirement effectively covers 97 % of the full nuclear cross section. The minimum bias event sample is used for the SMA and TMA energy, centrality, and multiplicity calibrations.

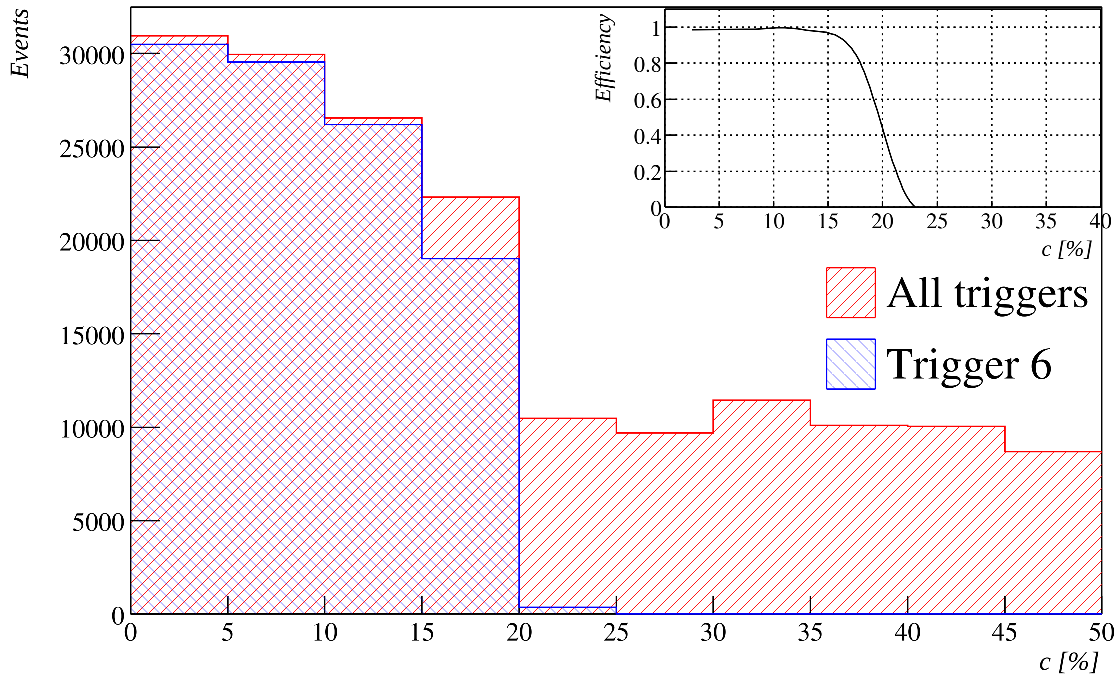

Figure 5.1: Number of events of run 5972 with all physics triggers, and requiring trigger 6 (inclusively) as a function of centrality. Insert shows the efficiency.

For these calibrations, large minimum bias event samples are needed. Unfortunately only very few, and only at the start of the run, minimum bias samples was collected during the $\sqrt{s_{NN}} = 200\,\mathrm{GeV}$ Au+Au. This makes calibrating for later runs, when RHIC was working best, much harder to do.

The distribution of triggers used in this analysis is shown on Figure 5.3(a).

5.2 Primary Vertex Determination using the BB

Due to the close proximity of the SMA and TMA to the collision point, variations in the collisions points z–coordinate (called v_z in the following) gives rise to variations in the number of charged particles that hit the individual elements in the arrays. These variations come from the fact that for a given element the mean η is dependent on the vertex' v_z, and hence will see a v_z dependent part of the $\frac{d^2N}{d\eta d\varphi}$. Also, the angle at which charged particles traverse the detector elements, and hence the length of matter the particles traverse, changes with v_z, giving rise to variations in the deposited energy by the charged particles (see also Figure 5.5(a)).

It is therefore of the utmost importance that the primary vertex location along the beam line is well known when studying the measurements of the SMA and TMA.

The method employed in this work uses the BB counters to measure v_z. The idea is sketched in Figure 5.2. The time signals of the BB counters are given by

$$t_L = \tau_L - \tau_t \qquad\qquad t_R = \tau_R - \tau_t \quad ,$$

where τ_L and τ_R are the actual time of flight of the particles, and τ_t is the unknown trigger delay, calibrated so that it is the same for all the BB counters. Assuming that the first or most of the particles that hit the BB counters have $\beta = 1$, which is not such a bad assumption for at least π's, the time signals can expressed as

$$t_L = \beta(l + v_z) - \tau_t \qquad\qquad t_R = \beta(l - v_z) - \tau_t \quad ,$$

which holds approximately even for outer counters in the arrays. Thus v_z, the primary vertex' z–coordinate can be calculated as[1]

$$v_z = c\frac{t_L - t_R}{2} \tag{5.1}$$

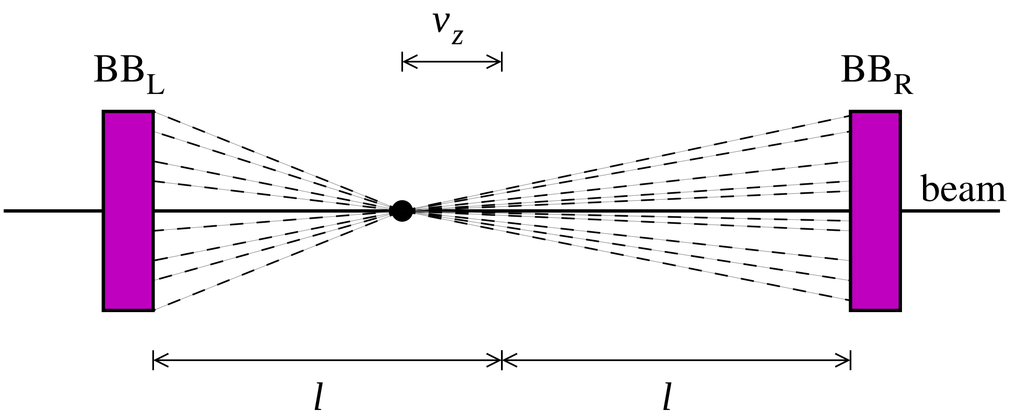

Figure 5.2: v_z from the BB

There are three different t_L and t_R that can be used in the (5.1), each with different merits (below $t.$ denotes either t_L or t_R):

First hit: The time of first hit i.e., the one with the smallest time signal, in all of the counters of each array is used for $t.$. This method relies on good calibrations and not too noisy detector signals

Small radiators: The $t.$ used is the truncated average[2] of all of the time signals from the small Čerenkov radiators. This method is good for events where the particle density at the BB counters is high i.e., central events, as the coverage of the small radiators is small, and hence timing resolution is not worsened by the high density.

Large radiators: For events with a lower particle density at the BB i.e., peripheral events, the number of small radiators that is hit can be very small, and the average of the time signals may be dominated by statistical uncertainties. On the other hand, the large radiators have a larger coverage and thus larger probability of being hit. Therefore, if the above method using the small types fails, the average of the time signals from the large radiators is used for $t.$.

During the calibration of the BB, the v_z found by the above methods is checked against a v_z calculated by pointing tracks back from TPM1 (see Figure 4.2) to the beam line, and an offset is introduced to line up the BB v_z and the TPM1 vertex found from the tracks. This resolves the unknown absolute delays and offsets between the two BB arrays. This gives a final v_z resolution of $< \pm 1\,\mathrm{cm}$.

Because the SMA spans from $z \approx -20\,\mathrm{cm}$ to $z \approx 20\,\mathrm{cm}$, only events with v_z in that range have been selected for the current analysis. Figure 5.3(b) shows the vertex distribution used for this analysis. In more than 90 % of these events, the small radiator time signals have been used.

[1] Here, an explicit factor of c, the speed of light has been included for clarity.
[2] *Truncated* means that all outliers (signals far away from the direct average) are ignored in the final sum.

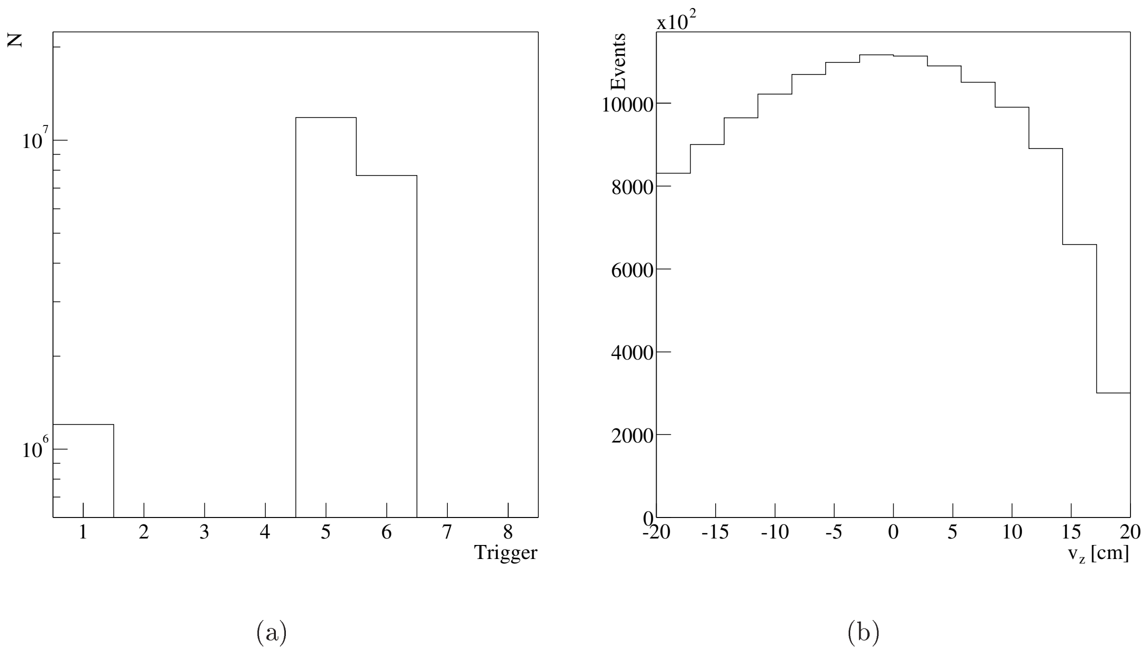

Figure 5.3: (a) Triggers used in this analysis. (b)v_z distribution used in this analysis. Most of these ($> 90\,\%$) come from the small radiators. The asymmetry is simply a consequence of the collider steering in the runs analysed.

5.3 Energy, Multiplicity and Centrality using the TMA and SMA

5.3.1 Calibrations

As mentioned in Section 4.3.1 the occupancy of the individual tiles of the TMA is almost 100 %, making the extraction of charged particle multiplicities from the raw ADC counts a highly non–trivial issue.

As with most detectors, the SMA and TMA have noise which the ADC picks up. This noise is identified in the raw ADC spectrum (see Figure 5.4(a)) with no physics triggers, as a rather sharp Gaussian distribution — the pedestal. Dedicated runs are made for measuring the pedestals of all detectors that have this feature — which most of them have. The pedestal mean $\overline{p_i}$ and spread $s^2_{p_i}$ is found offline, and fed into the database for later retrieval during first–level analysis.

In the analysis of subsequent data, an ADC value A_i is accepted as a hit for the i^{th} detector, if

$$A_i > t_i \qquad \text{where} \quad t_i = \overline{p_i} + t_f s^2_{p_i} \quad . \tag{5.2}$$

Here, t_f is the *threshold factor*, typically set to 4 or 5.

To calibrate the ADC *gain* of the SMA and TMA, i.e. find the conversion factor from ADC counts to energy, the detectors are set up in the laboratory to measure μ's from cosmic rays. These particles are very energetic and therefore *minimum ionising*, making it possible to calibrate a conversion from ADC counts to energy deposited. Minimum ionising means, that the particles deposits the least possible amount of energy, through ionisation (see also Section 6.1.3 for a longer discussion). These numbers are called the *gain factors* g_i (or simply gain) and are fed into the database for later retrieval. The energy deposited in a given element can therefore be calculated as

$$E_i \equiv \begin{cases} g_i\left(A_i - \overline{p_i}\right) & A_i > t_i \\ 0 & A_i \leq t_i \end{cases} \tag{5.3}$$

Example spectra of pedestal subtracted ADC count and energy deposited are shown in Figure 5.4(b) and 5.4(c).

Using minimum–bias runs the full spectra of deposited energy for valid hits of all elements is extracted. These spectra are matched up with the corresponding spectra from a GEANT3.21–based [63] detector simulation of BRAHMS, using the HIJING model as input. A mapping $c_i : E_i \mapsto M_i$ from energy deposited to number of primary particles is made, and stored in the database for later retrieval. The charged particle multiplicity in each element can calculated as

$$M_i = E_i c_i(\eta_i(v_z)) \sin\vartheta_i(v_z) \quad , \tag{5.4}$$

where η_i is the average η of the i^{th} detector, which obviously depends on v_z. The η dependency enters, as the mix of soft (not minimum ionising) and hard (minimum ionising) particles varies over η. As mentioned in the previous section, the amount of material that a particle traverses depends strongly on the primary vertex' z–coordinate. To correct for this, a factor of $\sin\vartheta_i$, where ϑ_i is the shown in Figure 5.5(a), is multiplied to the gain corrected value.

An in–depth description of the calibration process of the TMA and SMA can be found in [60].

5.3.2 Charged Particle Multiplicity Distribution — $\frac{dM_{\text{ch}}}{d\eta}$

The final multiplicity distribution $\frac{dM_{\text{ch}}}{d\eta}$ is obtained by adding up the individual contributions from the detector elements, corrected for the geometrical acceptance of the given element, and normalised to the number of events:

$$\left.\frac{dM_{\text{ch}}}{d\eta}\right|_{\eta=\eta_i} = \frac{1}{N}\sum_j^N \frac{1}{N_{j,i}}\sum_k^{N_{j,i}} M_{i,k}\frac{2\pi}{\Delta\varphi_k\Delta\eta_k} \quad , \tag{5.5}$$

where N is the number of events, $N_{j,i}$ is the number of hits in j^{th} event in the i^{th} η bin, and $\Delta\varphi_k$ and $\Delta\eta_k$ are the polar angle and η acceptance of the k^{th} detector element respectively (see also Figure 5.4(d) for an example spectrum). The acceptance factors are given[3] by (see also Figure 5.5(b)):

$$\Delta\varphi_k = \tan^{-1}\frac{w_k}{2r_k} \qquad\qquad \Delta\eta_k = \left|\log\frac{\tan\frac{\vartheta_{k,max}}{2}}{\tan\frac{\vartheta_{k,min}}{2}}\right| \tag{5.6}$$

where

$$\vartheta_{k,min} = \begin{cases} \tan^{-1}\frac{r_k}{z_k - l_k - v_z} & z_k - l_k \leq v_z \\ \tan^{-1}\frac{r_k + d_k}{z_k - l_k - v_z} & z_k - l_k > v_z \end{cases} \qquad \vartheta_{k,max} = \begin{cases} \tan^{-1}\frac{r_k + d_k}{z_k + l_k - v_z} & z_k + l_k \leq v_z \\ \tan^{-1}\frac{r_k}{z_k + l_k - v_z} & z_k + l_k > v_z \end{cases} \quad ,$$

and w_k, and r_k are defined in Figure 5.5.

This analysis of the SMA data, along with a similar analysis of the BB data, for Au+Au at $\sqrt{s_{NN}} = 200\,\text{GeV}$ has been published in *Phys. Rev. Lett.* [16]. Figure 5.6 shows the $\frac{dMch}{d\eta}$ for various centrality cuts, from that publication.

[3]Please also refer to Figure B.6 and Table B.2 for a list of $\bar{\eta}$ and $\Delta\eta$ for each of the SMA rings

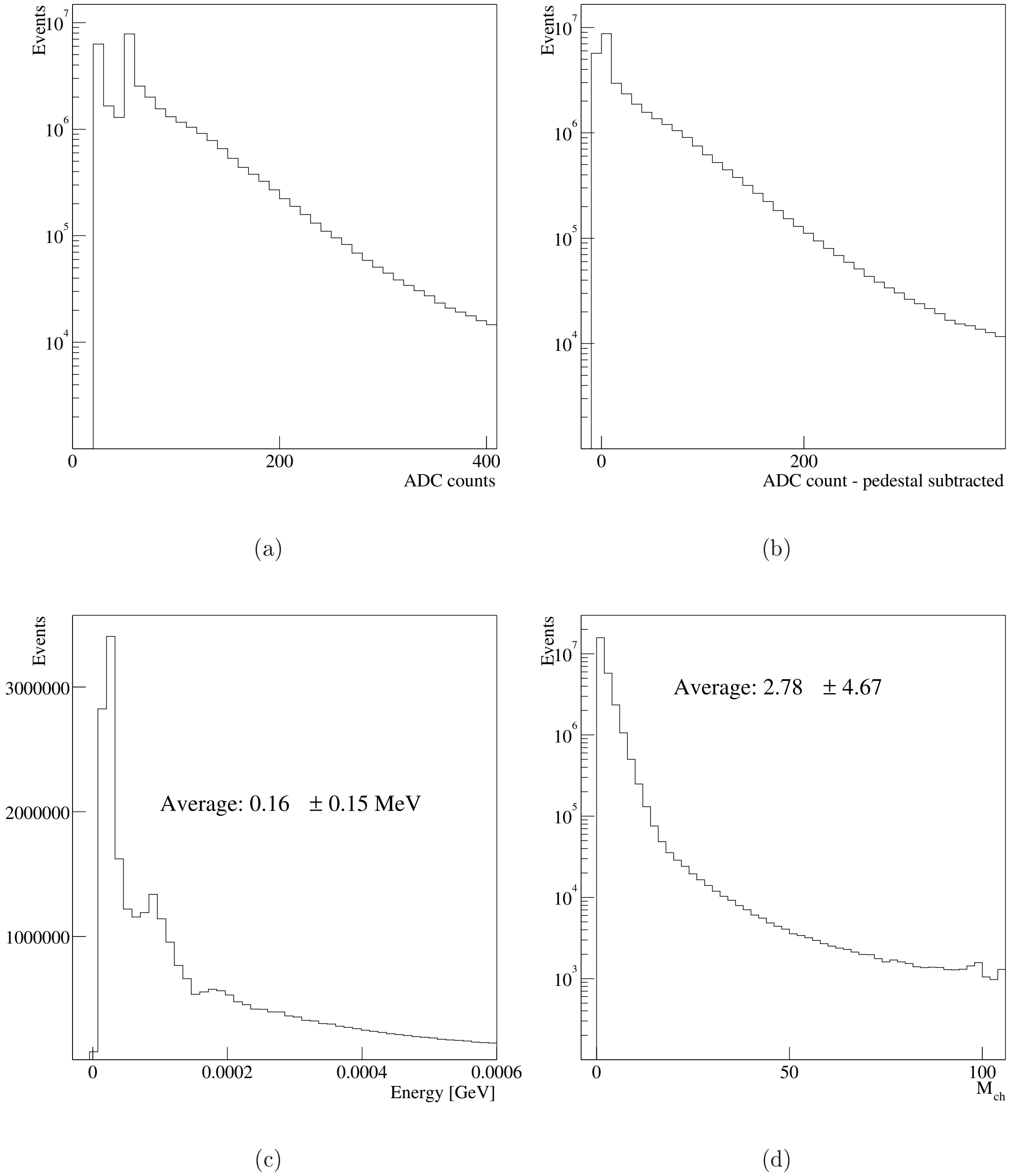

Figure 5.4: Example spectra (strip number 50) in 0 %–35 % central collisions. (a) Raw ADC counts. (b) ADC counts fulfilling valid hit criteria and after pedestal subtraction. (c) Energy deposited. (d) Multiplicity.

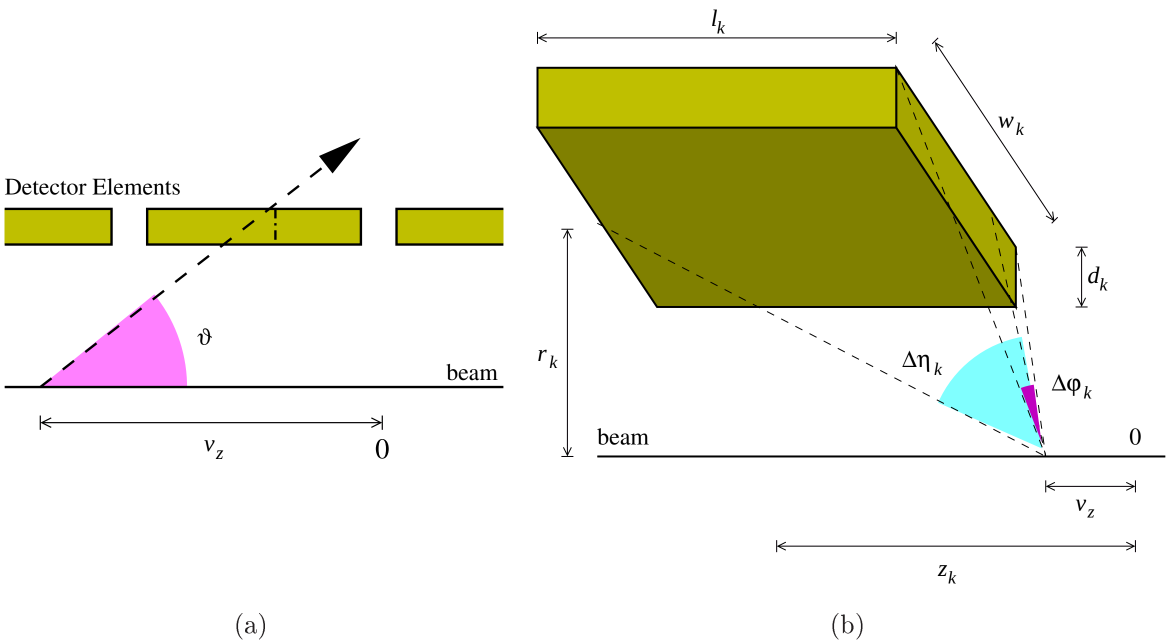

Figure 5.5: (a) Particles traversing a SMA/TMA element at $v_z \neq 0$. (b) Schematic acceptance of a TMA/SMA element. Note that r_k is 13.6 cm for all TMA elements, and 5.31 cm for all SMA elements.

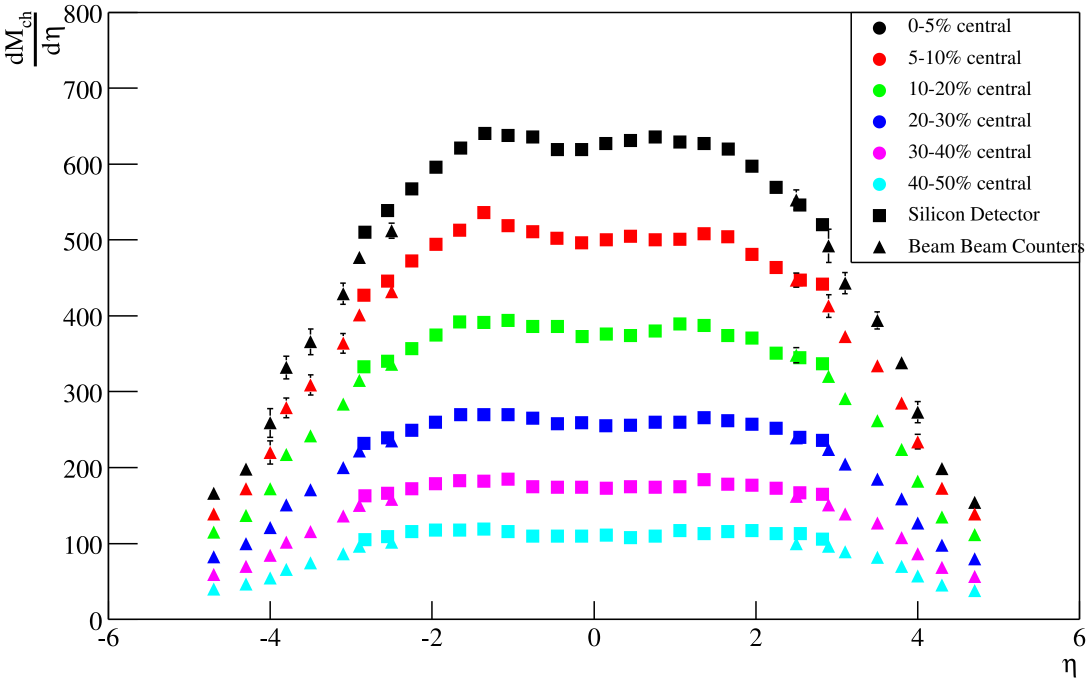

Figure 5.6: $\frac{dM_{\mathrm{ch}}}{d\eta}$ for Au+Au at $\sqrt{s_{NN}} = 200\,\mathrm{GeV}$ as measured by BRAHMS [16]. Error bars are only shown were they are larger than the marker symbol.

5.3.3 Centrality

As mentioned previously, the impact parameter b is of great importance when analysing the data from A+A collisions, but unfortunately that number is not accessible to the experiment. Instead one characterises events by the *centrality* of the events. One can think of centrality as a measure of how brutal a given collision was.

The centrality c, of a given event is defined as

$$c(x_i) = \frac{\int_{x_i}^{\infty} dx\, \frac{dN}{dx}}{\int_{0}^{\infty} dx\, \frac{dN}{dx}} \cdot 100\,\% \tag{5.7}$$

where x is either the full M_{ch} in the SMA and TMA, or the deposited energy in either detector, $\frac{dN}{dx}$ is the corresponding minimum bias distribution, and x_i is the relevant number for the given event. That is, the centrality is the maximum fraction of minimum bias events that has the same or higher x. c is often something like $5\,\%, 10\,\%, \ldots, 50\,\%$.

In other words, when one speaks of the event centrality being c, what one means is that the event has an x value that falls within the range of ratio c of events that has the highest x. For example, if an event has a total energy deposited of 3 GeV, then, referring to Figure 5.7(b), the event falls within the $0\,\%$–$3\,\%$ class of events. If an event has a total energy deposited of say 1.5 GeV, it has a centrality of $10\,\%$–$15\,\%$.

In the actual analysis, the integrals in (5.7) can not evaluated event–by-event. A series of dedicated runs where a large minimum bias sample is collected, is used to evaluate the denominator in (5.7) and cuts in x corresponding to a given percentage are defined. Figure 5.7 show these cuts.

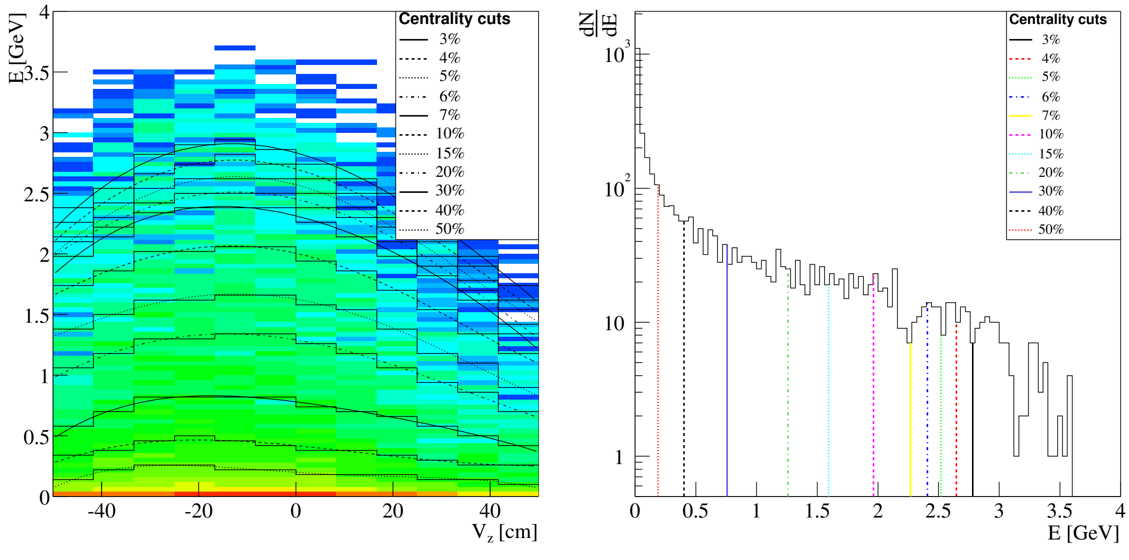

(a) (b)

Figure 5.7: Centrality cuts based on the energy deposited in the TMA. (a) Shows the distribution of the cut values as a function of the primary vertex's z coordinate. (b) Section of (a) at $8.2\,\mathrm{cm} \leq v_z \leq 0\,\mathrm{cm}$, with cut values superimposed.

The assumption is then, that there is a monotonic mapping from c to b however undetermined from experimental data. Using models, one can get a feeling whether that assumption is reasonable or not. As seen in Figure 5.8, this is not at all a bad assumption, with the $c \mapsto b$ in the range of $c \in [0, 50]$ being more or less linear. Of course, this is not something on which one can build a conclusion about the impact parameter based on the centrality, as it is entirely model dependent, but it serves to show that the principle of centrality is indeed sound.

The method employed in this work is based on the distribution of deposited energy in the TMA. This gives a clean unbiased event selection for the analysis of the SMA data. The distribution of centralities used in this analysis is shown on Figure 5.3.3.

5.4 Fluctuations Charged Particle Multiplicity and Energy Deposited in the SMA

Now we finally turn to fluctuations in multiplicity and energy deposited measured using the SMA. The measures used here are ω_{Mch} and ω_E — the fluctuations in charged particle multiplicity and the energy deposited in the SMA silicon strips (see also Section 3.2.4).

Event Sample

A fine segmentation of 25 even sized bins in the η range $[-2.5, 2.5]$ was used, and 4 bins in φ corresponding to rows of the SMA that were more or less fully instrumented. The rows of the SMA with only 7 or 14 active strips was ignored as the numbers of measurements was severely limited by statistics. In centrality c, 13 bins with variable bin sizes were used, to better resolve the contribution to ω_E from variations in the impact parameter b. An overview is given in Table 5.2

Variable	*# of bins*	*Ranges*
η	25	evenly spaced in $[-2.5, 2.5]$ ($\Delta\eta = 0.2$)
φ	4	[30°,90°),[90°,150°], [210°,270°),[270°,330°]
c	13	[0 %,2 %], (2 %,3 %], (3 %,4 %], (4 %,5 %], (5 %,6 %], (6 %,7 %], (7 %,8 %], (8 %,9 %], (9 %,10 %], (10 %,15 %], (15 %,20 %], (20 %,25 %], (25 %,30 %]

Table 5.2: Bin ranges and sizes

The fluctuations is calculated in separate η, φ matrices for each defined event class. The classification of events is done based on the centrality as determined from the TMA. Hence, a set of data tensors are set up, indexed by c, η, and φ — one for $\overline{Mch}$, $s^2_{M_{\mathrm{ch}}}$, $\overline{E}$, s^2_E and one for the number of events N with data in those bins. For a given event, sub–matrices of the tensors are chosen, based on the centrality, and the average and squared spread of the charge particle multiplicity and energy deposited are updated[4] in those matrices. Only η, φ bins that contain non–zero energy deposited are updated (see also Figure 5.10). The SMA ADCs saturate at 2000, from which point on, it is not possible to resolve M_{ch} and E, why these hits are ignored.

M_{ch} and E for a given η, φ, c bin is calculated as the acceptance corrected sum of the

[4]See Appendix C.2

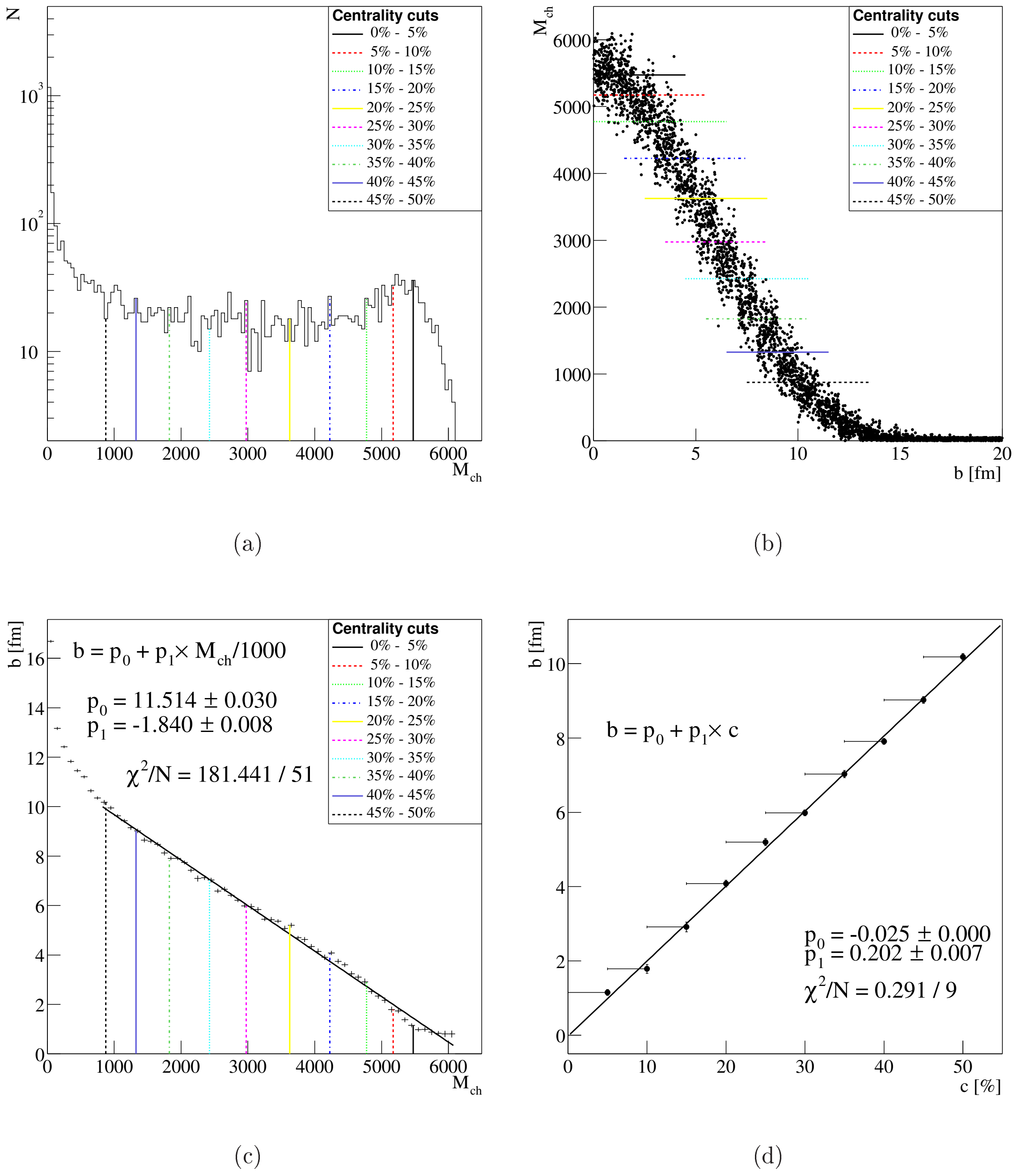

Figure 5.8: Estimation of c to b mapping using the HIJING model [11,12]. (a) shows the centrality cuts defined, (b) is similar to Figure 2.3(b) but with the centrality cuts superimposed, (c) is a profile of (b) fitted to a straight line in the interval $M_{\mathrm{ch}} \in [800, 6100]$, and (d) is obtained from (c) by correlating the cut values with the corresponding b. Note, that vertical bars indicate the bin width, not the error in c.

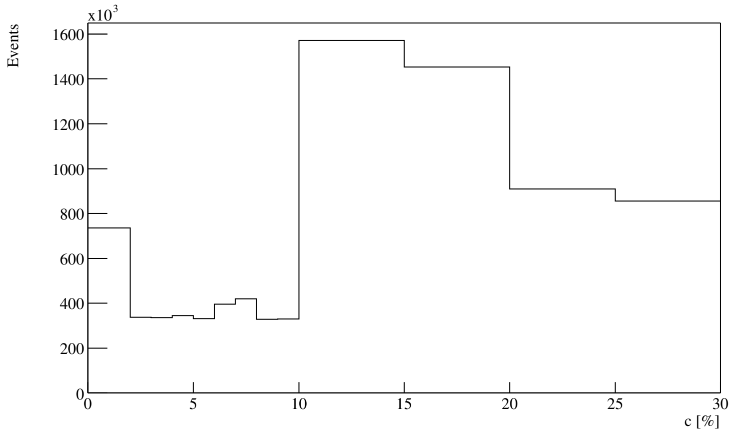

Figure 5.9: Centrality distribution used in this analysis. Note that the bin sizes varies (see also Table 5.2), so that the most central bins look smaller. However, the sum of those in 5 % bins are of course higher than the higher bins. The event sample consists not only of trigger 6 events, but all the physics triggers.

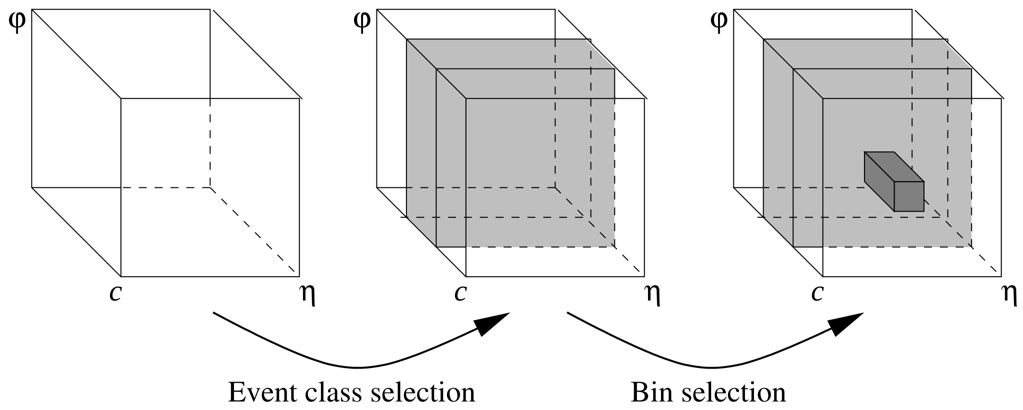

Figure 5.10: Selection of sub-matrix (centrality) and element (η, φ) in data tensors.

$N_{\eta,\varphi,c}$ contributions from detectors that are in that η, φ, c range.

$$M_{\mathrm{ch}\,\eta,\varphi,c} \equiv \sum_{i}^{N_{\eta,\varphi,c}} M_{\mathrm{ch}\,i} \frac{2\pi}{\Delta\varphi_i \Delta\eta_i} \sin\vartheta_i \tag{5.8}$$

$$E_{\eta,\varphi,c} \equiv \sum_{i}^{N_{\eta,\varphi,c}} E_i \frac{2\pi}{\Delta\varphi_i \Delta\eta_i} \sin\vartheta_i \tag{5.9}$$

Here, the symbols have the same meaning as in (5.3) to (5.6), except that $N_{\eta,\varphi,c}$ is the number of detectors that fell into the η, φ, c bin in a given event, and $\Delta\varphi_i$ and $\Delta\eta_i$ are bin sizes in φ and η of the η, φ, c bin.

Figure 5.11 shows the distribution of counts in each of the η, c bins. More than 10 000 000 events within the η and centrality criteria was used. This gives a number of counts > 1 000 000 in each bin, satisfying the need for a large statistical sample to validate the assumptions of the central limit theorem[5].

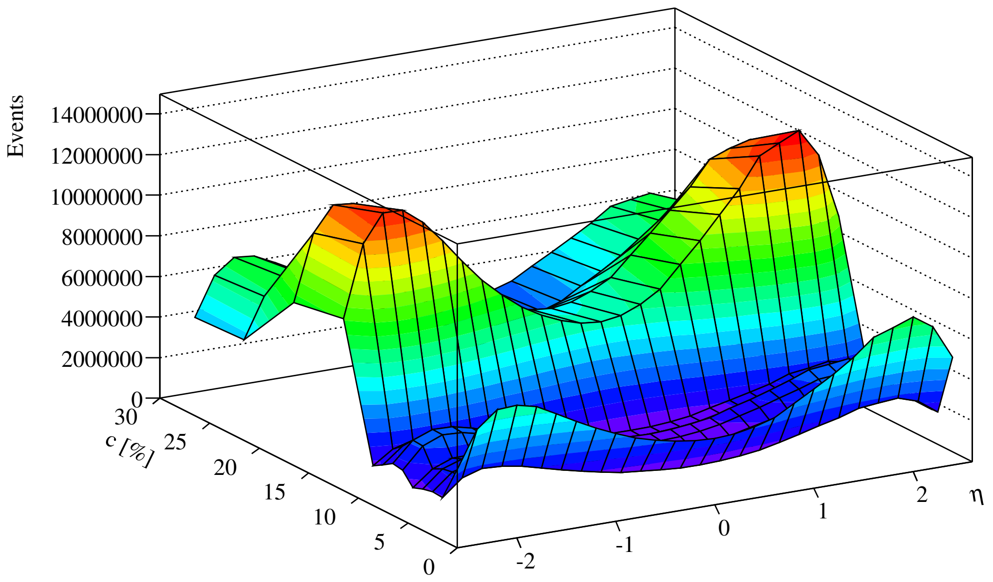

Figure 5.11: Distribution of measured counts in η and c, showing the large sample sizes in each η, c bin.

Errors

The statistical error on ω_x is given by (see Appendix C.1 for derivation):

$$s^2_{\omega_x} = \frac{\omega_x^2}{N}\left(\frac{\omega_{=}x}{\bar{x}} + 4\right) \quad . \tag{5.10}$$

[5]Please also refer to Appendix B for more details on the analysis useful for the BRAHMS collaborator.

The systematic error, $s^2_{\omega_x}$,is obtained from the systematic error on x by observing that for a constant a

$$\omega_{ax} = \frac{s^2_{ax}}{\overline{ax}} = \frac{\frac{1}{N-1}\sum_i (ax_i - \overline{ax})^2}{\frac{1}{N}\sum_i ax_i} = \frac{a^2\frac{1}{N-1}\sum_i (x_i - \bar{x})^2}{a\frac{1}{N}\sum_i x_i} = a\omega_x \quad .$$

Thus, the systematic errors on $\omega_{M_{\mathrm{ch}}}$ and ω_E are the same as the systematic errors on M_{ch} and E.

Polar angle φ and Centrality c Dependence

As can be seen on Figure 5.12(a), ω_E does not vary much over φ and hence the rest of the analysis is carried out summing over the full range in φ.

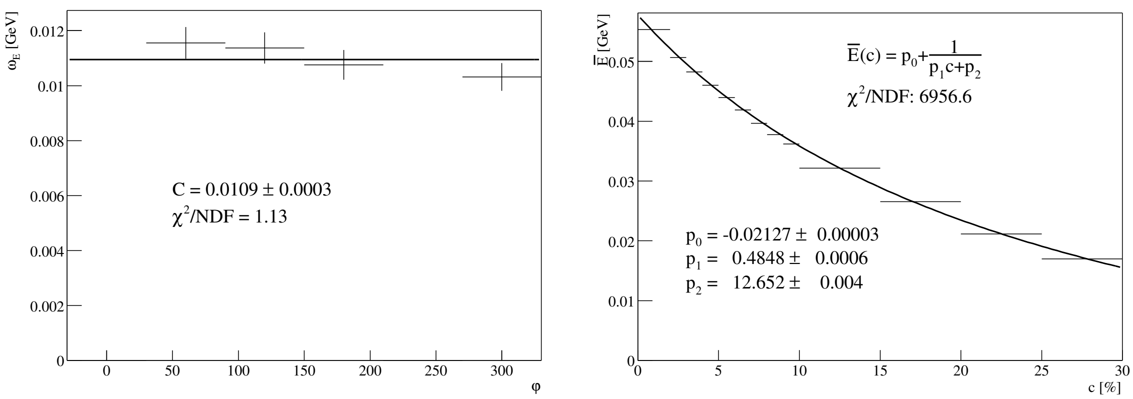

(a) (b)

Figure 5.12: (a) ω_E as a function of φ. (b) $\overline{E}$ as a function of c.

Figure 5.13 shows the measured fluctuations charged particle multiplicity and in deposited energy in the SMA.

A more striking feature of the analysis, shown in Figure 5.13(b), is that ω_E varies very little with c. This is an indication that very little changes in the region of $c \in [0\,\%, 30\,\%]$, which approximately covers from full to half overlap of the colliding nuclei (see Figure 5.8(d)).

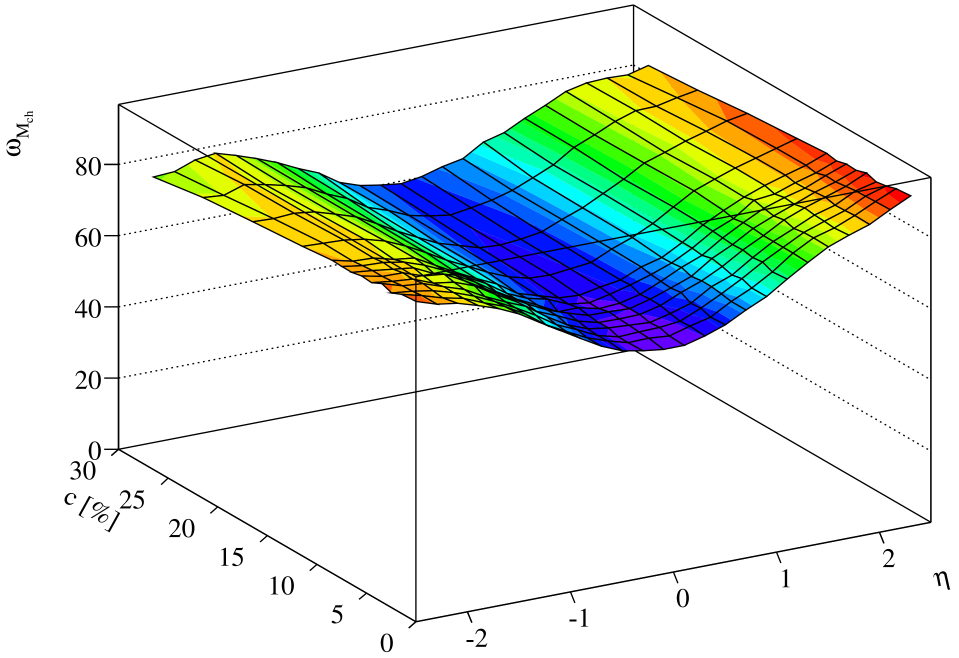

(a)

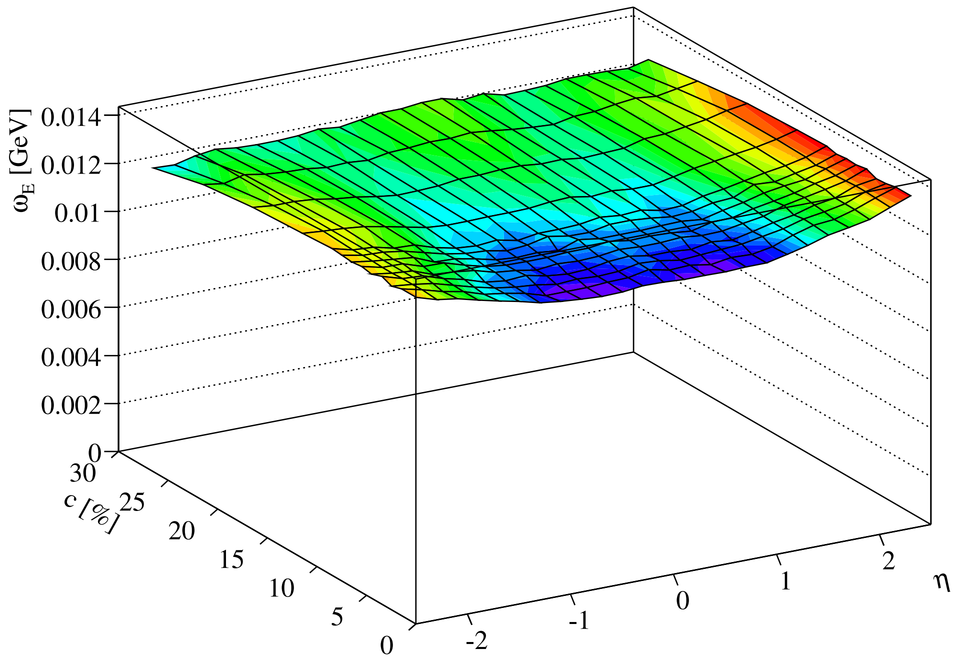

(b)

Figure 5.13: $\omega_{M_{\rm ch}}$ and ω_E as a function of η and c.

Chapter 6

Simulated Data

To better understand the individual terms and factors that go into equation (3.17),

$$\omega_E = \omega_e + \frac{\overline{E}}{\overline{M_{\mathrm{ch}}}}\left(\omega_m + \frac{\overline{E}}{\bar{e}}\frac{\omega_n}{\bar{n}}\right) \quad , \tag{3.17}$$

a model was used to generate some data. Various contributions to the fluctuations as measured in the SMA is identified and discussed. At the end of the chapter, some points on the inherent limitations of the SMA detector are discussed, pointing to the difficulties associated with using this detector for fluctuation analysis.

6.1 Using the Vanilla Model and BRAG Simulation

The vanilla[1] model data can be analysed to give the fluctuation and average in charged particle multiplicity $\omega_{M_{\mathrm{ch}}}, \overline{M_{\mathrm{ch}}}$ (just after thermal freeze–out), and the fluctuation and average of number of sources $\omega_n, \bar{n}$. Using that information, one can resolve the fluctuation in number of produced particles per source ω_m, using (3.12)

$$\omega_{M_{\mathrm{ch}}} = \omega_m + \overline{m}\omega_n \quad . \tag{3.12}$$

Feeding the model data into BRAG, the GEANT3.21 based simulation of BRAHMS detectors, it is possible to obtain the fluctuation and average energy deposited per particle $\omega_e, \bar{e}$, as well as the fluctuation and average in charged particle multiplicity and energy deposited $\omega_{M_{\mathrm{ch}}}, \overline{M_{\mathrm{ch}}}, \overline{E}, \omega_E$, in each η, φ cell in the acceptance of the BRAHMS $\omega_E, \overline{E}$. Note however, that the charged particle multiplicity derived from the BRAG simulation includes particles produced after the chemical freeze–out[2], of the Au+Au collision — that is, particles produced via decay or interactions in the beryllium beam pipe or other material. Further, the observed charged particle multiplicity M_{ch}, energy deposited per particle e, and total energy deposited E are affected by the efficiency of the detectors.

Finally, software is set–up to simulate the detector responses to energy deposition in the active elements, which then can be feed into the normal reconstruction software also used to analyse 'real' data, to give the experimentalist a further check on the quality of the analysis chain. Figure 6.1 shows this in graphical way, including the feed–back to theory.

[1] As vanilla is a rather uncharacteristic (but nice) taste, it is appropriate to use that term to qualify the 'bare' model data — that is, without any extra ingredients. If nothing else, the term is sure to raise a smile or two, just like vanilla ice–cream.

[2] See also Section 2.2.3

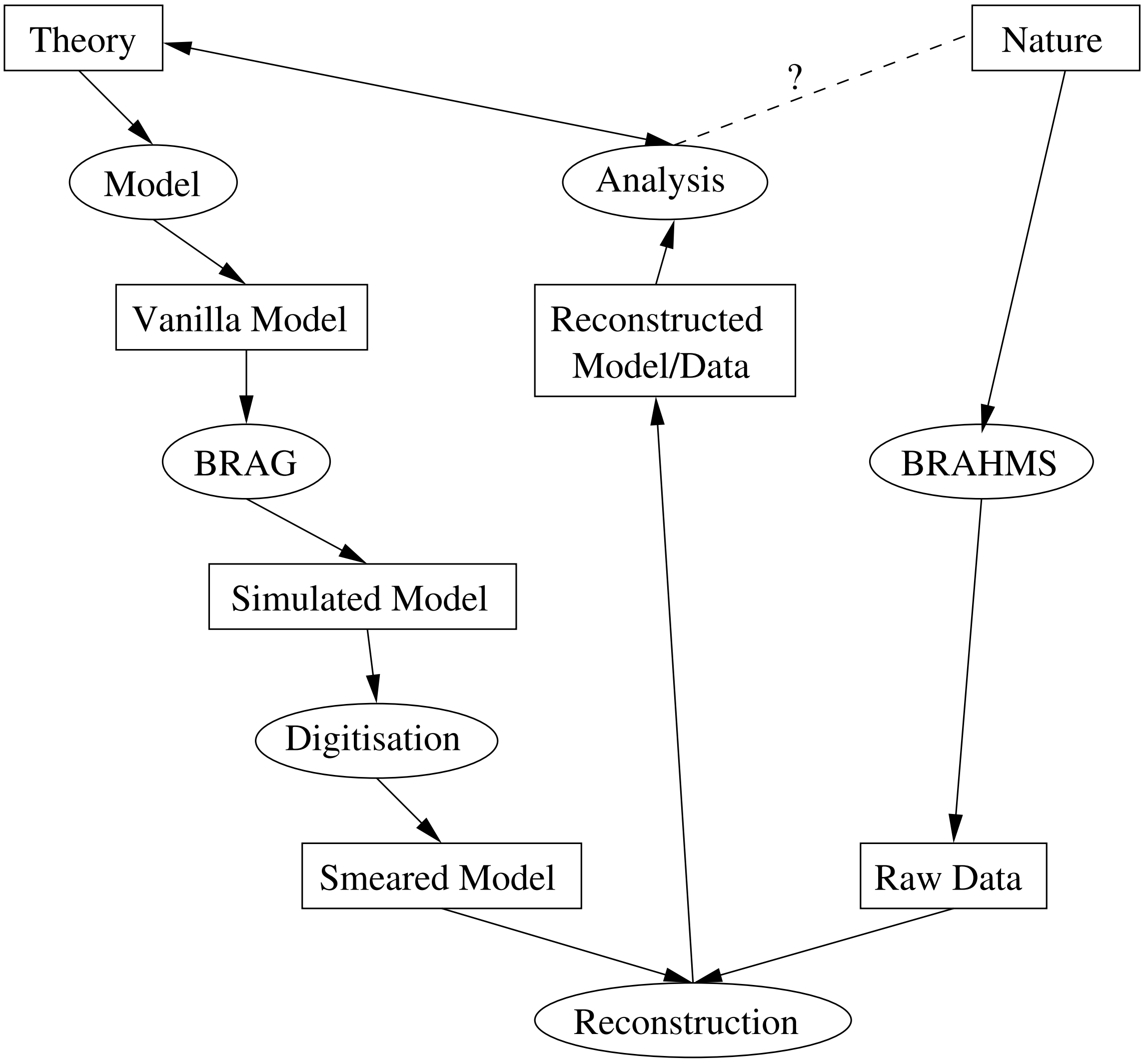

Figure 6.1: Analysis chain for both collision and model data.

6.1.1 Vanilla Model Data

The HIJING model has been used to generate 6000 events with an impact parameter in the range of 0-8 fm. Using a centrality determined as outlined in Section 5.3.3, and shown on Figure 5.8, the impact parameter b can be mapped monotonically into a centrality c. The vanilla model data is binned as the collision data (see Table 5.2) and analysed to obtain $\overline{M}_{\mathrm{ch}}$, $\omega_{M_{\mathrm{ch}}}$, $\bar{n}$, and ω_n [3]. In the analysis of the vanilla model, the number of participants is taken to be the number of sources n.

Solving (3.12) for ω_m, the fluctuation in number of particles produced per source ω_m can be calculated directly.

$$\omega_m = \omega_{M_{\mathrm{ch}}} - \overline{M}_{\mathrm{ch}} \frac{\omega_n}{\bar{n}} \tag{6.1}$$

The distribution of ω_m as a function of pseudorapidity η and centrality c is shown on Figure 6.2.

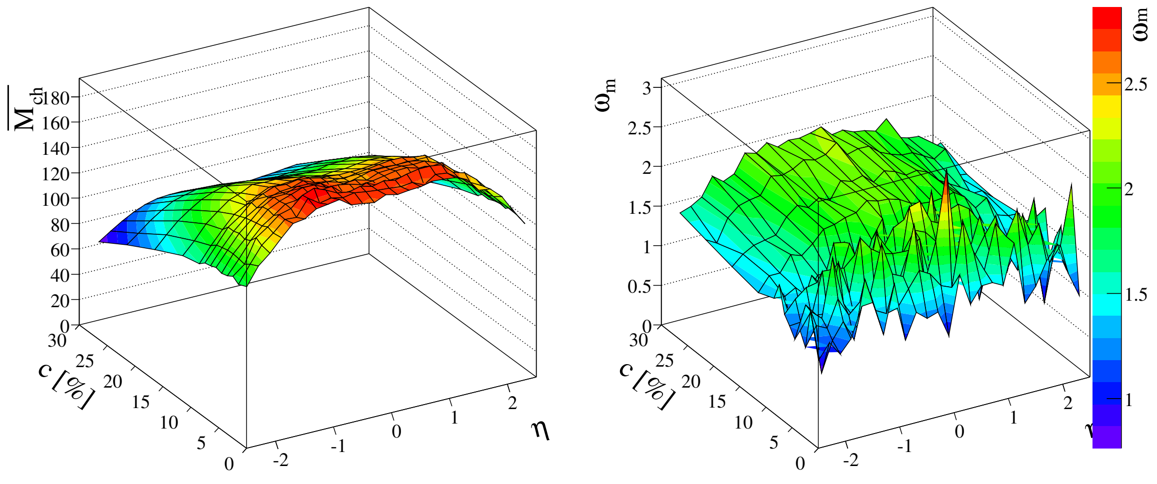

(a) (b)

Figure 6.2: (a) Average total charged particle multiplicity $\overline{M}_{\mathrm{ch}}$ and (a) fluctuation in number of particles produced per source ω_m in the vanilla HIJING data, calculated using (6.1).

As can be seen from the figure, the fluctuation is ≈ 1.5 and fairly constant over η and c. Hence, the HIJING model produces particles in an almost Poissonian manner. Also, it is important to note that the factor $\frac{\omega_n}{\bar{n}}$ in (6.1) is *very* small, as is evident from Figure B.1.

6.1.2 Simulated Model Data

Next, the vanilla model data is feed into the detector simulation, BRAG, to see how acceptance and efficiency of BRAHMS affects the fluctuations. As the SMA is azimuthal asymmetric, the HIJING events are reused to by rotating them 36°. Hence a total of 60,000 events has been send through BRAG.

The z coordinate of the collision point v_z, has been smeared with a Gaussian with a realistic mean and spread. However, the v_z is 100% determined in the analysis, and does not contribute

[3] See Appendix B.3 and Figure B.1 for the plots

in anyway, other than it gives a realistic acceptance and efficiency. The centrality c is again obtained from the impact parameter b via Figure 5.8(d).

BRAG records the particles that hit a given active detector element in the simulated environment. BRAGs concept of a 'hit' is that the particle deposits energy in the element, so particles that go straight through a detector element without any interactions at all, are not recorded as having hit an element. The number of particles hitting an element can simply be counted to make the $\omega_{M_{\mathrm{ch}}}$ distribution. The total count for a given η, φ, c is then corrected for the acceptance as shown in (5.5).

Again using (6.1), and the result[4] obtained for ω_n and $\bar{n}$ from the vanilla model, ω_m within the acceptance of the SMA is calculated, and Figure 6.3 shows the result.

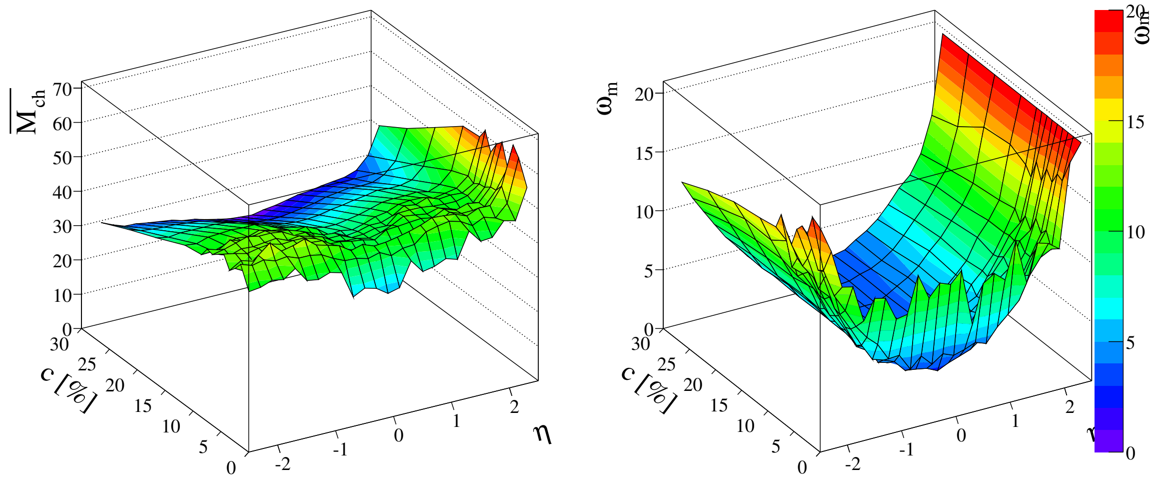

(a) (b)

Figure 6.3: (a) Average total charged particle multiplicity $\overline{M_{\mathrm{ch}}}$ and (b) fluctuation in number of particles produced per source ω_m in the acceptance of the SMA, calculated using (6.1).

The first thing to note, is that the shape of the $\overline{M_{\mathrm{ch}}}$ distribution in Figure 6.3(a) is very different from that of Figure B.3(b). However, observing that the simulated data contains contributions from secondary particles produced after the chemical freeze–out, this can easily be understood. In particular, particles that has a high pseudorapidity traverses a much thicker beryllium beam–pipe than those with a pseudorapidity around 0. Hence, particles moving forward and backward has a much higher cross section for producing secondary particles in the beam–pipe than those moving more outward. Figure 6.4 shows the ratio

$$\frac{M_{\mathrm{primary}} - M_{\mathrm{secondary}}}{M_{\mathrm{primary}}}$$

in the SMA as a function of η. The fit is a second degree polynomial with the linear term forced to 0.

As can be seen from the figure, the secondaries contribute with 14 % background at $\eta \approx 0$ increasing to 35 % at $\eta \approx 2.5$. This fits well with the qualitative difference in shape between Figure 6.2(a) and Figure 6.3(a). However, the *quantitative* difference is enhanced in the simulated data. That is, in the simulated data there are too many particles, as secondaries are

[4]Details can be found in Figure B.2.

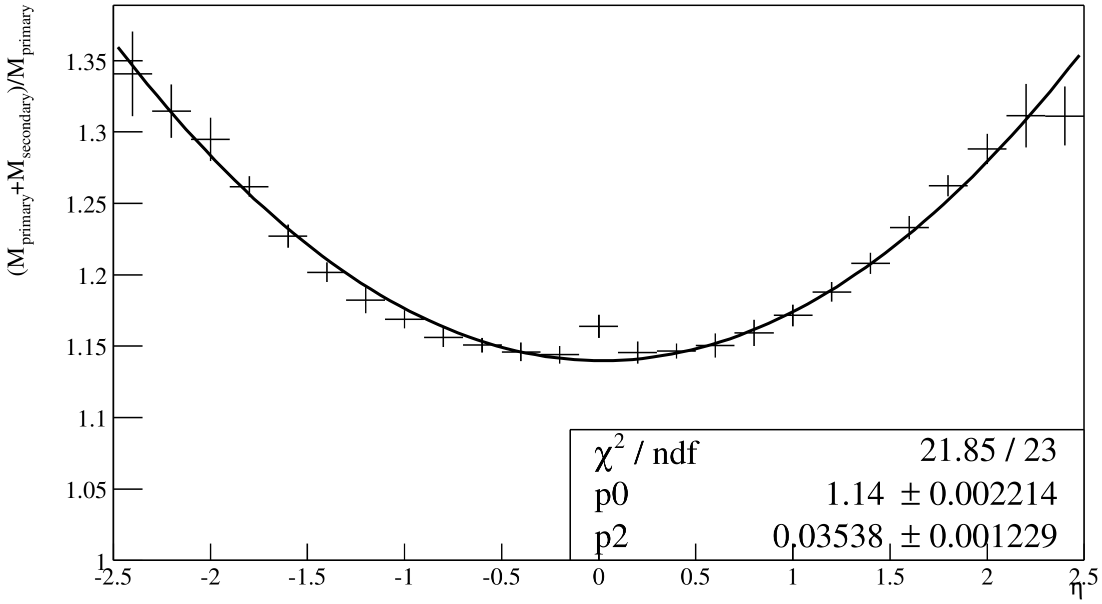

Figure 6.4: $\frac{M_{\text{primary}}+M_{\text{secondary}}}{M_{\text{primary}}}$ in the SMA.

counted too, but the overall level is too low, by $\approx 50\,\%$ after correcting for the secondaries. This indicates that the SMA has a detecting efficiency of $50\,\%$.

6.1.3 Range and Energy Loss in Silicon

The range of charged particles, losing energy only through ionisation, in matter is the average length the particle must travel before it comes to a halt [1,64]. The range of a material therefor gives an idea of how probable it is for a charged particle to deposit energy in a given medium. Figure 6.5(b) gives the range for various materials and particles.

Using the data in [65][5] for silicon, and that the SMA crystals are $300\,\mu$m thick, the range of particles as a function of $\beta\gamma$ can be calculated. The resulting curve is shown in Figure 6.6(b).

Reading off Figure 6.5(a) gives a range of 70 cm for a 0.5 GeV pion in Silicon (0.5 GeV is roughly the mean $p_\perp$ at $\sqrt{s_{NN}} = 130\,\text{GeV}$ at RHIC [55], and similar for $\sqrt{s_{NN}} = 200\,\text{GeV}$). That, and that the nuclear collision and interaction lengths are $70.6\,\text{gcm}^{-2}$ and $106\,\text{gcm}^{-2}$, giving an mean free collision and interaction path of 30 cm and 45 cm. Hence, very few particles that hit the SMA need interact at all in the silicon. The detecting efficiency of around $50\,\%$ can therefor easily be understood.

Further, as there are many dead areas in $(\eta, \varphi) \in [-2.5, 2.5] \cup [0^\circ, 360^\circ]$ in the acceptance of the SMA, the simple geometrical scaling given in (5.6) may simply underestimate the number of particles.

On Figure 6.5(a) the universal curve for the energy loss dE/dx (in units of $\text{MeVg}^{-1}\text{cm}^2$) by charged particles in various kinds of matter is given. Again, using the data of [65], and that the Silicon crystals in the SMA are $300\,\mu$m thick, the energy loss as a function of $\beta\gamma$ in a SMA element is evaluated and shown on Figure 6.6(a).

Silicon crystals has a density of $2.33\,\text{gcm}^{-3}$, close to that of of aluminium ($2.7\,\text{gcm}^{-3}$) [1]. Table 6 in [1] gives $1.664\,\text{MeVg}^{-1}\text{cm}^2$ for a minimum ionising particle in silicon. This gives an

[5] Also available electronically from `http://pdg.lbl.gov/AtomicNuclearProperties`.

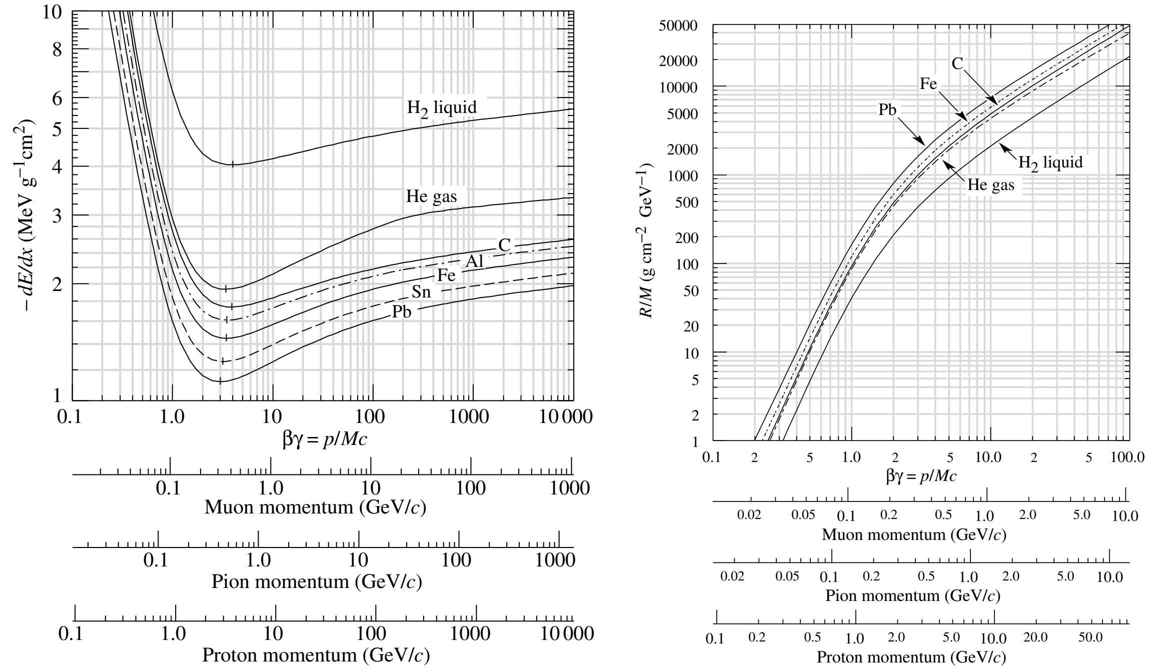

(a) (b)

Figure 6.5: (a) Energy loss and (b) range of charged particles in various materials. Both from [1].

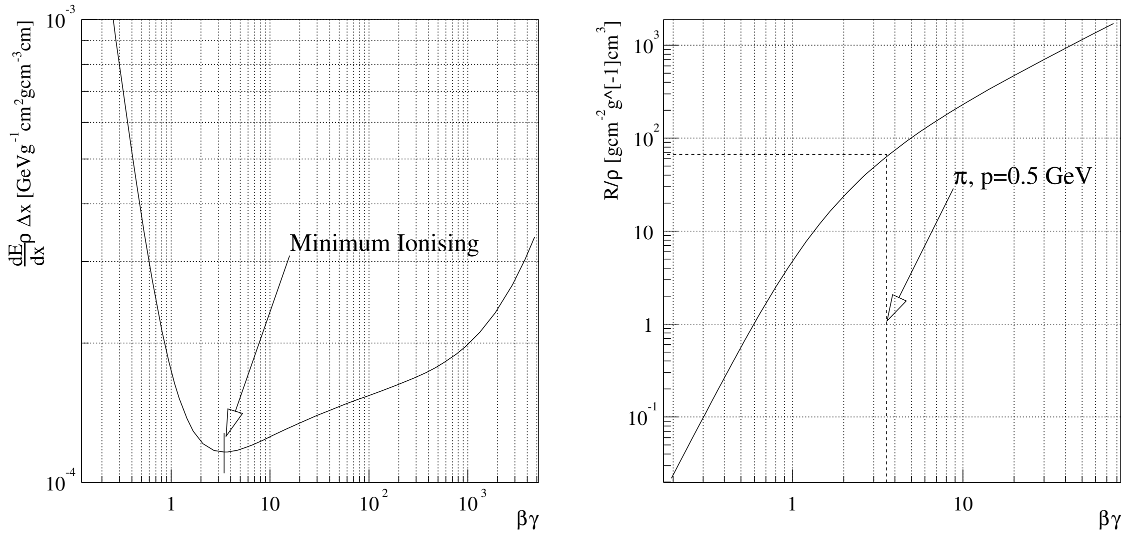

(a) (b)

Figure 6.6: (a) Energy loss and (b) range of charged particles in 300 μm Silicon. Note that the graphs are from μ data [65], hence the rise in dE/dx around the μ critical energy of 3.61 TeV corresponding to $\beta\gamma \approx 1000$.

expected energy deposition of a minimum ionising particle in a SMA element of

$$\begin{aligned}\bar{e}_{\mathrm{MIP}} &= 1.664\,\frac{\mathrm{MeV}}{\mathrm{g/cm^2}} 2.33\,\frac{\mathrm{g}}{\mathrm{cm^3}} 300\,\mu\mathrm{m} \\ &= 1.664\,\frac{\mathrm{MeV}}{\mathrm{g/cm^2}} 2.33\,\frac{\mathrm{g}}{\mathrm{cm^3}} 0.03\,\mathrm{cm} \\ &= 0.116\,\mathrm{MeV} = 0.000116\,\mathrm{GeV} \quad , \end{aligned} \tag{6.2}$$

in agreement with that shown on Figure 6.6(a).

Note, however, that this assumes that the particle impinges SMA element perpendicular to its surface. As explained in Section 5.3 this is not true of all particles, and the energy measured in the SMA must be corrected by a $\sin\vartheta_i(v_z)$ factor.

6.1.4 Secondaries

The shape of Figure 6.3(b) is different from those of Figure 6.2(b). As said previously, the difference between those two plots, are that the vanilla HIJING events have been sent through BRAG. BRAG imposes the acceptance and efficiency of the BRAHMS, and therefor also the SMA, on the data. But BRAG also generates secondary particles via interaction in matter and decay of short lived particle. These secondary particles are mainly produced at high $|\eta|$, where the particles traverses a longer path of matter in the beryllium beam pipe[6].

Figure 6.7(a) shows the relative increase in the fluctuations when counting both primary and secondary particles, relative to just counting primary particles. From that plot, it is clear, that the secondary particles contribute mainly at high $|\eta|$, where there are more of them (see Figure 6.4). However, the increase in number at $\eta \approx 0$ is 14 %, while the increase in the fluctuations are more like 20 %. Also, at $|\eta|$ the increase in number was 35 %, while the increase in the fluctuation is more like 50 %.

However, the level of Figure 6.3(b) is higher than that of Figure 6.2(b). In particular the high and low η regions are much enhanced, and the plateau in mid-region is $\approx 100\,\%$ higher, increasing to $\approx 250\,\%$ at $\eta = 1$. See also Figure 6.7(b).

The large increase at the high and low psuedorapidities are largely due to the limited acceptance and statistics in those regions. As $|\eta|$ becomes larger, each SMA element extends over smaller and smaller η regions, and so the statistics go down, and the error introduced by scaling up to bin sizes becomes larger. The latter is not a problem if the sample is large enough, but in the present case of simulated data where only 60 000 events was analysed, it does matter.

However, the large increase is hard to understand, and can be due to many factors in the experiment. As such, they constitute unidentifiable effects that can be corrected for, with the reservation that the result is highly dependent on the particularities of the input model (here HIJING), and the accuracy of the detector simulation.

Secondary particles are largely created by stochastic processes, like decay or interaction in matter. The resulting fluctuation in the charged particle number, is then a folding of all these stochastic processes. This raises the level of the fluctuations over the full range of η, though but more so in the forward and backward regions (see Figure 6.4).

[6]Note that primary particles may change momentum vectors as a result of elastic scattering, leading to changes the particles η.

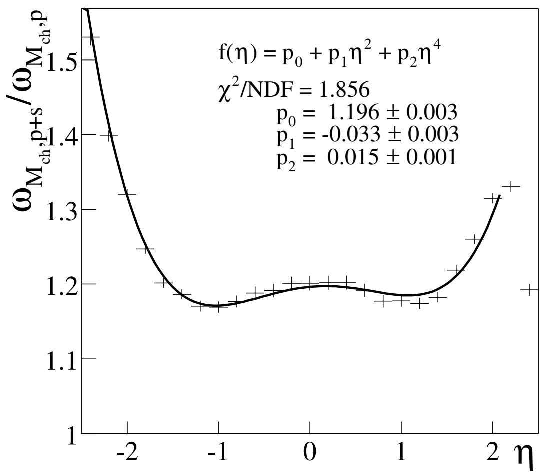

(a)

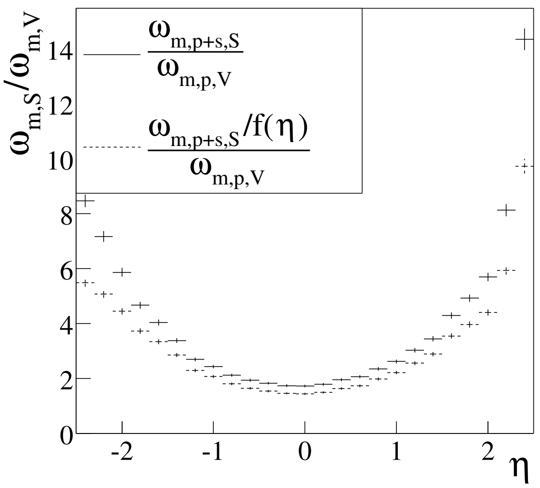

(b)

Figure 6.7: (a) Relative increase in $\omega_{M_{\rm ch}}$ when counting both primary and secondary particles ($\omega_{M_{\rm ch},p+s}$) relative to just counting primary particles ($\omega_{M_{\rm ch},p}$). The points at $\eta > 2.1$ deviate mainly due to missing wafers at the end of the array, leading to poorer statistics, and hence much larger spread. (b) The relative increase in ω_m from the BRAG simulation over the vanilla HIJING. The dashed curve shows the relative increase, when only counting primary particle in the simulated data.

6.1.5 Fluctuations in Energy Deposited from BRAG

In addition to recording the particles that hit each detector element in the simulated environment, BRAG also records the energy deposited per particle in a given detector element. Hence, ω_e and $\bar{e}$ as they appear in (3.17) can be evaluated on the simulated model data[7]. Solving (3.17) for ω_m gives

$$\omega_m = \frac{\overline{M_{\rm ch}}}{\overline{E}}\left(\omega_E - \omega_e\right) - \frac{\overline{E}}{\bar{e}}\frac{\omega_n}{\bar{n}} \quad , \tag{6.3}$$

which by direct application allows evaluation of ω_m, as shown on Figure 6.8.

It is seen, that the $\overline{E}$ distribution follows nicely the $\overline{M_{\rm ch}}$ from the vanilla model (Figure 6.2(a)). The level of $\overline{E}$ is higher than if all particles were minimum ionising. However, the mean energy deposited per particle in the SMA is not 0.116 MeV but rather goes from 0.125 MeV at high $|\eta|$, increasing to 0.22 MeV around $\eta = 0$ [8].

The ω_m calculated via (6.8) is *much* higher than that of from the vanilla model, *and* the from the charged particle multiplicity as observed in BRAG. For the ω_m calculated via (6.8) to agree with that calculated from vanilla model, the fluctuation in the energy deposited per particle should be around a factor 10 higher, or the fluctuation in total energy deposited ω_E should be around a factor of 10 lower. The second term on the right hand side of (6.8) is so small due to the factor $\frac{\omega_n}{\bar{n}}$ that it has no chance of outweighing the large factor $\frac{\overline{M_{\rm ch}}}{\overline{E}}$ in the first term.

That indicates, that the assumptions leading up to (3.17) in Section 3.2.4 are not valid. In particular, the factoring of $\overline{E}$ into $\overline{M_{\rm ch}}\bar{e}$ is dubious. That is not entirely surprising.

[7] See Figure B.2 in Appendix B.3 for more details.
[8] See also Figure B.2(c).

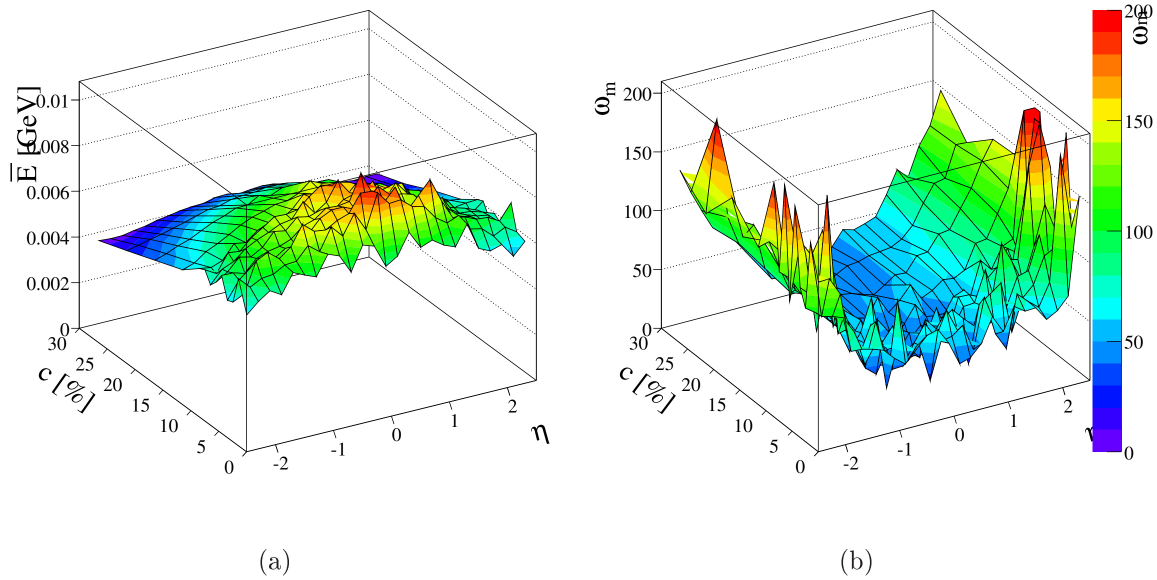

Figure 6.8: (a) Average energy deposited $\overline{E}$ and (b) fluctuation of the number of particles produced per source ω_m in the acceptance of the SMA, calculated using (6.3).

The SMA operates in an *integrating mode*. That is, in every event, each of the elements in the SMA integrates over a large sample of particles, adding the contributions from each particle into the total energy deposited E of the event. The distribution of energy loss per particle *and* the number of particles hitting the detector elements, are *both* very important for the total energy loss in the element, and therefor not necessarily independent. If the SMA was operating in *counting mode*, where any signal can be identified as *one* particle hitting the element, the situation is entirely different, as the analysis is no longer sensitive to the distribution of the energy loss per particle, and the complications that follow.

As described in Section 5.3, when analysing the data from the Au+Au collisions, the charged particle multiplicity in a given SMA element is extracted from the sum energy signal in the element. Hence, the charged particle multiplicity is sensitive to the above effects, and it is not reasonable to expect that the SMA will give credible results, simply because if its integrating nature.

6.2 Reconstructing the BRAG Simulation Data

As a further check of the procedure, the simulated data output from BRAG is sent through a digitisation step, as shown on Figure 6.1. In this step, the hits in the active elements in the simulated environment is transformed into the same format as that which is produced by the DAQ. The detector electronics is simulated by applying the inverse gain factor, and adding the pedestal value to give a simulated ADC count for each SMA element. As the ADC apparatus has some intrinsic fluctuation in the ground level, or pedestal, typically 1-3 counts wide, a random smearing of the pedestal can be introduced. Finally, the saturation effect of the ADCs are also simulated.

Having brought the simulated data into a format matching the DAQ format, it is sent through the normal analysis chain used in the BRAHMS, called BRAT[9]. BRAT tries to reconstruct

[9]See also Appendix B.

the energy deposited in each SMA element, and from that, number of particles that hit each element. See also Section 5.3 for more on this.

In the reconstruction of the BRAG data, the centrality c and vertex z–coordinate v_z used are the same as the ones used in analysing the vanilla and simulated data. That means that there's no ambiguity in v_z, and the event selection is consistent with the previous two steps. Figure 6.9 shows the result of this analysis[10].

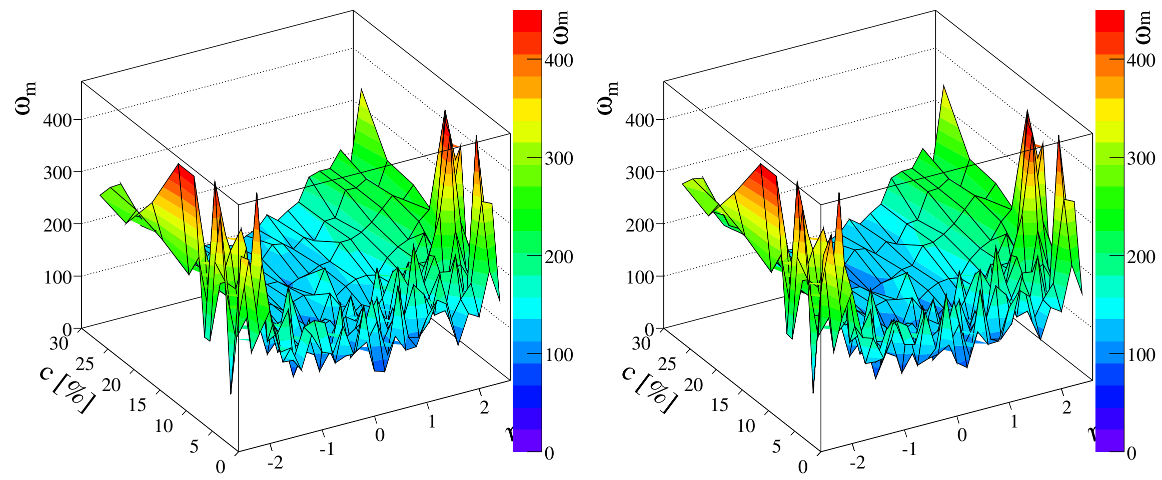

(a) (b)

Figure 6.9: (a) ω_m from reconstructed simulation data calculated using (6.1), and (b) and using (6.3)

The good news here, is that the ω_m derived from the total energy deposited and the from the charged particle, are roughly the same (less than 5 % difference). That is not surprising, as the reconstructed charged particle multiplicity is derived from the total deposited energy, as outlined in Section 5.3.

The bad news, is that the level is again higher ($\approx 100\,\%$ higher) than that from both the vanilla and the simulated data. This applies whether or not the pedestal was smeared or not. The reason for this, is that in the reconstruction, elements of the SMA that are *saturated* — that is, the counter that in ADC apparatus has reached its upper limit — are disregarded. That lowers the average energy deposited $\overline{E}$, and thereby raises the fluctuation ω_E. As the charged particle multiplicity is derived from the energy, this effects the $\overline{M_{\mathrm{ch}}}$ and $\omega_{M_{\mathrm{ch}}}$ similarly. Again, this is due to the integrating nature of the SMA. If the SMA was operating in counting mode, then any hit would be valid, and the event sample would not be biased by limitations in the electronics.

6.3 Comparison of Vanilla to Reconstructed Model Data

Noting that ω_e separates out the detector energy response characteristics and particle momentum distribution (see Section 3.2.5), and that $\frac{\omega_n}{\bar{n}}$ separates out the variations due to varying collision conditions, what is left in (3.17), is ω_m the particle produced per source. However, this is contaminated by secondaries and other unidentifiable detector characteristics. It is therefor

[10]Figure B.3 shows $\overline{M_{\mathrm{ch}}}$ and $\overline{E}$ from this analysis.

interesting to compare the ω_m of simulated data (Figure 6.3(b)) to that of the vanilla model (Figure 6.2(b)). The ratio $\frac{\omega_{m,S}}{\omega_{m,V}}$ contains exactly these unidentifiable contributions relative to the bare 'true' ω_m of the model.

Hence, knowing that ratio, it is possible to correct real data for these unidentifiable contributions.

$$\omega'_m = \omega_m \frac{\omega_{m,S}}{\omega_{m,V}} \tag{6.4}$$

However, it is important to realise that the ratio is dependent on the particle/momentum distribution of the input vanilla model (here HIJING), the detector simulation (here GEANT) as well of the sample size of simulated data:

- If the another model was chose, the number of particles may be entirely different and with a completely different energy distribution, resulting in some other number being recorded in BRAG as having hit a detector element. It is well–known that HIJING over–predicts the $\bar{p}/p$ and underestimates the width of the charged particle multiplicity in Au+Au at $\sqrt{s_{NN}} = 200\,\mathrm{GeV}$ [52, 66].

- If the detector simulation is wrong, it may result in wrongly accepting particles or a entirely different secondary particle production. However, GEANT has for some time now been thoroughly test in the high energy physics experimental community, and enjoys a great deal of respect there.

- Finally, if the sample size is too small, the spread of the distribution is poorly known, leading to problems in the scaling to the acceptance of the detector as explained above. In the present analysis, 60 000 events was used, giving between 500 and 1 500 counts in each η, c bin — a bit on the low side, resulting a $\frac{\omega_{m,S}}{\omega_{m,V}}$ that is probably slightly too high, especially at high $|\eta|$.

Chapter 7

Extracting the Fluctuations in Produced Particles per Source — ω_m

Chapter 6 showed the difficulties inherent in analysing the SMA data for fluctuations, both in terms of detector limitations, and underlying assumptions. As pointed out in that chapter, the problem is that it is hard to resolve the charged particle multiplicity based on the sum energy signal in the SMA elements. In this chapter, an alternative approach, where fits to the data are used, is evaluated. It turns out that this is no better than what could be expected from the discussion in Chapter 6.

7.1 $\omega_{M_{\mathrm{ch}}}$ as a function of $\overline{M_{\mathrm{ch}}}$

Using (3.12), and substituting $\overline{m} = \overline{M_{\mathrm{ch}}}/\bar{n}$, it is possible to express the measured $\omega_{M_{\mathrm{ch}}}$ as a function of the measured $\overline{M_{\mathrm{ch}}}$:

$$\omega_{M_{\mathrm{ch}}} = \omega_m + \overline{M_{\mathrm{ch}}}\frac{\omega_n}{\bar{n}} \tag{3.12}$$

Also, observing that for each η bin, that the centrality c maps into a unique $\overline{M_{\mathrm{ch}}}$, ω_M can be presented as a function of $\eta, \overline{M_{\mathrm{ch}}}$ rather than as a function of η, c. This is shown in Figure 7.1.

To extract the fluctuation in number of charged particles produced per source, the histogram in Figure 7.1 can be fitted to

$$f(x) = p_0 + xp_1 \quad , \tag{7.1}$$

in each η bin, where x is identified with $\overline{M_{\mathrm{ch}}}$, p_0 with ω_m and p_1 with $\frac{\omega_n}{\bar{n}}$. Four examples of these fits are shown in Figure 7.2.

The distribution of the parameters p_0, p_1, and the χ^2 per degree of freedom (NDF) is shown in Figure 7.3. The mean values of the parameters over η is shown in Table 7.1.

Parameter		*Value*: $\pm$ *Error*	χ^2/NDF
ω_m	p_0	74.2: $\pm$ 0.1	144.3
$\omega_n/\bar{n}$	p_1	-0.040: $\pm$ 0.002	64.5

Table 7.1: Results of fits of ω_m, and $\frac{\omega_n}{\bar{n}}$ to a constant.

As can be seen from Figure 7.3 and Table 7.1, the $\frac{\omega_n}{\bar{n}}$ is much higher than what could be expected from the HIJING model (see Section 6.1), and also there is a strong η dependence

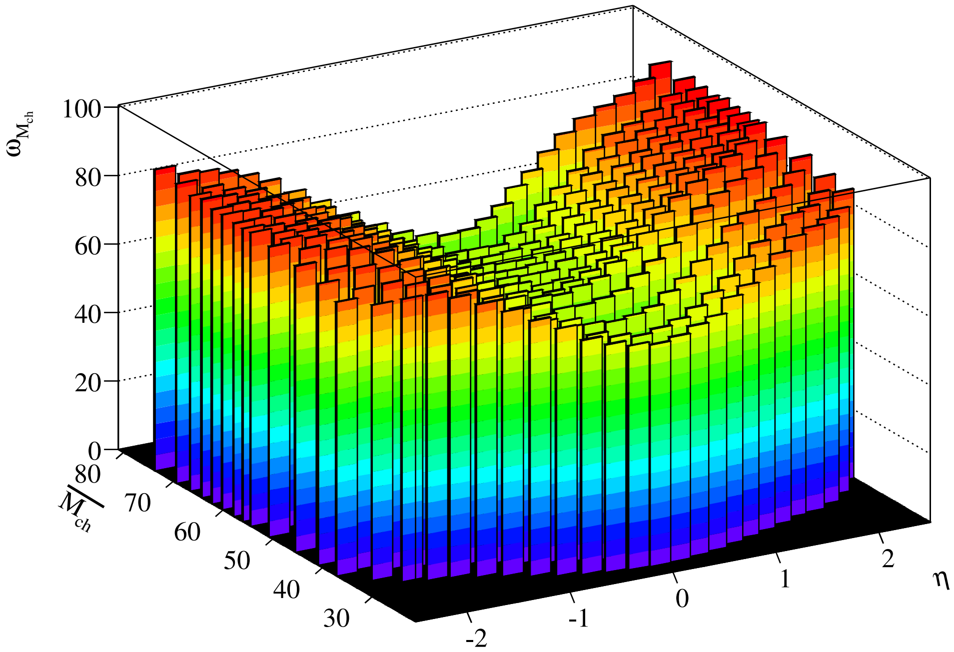

Figure 7.1: $\omega_{M_{\rm ch}}$ as a function of η and $\overline{M_{\rm ch}}$.

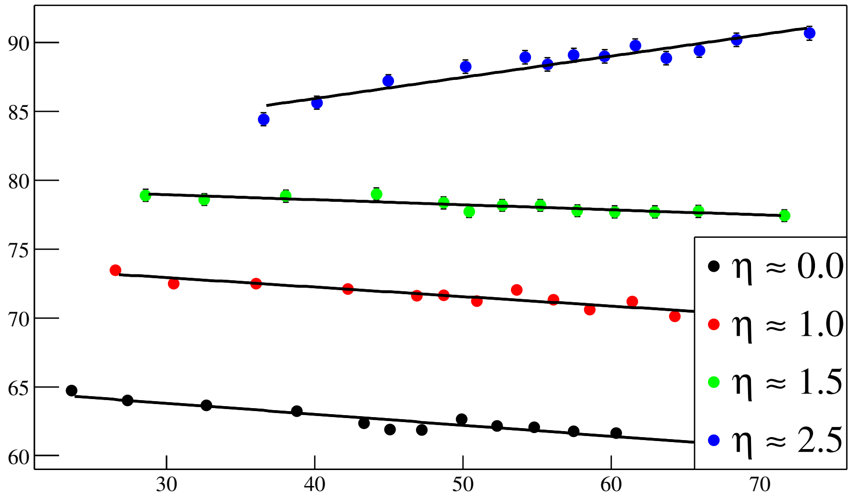

Figure 7.2: Fits to $\omega_{M_{\rm ch}}$ as function of $\overline{M_{\rm ch}}$ at $\eta \approx 0, 1, 1, 1.5$, and 2.5 in $\Delta\eta = 0.2$ bins.

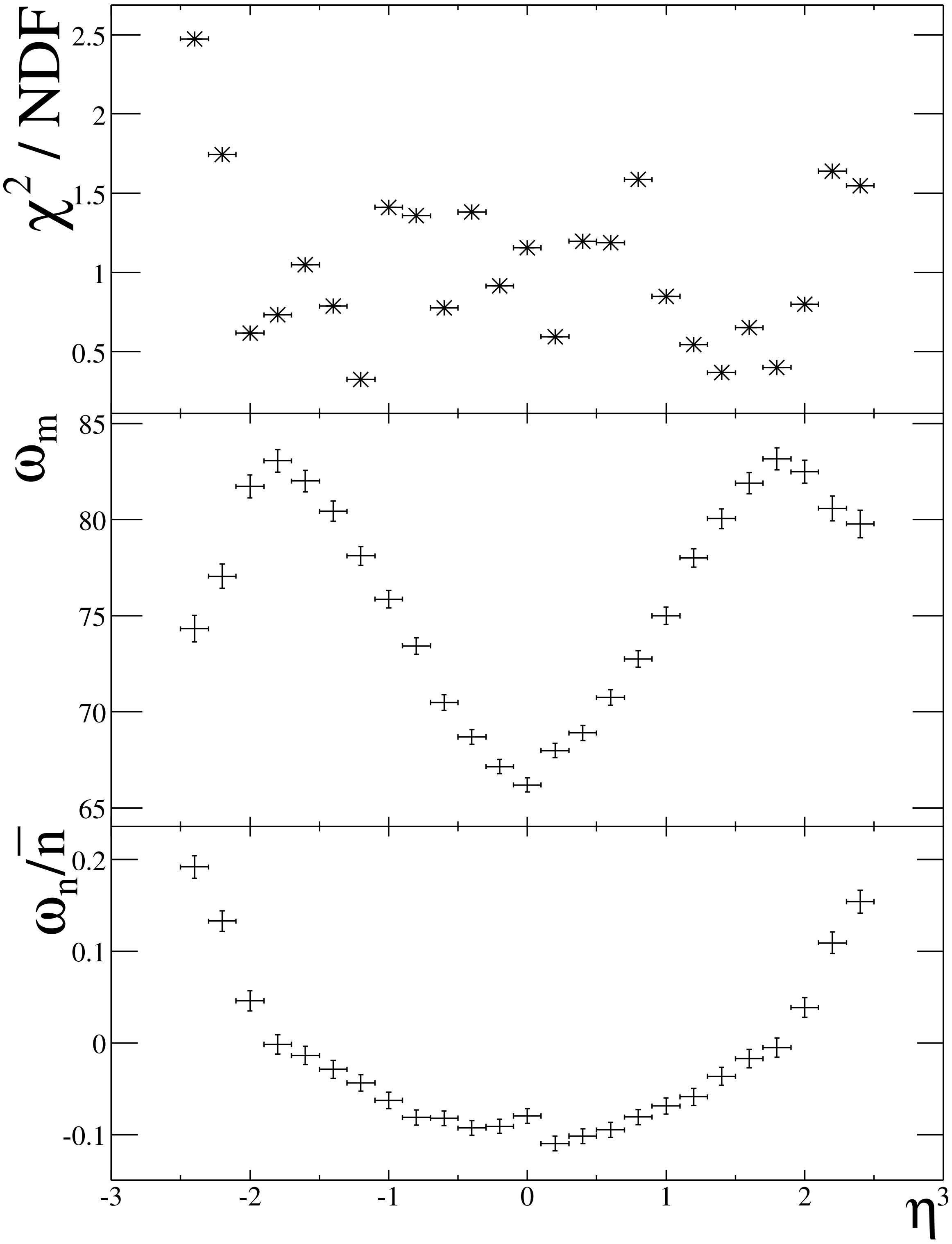

Figure 7.3: The χ^2/NDF and parameters of Figure 7.1 fitted in each η bin to (7.1). The average χ^2/NDF is ≈ 1.1.

which is hard to interpret: Taking the participants of the collision to be the sources, most of these sources will have an infinite, or very high $|\eta|$, as they are racing down the beam line. Hence, one would expect the distribution of the sources to be peaked at very high $|\eta|$ (higher than 2.5). This, and that $\frac{\omega_n}{\bar{n}}$ is negative in a large region, indicates that the value of $\frac{\omega_n}{\bar{n}}$ is driven by the fit optimisation, which is also evident from the confidence contour shown in Figure 7.4. (More is said on the negative $\frac{\omega_n}{\bar{n}}$ toward the end of this chapter.)

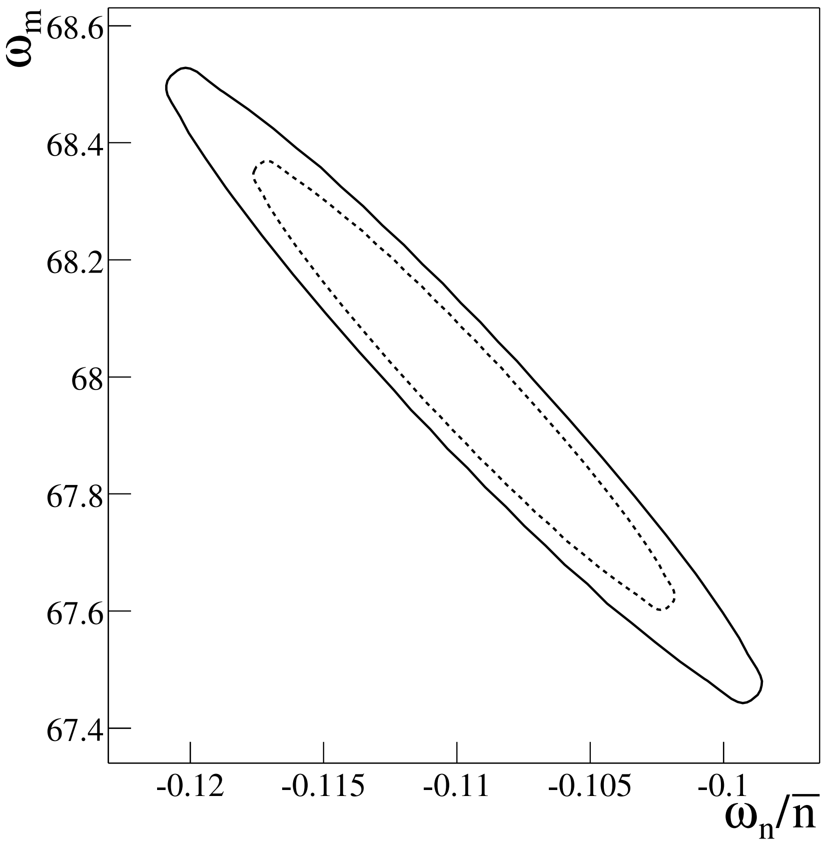

Figure 7.4: Example 2σ (full) and 1σ (dashed) confidence contour of ω_M versus $\frac{\omega_n}{\bar{n}}$ at $\eta \approx 0.1$. The contour shows the values of the parameters ω_M and $\frac{\omega_n}{\bar{n}}$ for which the χ^2/NDF changes by one unit.

Exemplified in Figure 7.4 are the 1 and 2σ confidence contours of ω_M versus $\frac{\omega_n}{\bar{n}}$, which show the strong anti–correlation of the parameters of the fit, meaning that if one increases, the other *must* decrease correspondingly. This, on the other hand, indicates that M_{ch} and n are *not* independent as conjectured in Section 3.2.2 — or that the SMA can not measure the M_{ch} well enough that it is independent from the centrality measured from the TMA. Given that we have no measurement of n, and the considerations brought forward in Section 6.1.5, the latter is the more credible of these consequences.

The overall level of ≈ 75 is on the same level as ω_m calculated using (6.3) from simulated summed energy data (see Figure 6.8(b)) and ω_m calculated using (6.1) from the reconstructed model multiplicity data (see Figure 6.9(a)). As the discussed there, in particular Section 6.2, the high level is grounded in the inadequate resolution in the SMA to resolve the spread of charged particle multiplicity distribution.

Now, given the problems of going from the summed energy signal in a SMA element to a charged particle multiplicity in that element, it is reasonable to ask if M_{ch} is really the right variable to look at, as it is after all derived from E. Section 7.3 will try to answer that, by using the summed energy signal E rather than the charged particle multiplicity M_{ch}. But first an aside needed for the subsequent analysis.

7.2 $\overline{M_{\text{ch}}}$ as a function of $\overline{E}$

From Section 3.2.4 we have that $\overline{M_{\text{ch}}} \propto \overline{E}$, and since $\overline{M_{\text{ch}}}$ is present in (3.17) it is desirable to know this relation. Therefor, for each η bin, pairs of $\left(\overline{E}, \overline{M_{\text{ch}}}\right)$ are fitted to the function

$$\overline{M_{\text{ch}}}(\overline{E}) = \overline{M_{\text{ch},0}} + \frac{1}{\bar{e}}\overline{E} \tag{7.2}$$

Some examples of these fits are shown in Figure 7.5[1].

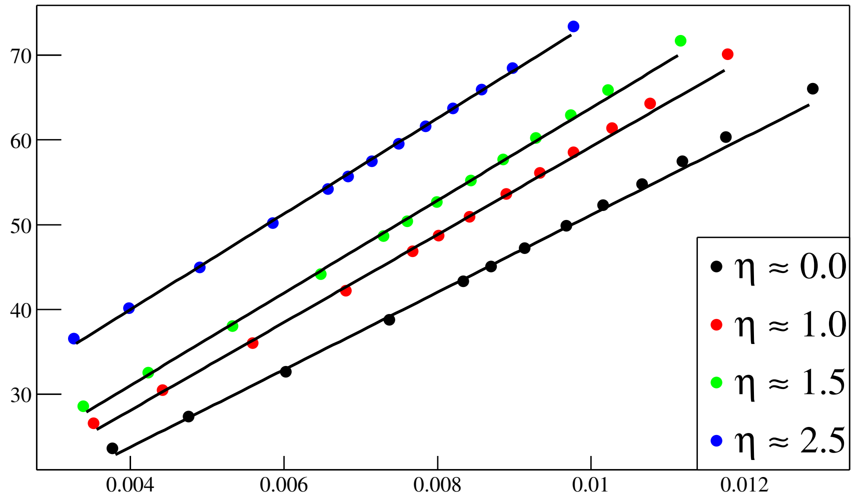

Figure 7.5: Example fits of $(M_{\text{ch}}, \overline{E})$ pairs in $\Delta\eta = 0.2$ bins.

As can be seen from the example fits, the relation between $\overline{M_{\text{ch}}}$ and $\overline{E}$ is nicely linear for a given η value. The parameters of the fits can now be used when evaluating ω_m from ω_E as expressed in (3.17).

7.3 ω_E as a function of $\overline{E}$

The equation

$$\omega_E = \omega_e + \frac{\overline{E}}{\overline{M_{\text{ch}}}}\left(\omega_m + \frac{\overline{E}}{\bar{e}}\frac{\omega_n}{\bar{n}}\right) \tag{3.17}$$

expresses the intrinsic fluctuations ω_m in the particle production as a function of the measurable quantities $\overline{E}$, $\overline{M_{\text{ch}}}$ and ω_E with the parameters: fluctuation in energy deposited per charged particle ω_e, average deposited energy per particle $\bar{e}$, fluctuations in number of sources ω_n and average number of sources $\bar{n}$. Since ω_E changes very little over $c \in [0\,\%, 30\,\%]$ and that $\overline{E} \propto \frac{1}{c}$ in that range (see Figure 5.12(b)), one can plot ω_E as a function of η and $\overline{E}$ rather than the measured c. This is shown in Figure 7.6.

[1] All the parameters from the fits are shown in Figure B.4.

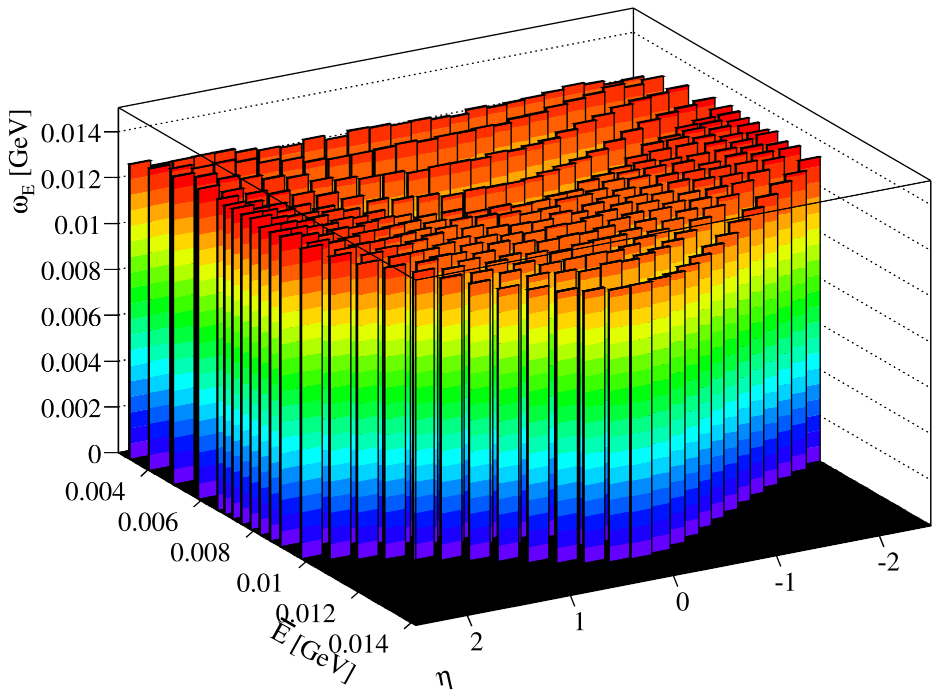

Figure 7.6: ω_E as a function of η and $\overline{E}$

To evaluate ω_m, the histogram in Figure 7.6 is sliced up along η, giving ω_E as a function of $\overline{E}$ for a given η. As shown in the previous section, $\overline{M_{\mathrm{ch}}} \propto \overline{E}$, we can change (3.17) to read

$$\omega_E = \omega_e + \overline{E}\frac{\omega_m}{\overline{M_{\mathrm{ch},0}} + \frac{1}{\bar{e}}\overline{E}} + \overline{E}\frac{\omega_n}{\bar{n}} \tag{7.3}$$

Each slice in η is fitted to the function

$$f(x) = p_0 + x\frac{p_1}{p_2 + xp_3} + xp_4 \tag{7.4}$$

where x is identified with $\overline{E}$, and p_2 and p_3 are constants for a given η, given by the fits mentioned previously. In this expression we can identify p_0 with ω_e, p_1 with ω_m and p_4 with $\frac{\omega_n}{\bar{n}}$. Four examples of these fits are shown in Figure 7.7. The result of these fits, along with the χ^2 per degrees of freedom (NDF) are shown in Figure 7.8, and Table 7.2 summarises the average, spread and χ^2/NDF of $\overline{M_{\mathrm{ch}}}$, ω_m, and $\frac{\omega_n}{\bar{n}\bar{e}}$ from the fits.

Parameter		*Value*: $\pm$ *Error*	χ^2/NDF
ω_m	p_1	18.0: $\pm$ 1.3	9.3
$\omega_n/\bar{n}$	p_4	-0.136: $\pm$ 0.006	2.8
ω_e	p_0	0.0106: $\pm$ 0.0001	6.8

Table 7.2: Results of fits of ω_m, $\frac{\omega_n}{\bar{n}}$ and ω_e to a constant.

On the average, ω_e is seen to be one order of magnitude to bigger than the results from the BRAG simulation (see Figure B.2(b)).

As previously explained, the ω_e term encodes the detector response characteristics and fluctuations in energy deposited per particle due to slow particles. Hence, if ther are more slow particles than predicted in HIJING and BRAG, that would explain the increase.

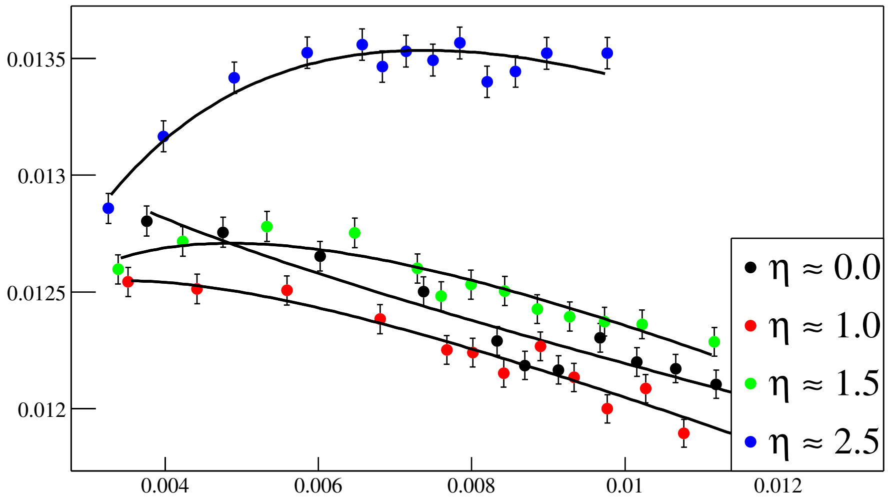

Figure 7.7: Fits to ω_E as function of $\overline{E}$ at $\eta \approx 0, 1, 1.5$, and 2.5 in $\Delta\eta = 0.2$ bins.

Note, that the relatively large value of ω_e can be attributed to the integrating nature of the SMA. In general, a charged particle deposit energy according to a Landau distribution. That distribution may have a very long tail, which is truncated by the detector read–out (ADC overflow or saturation). When a detector is integrating, then the total energy deposited is a folding of the individual Landau distributed contributions from each particle. That greatly increases the width of the response function, and thereby the extracted fluctuation ω_e. There is no way that the fitting procedure can unfold the individual contributions to get a more true variance.

As can be seen from the example fits in Figure 7.7, ω_E decreases with increasing $\overline{E}$ (or decreasing c). Hence, the term xp_4 in (7.4) must be decreasing, making $\frac{\omega_n}{\bar{n}}$ negative. This gives one pause to think what may lead to this odd result.

If, contrary to the assumption in Section 3.2.2, the number of particles produced is anti–correlated with number sources, then the cross term[2]

$$C_{n,m} = \frac{1}{N}\sum_{k}^{N}(n_k - \bar{n})(m_k - \overline{m}) \quad ,$$

may become negative. This means that the fluctuations will drop as the number of source increases, or equivalently — the centrality falls. Then, the average of the total multiplicity would become

$$\overline{M_{\mathrm{ch}}} = \overline{m}\bar{n} + C_{mn} \quad ,$$

and an additional terms would be present in (3.17), all proportional to C_{mn} that is potentially negative. Hence, the assumption of independent particle production of the sources, does not seem to hold.

In Figure 7.9 shows typical examples of 1 and 2σ confidence contours for the three parameters ω_m, $\frac{\omega_n}{\bar{n}}$, and ω_e. Again, the parameters are strongly (anti–) correlated with each other, making the assumptions of Section 3.2.2 and Section 3.2.4 — that M_{ch}, n, E and e are independent dubious.

As explained in Section 3.5 this is an indication that something other than pure statistical production is going on in the Au+Au collisions. That the parameterisation of (3.17) does not

[2]See also Appendix A.2.

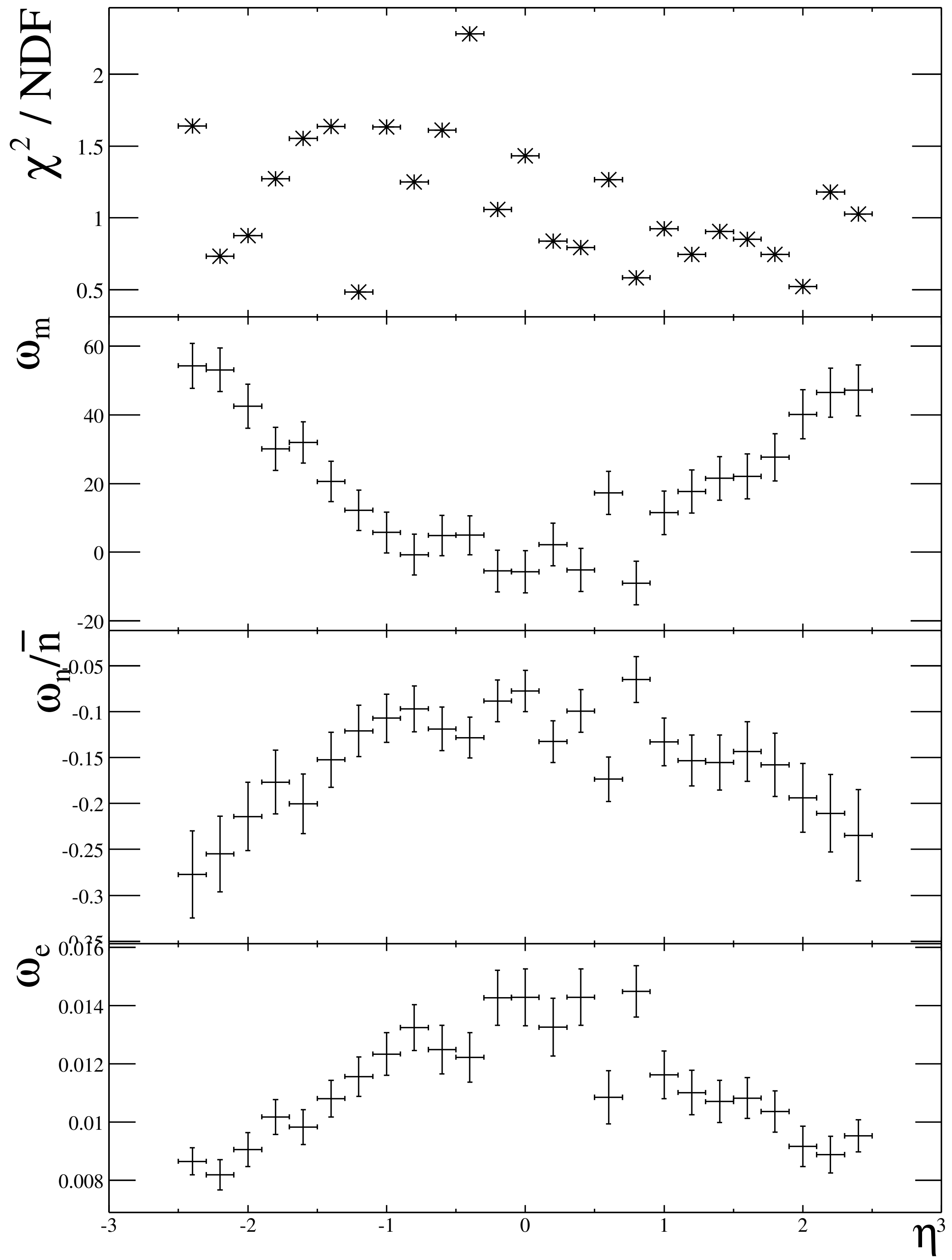

Figure 7.8: The χ^2/NDF and parameters of Figure 7.6 fitted in each η bin to (7.4). The average χ^2/NDF is ≈ 1.1.

give credible results, indicates the simple picture — of independent particle production and energy deposition — leading up to that expression is wrong.

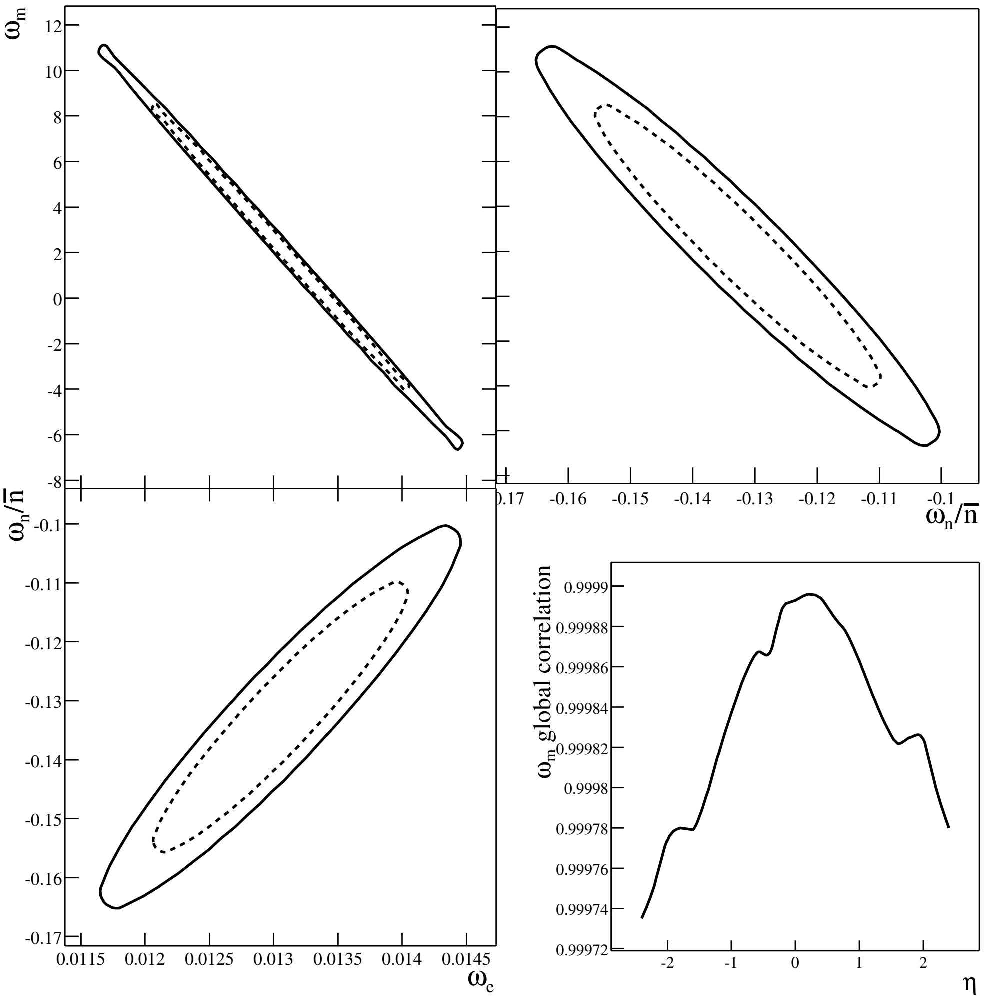

Figure 7.9: Example 2σ (full) and 1σ (dashed) confidence contours at $\eta \approx 0.1$ for ω_m versus ω_e (top–left), ω_m versus $\frac{\omega_n}{\bar{n}}$ (top–right), $\frac{\omega_n}{\bar{n}}$ versus ω_e (bottom–left), and correlation coefficient of ω_m for all η.

7.4 Comparison to HIJING Data

As explained in Section 6.3, the BRAG detector simulation can in principle be used to evaluate any unidentifiable contributions to the fluctuations in particles produced per source ω_m, to obtain a bare ω'_m by

$$\omega'_m = \omega_m \frac{\omega_{m,S}}{\omega_{m,V}} \quad . \tag{6.4}$$

However, as stressed in that section, this interpretation of ω'_m is highly model dependent.

Figure 7.10 shows the result of applying (6.4) (where the ratio is that in Figure 6.7(b)) to ω_m from Figure 7.8.

As can be seen from Figure 7.10 the bare fluctuations are, averaged over η, 4.3 ± 0.3 at with a rather poor χ^2/NDF of 1.7. The point at $\eta \approx 2.4$ (right most point) has been omitted from the fit, as it is dominated by the unexplainable raise at high η in Figure 6.7(b).

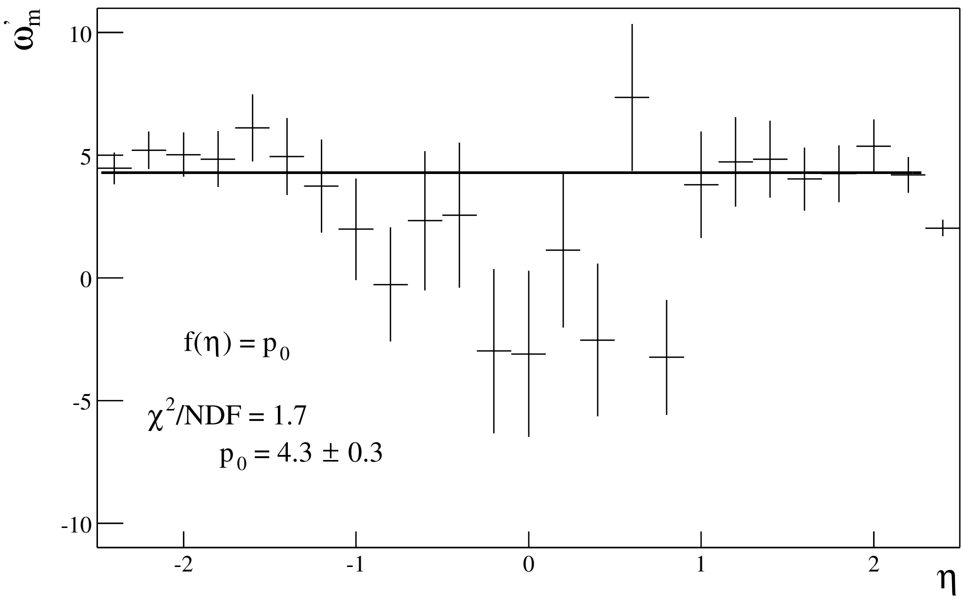

Figure 7.10: ω_m (from Figure 7.8) adjusted for secondary particle production, geometrical and detector acceptance, as well as other unidentifiable sources of fluctuations.

The main cause of errors in the figure, is the error on ω_m in Figure 7.8. The fact that it is not as smooth as one may have hoped shows up again in the bare ω_m, and is the main reason why the constant fit is relatively poor.

Assuming that the model calculations are sound, the value of η, 4.3 ± 0.3 is far above the Poissonian value of 1, and in between the value of 6.3 expected from KNO scaling at $\sqrt{s_{NN}} = 200\,\text{GeV}$, and the value of 1.4 from a thermal source (see also Figure 3.1(b)). Hence, the conclusion of the analysis is, that in terms of fluctuations, Au+Au collisions at relativistic energies behaves much like scaled N+N collisions. However, the level is not high enough to suggest that a transition to chiral symmetric and deconfined matter has been achieved, which would most probably result in fluctuations orders of magnitude higher [36].

Chapter 8

Conclusion

A large sample of central to semi central events have been analysed to look for fluctuations in the particle production per source (ω_m). However, the analysis of the data and in particular the simulated data show that the SMA of BRAHMS, is not really well suited for this task, as there is a large correction to the extracted ω_m which must be applied to obtain the 'bare' ω_m of the interactions.

While the SMA gives good results for the first moment (the average) of charged particle distribution over a large sample of events, the integrating nature of the detector plus the long Landau tail in the energy spectrum, makes the measurement of the second (the spread) and higher moment of the charged particle distribution very difficult. The average of the energy and multiplicity distributions are not so sensitive to the relatively infrequent outliers — that is, measurements that lie far from the average — as the spread or higher moments are.

The SMA detector requires very good gain calibrations to give a high accuracy for the spread of the energy distribution. These calibrations must necessarily be done on a large minimum bias sample of events. However, at the end of the $\sqrt{s_{NN}} = 200\,\text{GeV}$ run in 2000, very few minimum bias runs was collected at the time where the RHIC accelerator worked the best. That means that the gain calibrations for the larger part of the central events is not optimal, which has the consequence that the spread of the energy distribution is larger than necessary.

From the trouble discussed in Chapter 6 on simulations and Chapter 7 on the fits, it is clear that the result of the fluctuation analysis is very dependent on the precision of various conversion procedures needed in going from ADC counts to charged particle multiplicity via the summed deposited energy signal. In particular, the large spread in the energy deposited by a charged particle and the integrating nature of the SMA severely limits this detectors ability to measure fluctuations. The assumption that $\overline{E} = \bar{e}\overline{M_{\text{ch}}}$ seems quite reasonable at first sight, but turns out to be wrong.

For the method employed here, of fitting ω_E to a function of $\overline{E}$ with parameters ω_e, $\frac{\omega_n}{\bar{n}}$, and ω_m, it is important that the resolution of summed energy signal is good enough that the assumption of $\overline{E} = \bar{e}\overline{M_{\text{ch}}}$ can be validated — otherwise, the parameterisation of ω_E becomes invalid and meaningless. The strong (anti–)correlations seen in the fit parameters, suggests that the parameterisation is in fact not valid, and that the simple picture that leads to this parameterisation is not entirely correct. That is hardly surprising, as it is well–known that there are strong correlations and collective effects in relativistic heavy ion collisions.

Going forth, and applying the model–dependent correction to the ω_m extracted via the fits, a bare ω_m of 4.3 ± 0.3 is obtained. That value suggests that the particle production is far from trivial, in the sense of Poissonian statistics. In fact, it is closer to the KNO scaling value of 6.3, but not near high enough to suggest a transition to to chiral symmetric and deconfined matter.

What the Future has in Store

The ideal detector for fluctuation analysis like the one presented here, would be a detector with an occupancy of 5 % or less, and if that is not possible, that the contribution to the summed energy signal from $1, 2, \ldots$ particles can be positively identified. The former implies a detector with a high spatial segmentation, which unfortunately is a rather costly design. The latter is possible by having very sensitive detectors over a large energy domain, possibly with some redundancy to exclude decay particles and similar. This may be hard to accomplish in an environment of 100–700 charged particles per unit pseudorapidity.

However, the future does hold some promise for this kind of analysis. The ALICE detector at LHC, scheduled to record Pb+Pb collisions at $\sqrt{s_{NN}} = 4\,\mathrm{TeV}$ in 2008 is one such promise.

In ALICE, the Inner Tracking System, covering $|\eta| < 1.7$, is expected to have an occupancy of a few percent [67], making it ideal for fluctuation analysis. Also, in the Forward Multiplicity Detector (FMD) of ALICE, designed at the Niels Bohr Institute, the expected number of particles hitting an element will be lower than 1 [68], giving an occupancy lower than 63 %, assuming Poissonian statistics[1]. The FMD covers the union of $-5.1 < \eta < -1.7$ and $1.7 < \eta < 3.4$, so that together the ITS and FMD cover the range $-5.1 < \eta < 3.4$ with very high granularity.

Also, the tracking system of CMS, also at LHC is expected to have an occupancy from 1 % to 10 % in $|\eta| < 1.8$ [69] for the Pb+Pb running, making it ideal for measuring fluctuations in charged particle multiplicity, though in a more limited η range than ALICE.

Christian Holm Christensen
Copenhagen, February 2003

[1] See also Appendix B.5

Bibliography

[1] Particle Data Group Collaboration, D. E. Groom *et al.*, 'Review of particle physics,' *Eur. Phys. J.,* **C15** (2000) 1–878.

[2] G. S. Bali, K. Schilling, C. Schlichter, and A. Wachter, 'Confining Forces and String Formation from the Lattice,' `hep-lat/9410002`.

[3] M. E. Peskin and D. V. Schroeder, *Introduction to Quantum Field Theory.* Addison-Wesley, Reading, USA, 1997.

[4] B. Muller, 'Physics of the Quark-Gluon Plasma,' `nucl-th/9211010`.

[5] Z. Fodor and S. D. Katz, 'Lattice QCD Results at Finite T and μ,' `hep-lat/0204029`.

[6] T. Blum, L. Karkkainen, D. Toussaint, and S. Gottlieb, 'The Beta Function and Equation of State for QCD with Two Flavors of Quarks,' *Phys. Rev.,* **D51** (1995) 5153–5164, `hep-lat/9410014`.

[7] G. Boyd *et al.*, 'Equation of State for the SU(3) Gauge Theory,' *Phys. Rev. Lett.,* **75** (1995) 4169–4172, `hep-lat/9506025`.

[8] J. W. Harris and B. Muller, 'The Search for the Quark-Gluon Plasma,' *Ann. Rev. Nucl. Part. Sci.,* **46** (1996) 71–107, `hep-ph/9602235`.

[9] H. Satz, 'QCD and QGP: A summary,' `hep-ph/9706342`.

[10] J. J. Brehm and W. J. Mullin, *Introduction to the Structure of Matter.* John Wiley & Sons, Inc., 1989.

[11] X.-N. Wang and M. Gyulassy, 'HIJING: A Monte Carlo Model for Multiple Jet Production in p+p, p+A and A+A Collisions,' *Phys. Rev.,* **D44** (1991) 3501–3516.

[12] M. Gyulassy and X.-N. Wang, 'HIJING 1.0: A Monte Carlo Program for Parton and Particle Production in High-Energy Hadronic and Nuclear Collisions,' *Comput. Phys. Commun.,* **83** (1994) 307, `nucl-th/9502021`.

[13] BRAHMS Collaboration, I. G. Bearden *et al.*, 'Rapidity Dependence of Antiproton to Proton Ratios in Au+Au Collisions at $\sqrt{s_{NN}} = 130\,\mathrm{GeV}$,' *Phys. Rev. Lett.,* **87** (2001) 112305, `nucl-ex/0106011`.

[14] BRAHMS Collaboration, I. G. Bearden *et al.*, 'Rapidity Dependence of Charged Antiparticle-to-Particle Ratios in Au+Au Collisions at $\sqrt{s_{NN}} = 200$ GeV,' `nucl-ex/0207006`. Submitted to Phys. Rev. Lett.

[15] Z.-w. Lin, S. Pal, C. M. Ko, B.-A. Li, and B. Zhang, 'Multiphase Transport Model for Heavy Ion Collisions at RHIC,' *Nucl. Phys.,* **A698** (2002) 375–378, `nucl-th/0105044`.

[16] BRAHMS Collaboration, I. G. Bearden *et al.*, 'Pseudorapidity Distributions of Charged Particles from Au+Au Collisions at the Maximum RHIC Energy,' *Phys. Rev. Lett.,* **88** (2002) 202301, `nucl-ex/0112001`.

[17] J. Bondorf, T. Døssing, J. J. Gaardhøje, H. Heiselberg, A. Jackson, B. Lauritzen, I. Mishustin, and H. Schulz, *Topics in Nuclear Physics.* Niels Bohr Institute, University of Copenhagen, 1999.

[18] STAR Collaboration, R. Snellings, 'Single Particle Inclusive Spectra, HBT and Elliptic Flow: A Consistent Picture at RHIC?,' `hep-ph/0111437`.

[19] STAR Collaboration, H. Z. Huang, 'Anti-baryon to Baryon Ratios in Au+Au Collisions at $\sqrt{s_{NN}} = 130\,\mathrm{GeV}$,' *Nucl. Phys.,* **A698** (2002) 663–666.

[20] PHENIX Collaboration, H. Ohnishi, 'Particle Ratios in PHENIX at RHIC,' *Nucl. Phys.,* **A698** (2002) 659–662.

[21] PHOBOS Collaboration, B. B. Back *et al.*, 'Ratios of Charged Antiparticles to Particles Near Mid- Rapidity in Au+Au collisions at $\sqrt{s_{NN}} = 130\,\mathrm{GeV}$,' *Phys. Rev. Lett.,* **87** (2001) 102301, `hep-ex/0104032`.

[22] P. L. H. Christiansen, 'Pion Interferometry in Central 158GeV/Nucleon Pb+Pb Collisions at CERN SPS,' Master's thesis, Niels Bohr Institute, September, 1999.

[23] A. G. Hansen, 'Light Nuclei Production in Ultra Relativisitc Heavy Ion Collisions,'. PhD thesis, Niels Bohr Institute, Aug., 1999.

[24] H. Heiselberg and A. D. Jackson, 'Signatures of QCD Matter at RHIC,' `nucl-th/9809013`.

[25] NA50 Collaboration, M. C. Abreu *et al.*, 'Evidence for Deconfinement of Quarks and Gluons from the J/psi Suppression Pattern Measured in Pb+Pb Collisions at the CERN-SPS,' *Phys. Lett.,* **B477** (2000) 28–36.

[26] V. Koch, 'Aspects of Chiral Symmetry,' *Int. J. Mod. Phys.,* **E6** (1997) 203–250, `nucl-th/9706075`.

[27] M. Bleicher, J. Randrup, R. Snellings, and X. N. Wang, 'Enhanced Event-by-Event Fluctuations in Pion Multiplicity as a Signal of Disoriented Chiral Condensates at RHIC,' *Phys. Rev.,* **C62** (2000) 041901, `nucl-th/0006047`.

[28] H. S. Walter Greiner, Ludwig Neise, *Thermodynamics and Statistical Mechanics.* Springer-Verlag, New York, 1997.

[29] H. Heiselberg, G. Baym, B. Blaettel, L. L. Frankfurt, and M. Strikman, 'Color Transparency, Color Opacity, and Fluctuations in Nuclear Collisions,' *Phys. Rev. Lett.,* **67** (1991) 2946–2949.

[30] G. Baym and H. Heiselberg, 'Event-by-Event Fluctuations in Ultrarelativistic Heavy-Ion Collisions,' *Phys. Lett.,* **B469** (1999) 7–11, `nucl-th/9905022`.

[31] M. Asakawa, U. W. Heinz, and B. Muller, 'Fluctuation Probes of Quark Deconfinement,' *Phys. Rev. Lett.,* **85** (2000) 2072–2075, `hep-ph/0003169`.

[32] G. Baym, B. Blattel, L. L. Frankfurt, H. Heiselberg, and M. Strikman, 'Correlations and Fluctuations in High-Energy Nuclear Collisions,' *Phys. Rev.,* **C52** (1995) 1604–1617, `nucl-th/9502038`.

[33] F. W. Bopp and J. Ranft, 'Charged Particle Fluctuation as Signal of the Dynamics in Heavy Ion Processes,' *Eur. Phys. J.,* **C22** (2001) 171–177, `hep-ph/0105192`.

[34] P. Carruthers and C. C. Shih, 'Correlations and Fluctuations in Hadronic Multiplicity Distributions: The Meaning of KNO Scaling,' *Phys. Lett.,* **B127** (1983) 242.

[35] M. Gazdzicki, A. Leonidov, and G. Roland, 'On Event-by-Event Fluctuations in Nuclear Collisions,' *Eur. Phys. J.,* **C6** (1999) 365–369, `hep-ph/9711422`.

[36] H. Heiselberg, 'Event-by-Event Physics in Relativistic Heavy-Ion Collisions,' *Phys. Rept.,* **351** (2001) 161–194, `nucl-th/0003046`.

[37] H. Heiselberg and A. D. Jackson, 'Anomalous Multiplicity Fluctuations from Phase Transitions in Heavy Ion Collisions,' *Phys. Rev.,* **C63** (2001) 064904, `nucl-th/0006021`.

[38] R. C. Hwa and Q.-h. Zhang, 'Fluctuation of Voids in Hadronization at Phase Transition,' *Phys. Rev.,* **C62** (2000) 054902, `nucl-th/0003032`.

[39] S. Jeon and V. Koch, 'Fluctuations of Particle Ratios and the Abundance of Hadronic Resonances,' *Phys. Rev. Lett.,* **83** (1999) 5435–5438, `nucl-th/9906074`.

[40] S. Jeon and V. Koch, 'Charged Particle Ratio Fluctuation as a Signal for QGP,' *Phys. Rev. Lett.,* **85** (2000) 2076–2079, `hep-ph/0003168`.

[41] B. Mohanty, D. P. Mahapatra, and T. K. Nayak, 'A Fluctuation Probe of Disoriented Chiral Condensates,' `nucl-ex/0201010`.

[42] S. Mrowczynski, 'Measuring Charge Fluctuations in High-Energy Nuclear Collisions,' `nucl-th/0112007`.

[43] M. Stephanov, 'QCD Critical Point and Event-by-Event Fluctuations in Heavy Ion Collisions,' *Nucl. Phys.,* **A661** (1999) 403–406, `hep-ph/9907312`.

[44] M. Stephanov, K. Rajagopal, and E. V. Shuryak, 'Event-by-Event Fluctuations in Heavy Ion Collisions and the QCD Critical Point,' *Phys. Rev.,* **D60** (1999) 114028, `hep-ph/9903292`.

[45] E. V. Shuryak, 'Event-per-Event Analysis of Heavy Ion Collisions and Thermodynamical Fluctuations,' *Phys. Lett.,* **B423** (1998) 9–14, `hep-ph/9704456`.

[46] S. A. Voloshin, V. Koch, and H. G. Ritter, 'Event-by-Event Fluctuations in Collective Quantities,' `nucl-th/9903060`.

[47] WA98 Collaboration, M. M. Aggarwal *et al.*, 'Event-by-Event Fluctuations in Particle Multiplicities and Transverse Energy Produced in 158AGeV Pb+Pb Collisions,' `nucl-ex/0108029`.

[48] WA98 Collaboration, T. K. Nayak *et al.*, 'Multiplicity Distributions and Charged-Neutral Fluctuations,' *Pramana,* **57** (2001) 285–300, `nucl-ex/0103007`.

[49] WA98 Collaboration, T. K. Nayak *et al.*, 'Multiplicity Distributions and Charged Neutral Fluctuations,' `nucl-ex/0108026`.

[50] E. Jakobsen, 'Event–by–Event Fluctuations in Charged Particle Production in Au+Au Collisions at $\sqrt{s_{NN}} = 130\,\text{GeV}$,' Master's thesis, Niels Bohr Institute, December, 2001.

[51] P. R. Bevington and D. K. Robinson, *Data Reduction and Error Analysis for the Physical Sciences.* McGraw–Hill, Inc., 2 ed., 1992.

[52] BRAHMS Collaboration, I. G. Bearden *et al.*, 'Charged Particle Densities from Au+Au Collisions at $\sqrt{s_{NN}} = 130\,\text{GeV}$,' *Phys. Lett.,* **B523** (2001) 227–233, `nucl-ex/0108016`.

[53] NA49 Collaboration, H. Appelshauser *et al.*, 'Event-by-Event Fluctuations of Average Transverse Momentum in Central Pb+Pb Collisions at 158GeV per Nucleon,' *Phys. Lett.,* **B459** (1999) 679–686, `hep-ex/9904014`.

[54] NA49 Collaboration, J. G. Reid, 'Event-by-Event Physics in NA49,' *Nucl. Phys.,* **A661** (1999) 407–410.

[55] PHENIX Collaboration, K. Adcox *et al.*, 'Event-by-Event Fluctuations in Mean $p_\perp$ and Mean $e_\perp$ in $\sqrt{s_{NN}} = 130\,\text{GeV}$ Au+Au Collisions,' *Phys. Rev.,* **C66** (2002) 024901, `nucl-ex/0203015`.

[56] STAR Collaboration, J. G. Reid, 'STAR Event–by–Event Fluctuations,' *Nucl. Phys.,* **A698** (2002) 611–614.

[57] PHENIX Collaboration, K. Adcox, 'Flow Measurements via Two-Particle Azimuthal Correlations in Au+Au Collisions at $\sqrt{s_{NN}} = 130\,\text{GeV}$,' *Phys. Rev. Lett.,* **89** (2002) 212301, `nucl-ex/0204005`.

[58] PHENIX Collaboration, A. Enokizono, 'Two-Particle Correlations Measured by PHENIX in Au+Au collisions at $\sqrt{s_{NN}} = 200\,\text{GeV}$,' `nucl-ex/0209026`. Talk given at 16th International Conference on Ultrarelativistic Nucleus-Nucelus Collisions, Quark Matter 2002 (QM 2002), Nantes, France, 18-24 Jul 2002.

[59] BRAHMS Collaboration, I. G. Bearden *et al.*, 'The BRAHMS Experiment at RHIC,' *Nucl. Instrum. Meth.,* **???** (2002) ???

[60] H. Ito, 'Charged–Particle Production in Au+Au Collisions at $\sqrt{s_{NN}} = 130\,\text{GeV}$ and $\sqrt{s_{NN}} = 200\,\text{GeV}$,'. PhD thesis, Kansas Univeristy, 2002. Limited access via web–page.

[61] OMG, *OMG Unified Modeling Language Specification* specification, Object Mangament Group, September, 2001.

[62] C. H. Christensen and F. Videbæk, *The Hitchickers Guide to BRAT.* BRAHMS Collaboration, 2002. `http://pii3.brahms.bnl.gov/~brahmlib/brat/guide`.

[63] R. Brun, F. Carminatti, and F. Rademarkers, *GEANT 3.21.* CERN, Geneva, Switcherland, October, 1994.

[64] R. K. Bock and A. Vasilescu, *The Particle Detector Briefbook.* Springer, Berlin, Germany, 1998.

[65] D. E. Groom, N. V. Mokhov, and S. I. Striganov, 'Muon Stopping Power and Range Tables 10 MeV to 100 TeV,' *Atom. Data Nucl. Data Tabl.,* **78** (2001) 183–356.

[66] BRAHMS Collaboration, I. G. Bearden, 'Anti-Proton to Proton Ratio in $\sqrt{s_{NN}} = 130\,\text{GeV}$ Au+Au Collisions,' *Nucl. Phys.,* **A698** (2002) 667–670.

[67] ALICE Collaboration, 'ALICE Technical Design Report of the Inner Tracking System (ITS),'. CERN-LHCC-99-12.

[68] J. J. Gaardhøje and B. S. Nielsen, *A Silicon Forward Multiplicity Detector (FMD) for ALICE* In preperation, November, 2002.

[69] CMS Collaboration, *Technical Proposal* CERN/LHCC 94–38, CERN, Geneva, December, 1994.

[70] R. Brun and F. Rademakers, 'ROOT: An object oriented data analysis framework,' *Nucl. Instrum. Meth.,* **A389** (1997) 81–86.

Appendix A

Variables

A.1 Physical Variables

For a particle with three–momentum $\mathbf{p} = (p_x, p_y, pz)$ and mass m we get

$$
\begin{aligned}
p &\equiv \sqrt{p_x^2 + p_y^2 + p_z^2} \\
p_\perp &\equiv \sqrt{p_x^2 + p_y^2} \\
p_\parallel &\equiv p_z \\
m_\perp &\equiv \sqrt{m^2 + p_\perp^2} \\
E &= \sqrt{m^2 + p^2}
\end{aligned}
$$

We define the rapidity y as

$$y \equiv \log \frac{E + p_\parallel}{E - p_\parallel} \quad . \tag{A.1}$$

y has the nice property that it is relativistically additive, so that seen a particle seen moving with y in the frame S, is seen in the frame S' moving with y_β relative to S is simply given by

$$
\begin{aligned}
y' &= \frac{1}{2} \log \frac{p' + p'_\parallel}{p' - p'_\parallel} \\
&= \frac{1}{2} \log \frac{\gamma(1-\beta)(p' + p'_\parallel)}{\gamma(1+\beta)(p' - p'_\parallel)} \\
&= \frac{1}{2} \log \frac{p + p_\parallel}{p - p_\parallel} + \frac{1}{2} \log \frac{1+\beta}{1-\beta} \\
&= y - y_\beta
\end{aligned}
$$

When the energy of a particle is not known it is convenient to define the pseudorapidity η as:

$$\eta \equiv -\log \left(\tan \frac{\vartheta}{2} \right) \quad , \tag{A.2}$$

where $\vartheta \equiv \tan^{-1}(p_\perp / p_\parallel)$.

One often characterises the available energy in a collision by the centre–of–mass $\sqrt{s}$ energy of the system. However, for nucleus–nucleus collision a more measure convenient measure is the centre–of-mass energy per colliding nucleon pair $\sqrt{s_{NN}}$. Sometimes one also sees the notation $\sqrt{s} = x\text{AGeV}$ which is the same as $\sqrt{s_{NN}} = x\,\text{GeV}$.

A.2 Statistical Variables

Since the analysis carried out in this work, is largely statistical, both in the nature of the BRAHMS experiment, but also in kind, a brief discussion of some statistical concepts seem in order.

Given N successive measurement of the variable x, we define the *sample mean* or average $\bar{x}$ as:

$$\bar{x} \equiv \frac{1}{N}\sum_{i=1}^{N} x_i \quad . \tag{A.3}$$

To characterise the dispersion of the data away from the mean, we define the *sample variance* s^2 as

$$\begin{aligned} s_x^2 &\equiv \frac{1}{N-1}\sum_{i=1}^{N}(x_i-\bar{x})^2 = \frac{N}{(N-1)N}\sum_{i=1}^{N}\left(x_i^2+\bar{x}^2-2\bar{x}x_i\right) \\ &= \frac{N}{N-1}\left(\overline{x^2}+\bar{x}^2-2\bar{x}^2\right) = \frac{N}{N-1}\left(\overline{x^2}-\bar{x}^2\right) \quad , \end{aligned} \tag{A.4}$$

which in the limit of large N becomes

$$s_x^2 \underset{N\gg 1}{\approx} \overline{x^2} - \bar{x}^2 \quad .$$

The $N-1$ in the numerator in equation (A.4) is needed to make s^2 an *unbiased* estimator of the *parent variance.*

For a given distribution $P(x)$, where the probability of measuring fraction dN of $x' \in [x, x+dx]$ is given by

$$dN = P(x)dx \quad ,$$

and the probabilities are normalised

$$\int_{-\infty}^{\infty} dx\, P(x) = 1 \quad ,$$

we can define the the *parent mean* $\langle x\rangle$ as

$$\langle x\rangle \equiv \int_{-\infty}^{\infty} dx\, xP(x) \tag{A.5}$$

One sees that

$$\langle x\rangle \equiv \lim_{N\to\infty} \bar{x}$$

The dispersion is given by

$$\sigma_x^2 \equiv \int_{-\infty}^{\infty} dx\,(x-\langle x\rangle)^2 P(x) \tag{A.6}$$

and again,

$$\sigma_x^2 \equiv \lim_{N\to\infty} s_x^2$$

For M stochastic variables $x_1, x_2, \ldots, x_M$, the correlation of the i^{th} and j^{th} variables are characterised by the *covariance* matrix element C_{ij}:

$$C_{ij} = \frac{1}{N}\sum_{k=1}^{N}\left(x_{ik}-\overline{x_k}\right)\left(x_{jk}-\overline{x_j}\right) = \overline{x_i x_j} - \overline{x_i}\,\overline{x_j} \tag{A.7}$$

The covariance matrix is positive semi–definite.

If two stochastic variables x_i, x_j are *uncorrelated* the element of the covariance matrix C_{ij} becomes identical zero, and

$$\overline{x_i x_j} = \overline{x_i}\,\overline{x_j}$$

However, if x_i and x_j are *correlated*, meaning that a higher value of x_i implies a higher value of x_j, and vice versa, then the element $C_{ij} > 0$. Equivalently, if x_i and x_j are *anti correlated*, meaning a higher value of x_i implies a lower value of x_j the element $C_{ij} < 0$. If x_i and x_j are (anti)correlated, then

$$\overline{x_i x_j} = \overline{x_i}\,\overline{x_j} + C_{ij} \neq \bar{x}\bar{y}$$

Appendix B

Details of the Analysis

B.1 Software Overview

For the analysis presented in Chapter 5, the *BR*ahms *A*nalysis *T*oolkit[1] (BRAT) was used, with some additional user modules and data structures.

BRAT is a toolkit developed by the BRAHMS collaboration for reduction, analysis, etc. of experimental and simulated data. It is based on the *R*oot's *O*bject–*O*riented *T*echnologies[2] (ROOT) [70] framework from CERN. The author of this text have had the pleasure of working with the ROOT main developers René Brun and Fons Rademarkers during his stay at CERN as a summer student in the year 2000, and continues to contribute to ROOT.

BRAT is mainly composed of *modules* and *data structures*, where each module is responsible for the creation and manipulation of a specific (set of) data structures. These modules can be connected in a module pipeline via a simple configuration file, to form an reconstruction, analysis, etc. job. Individual users can, and are encouraged to create their specialised modules to insert into the module pipeline as they see fit. Users can also define specialised data structures for their modules to read/write to storage disks.

Data structures written to disk are often catalogued and summarised into some sort of *D*ata *S*ummary *T*ape[3] (DST), which one then analysis in the interactive environment of ROOT, making histograms and plots. Most of the plots in the current text is made using ROOT, though some, are obtained from third–party sources (and duly marked so).

B.2 Analysis Steps

The analysis at hand is done in a two step process

1. First, the raw data as recorded by the DAQ, is processed to give

    - Interaction point location, using the BB.
    - Energy and multiplicity signals from the SMA.
    - Energy and multiplicity signals from the TMA.
    - Centrality determination from the energy signal in the TMA.

[1] Please refer to `http://pii3.brahms.bnl.gov/~brahmlib` for extensive information on BRAT.

[2] Please refer to `http://root.cern.ch` for extensive information on ROOT.

[3] These are not really magnetic tapes, but rather normal files on some storage device. The term has historical meaning, from back when magnetic tapes was extensively used.

These data structures are written to storage.

Events with irrelevant triggers, such as synchronisation and pedestal triggers are discarded. Events with an interaction point outside of the defined cuts are discarded.

2. The second step uses the data structures of the previous step to give

   - Fluctuations in the energy signal of the SMA, as a function of η, φ and/or centrality, in various bin sizes.
   - Fluctuations in the multiplicity signal of the SMA, as a function of η, φ and/or centrality.
   - Fluctuations in the multiplicity signal of the TMA, as a function of η, φ and/or centrality.

   These data structures are written to storage. These data structures are what is presented in this work. They can be directly manipulated, plotted and histogramed in an interactive ROOT session.

Below, the 'BRAHMS CVS repository' refers to the software archive at

`/afs/rhic/brahms/BRAHMS_CVS`

accessible via CVS from any machine that is running AFS, provided the user has the needed privileges. 'The authors area' refers to the sub archive of the above archive located in the subdirectory `brahms_app/cholm_app`; Please refer to the file `README` in that directory. Please also refer to [62] for more information on CVS use in BRAHMS.

The first step above is performed using standard BRAT modules and data structures. The configuration file for this step is called `GlbRdoConfig.C` and can be obtained from the authors area in the BRAHMS CVS repository in the subdirectory `jobs/global`. The data is analysed on a GNU/Linux farm at BNL, called RCAS, to speed up the processing; however, the only requirement in terms of environment is a standard installation of BRAT and ROOT, plus access to the raw data and the run catalogue served from `mysql://pii3.brahms.bnl.gov/RUNDB`.

The second step involves the user defined module `FluctModule` and data structure `Fluct`; the configuration file for this step is `FluctConfig.C`. The above is available from the authors are in the BRAHMS CVS repository in the subdirectory `jobs/fluct`. Again, the data is processed on a GNU/Linux farm at BNL, called RCAS, for speed, but the only requirements in terms of environment is the installation of ROOT, BRAT, and the above mentioned user modules and data structures.

Approximately 80 runs have been analysed, with a total of more than 10 million useful events. In Table B.1 the run numbers are listed. The runs have been chosen on the merits of the number of central events and available calibrations. The software necessary to set up the analysis of these runs on the GNU/Linux farms is available from the authors area in the BRAHMS CVS repository in the subdirectory `runs`.

Questions, comments, etc. on the software and other details on this can be sent to `cholm@nbi.dk` (see also the cover page).

B.3 Detailed Plots from the Simulation Analysis

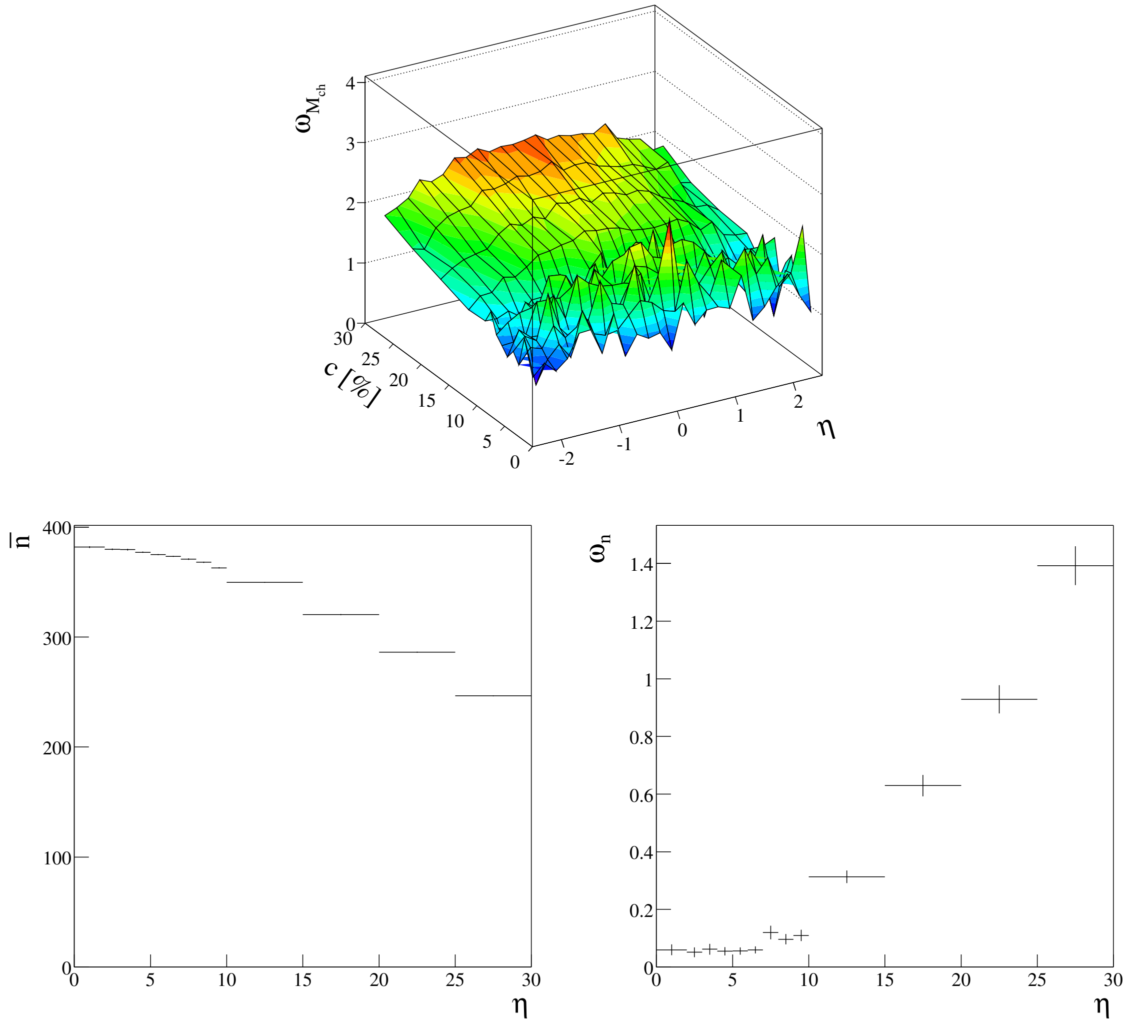

Figure B.1: $\overline{M_{\text{ch}}}$, $\omega_{M_{\text{ch}}}$, $\bar{n}$, and ω_n from vanilla HIJING data.

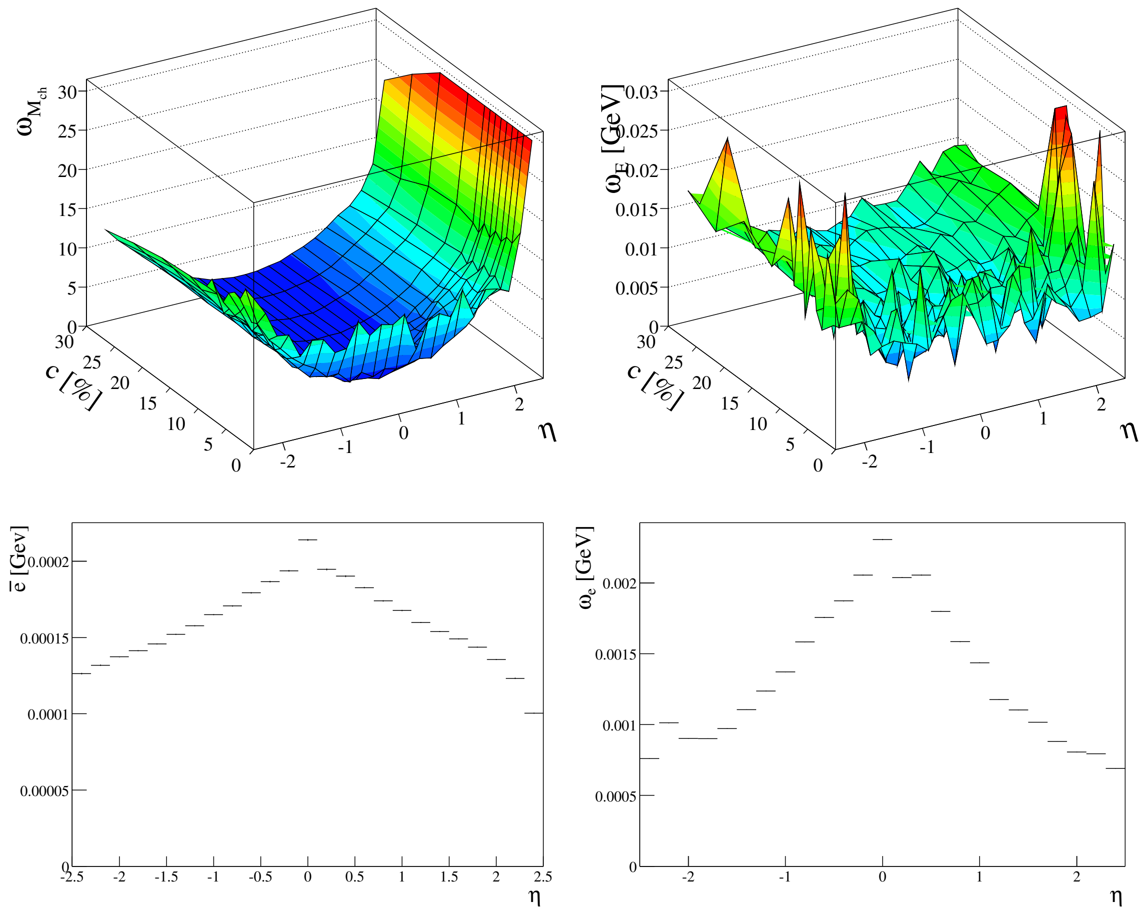

Figure B.2: $\omega_{M_{\mathrm{ch}}}$, and ω_E within the acceptance of the SMA.

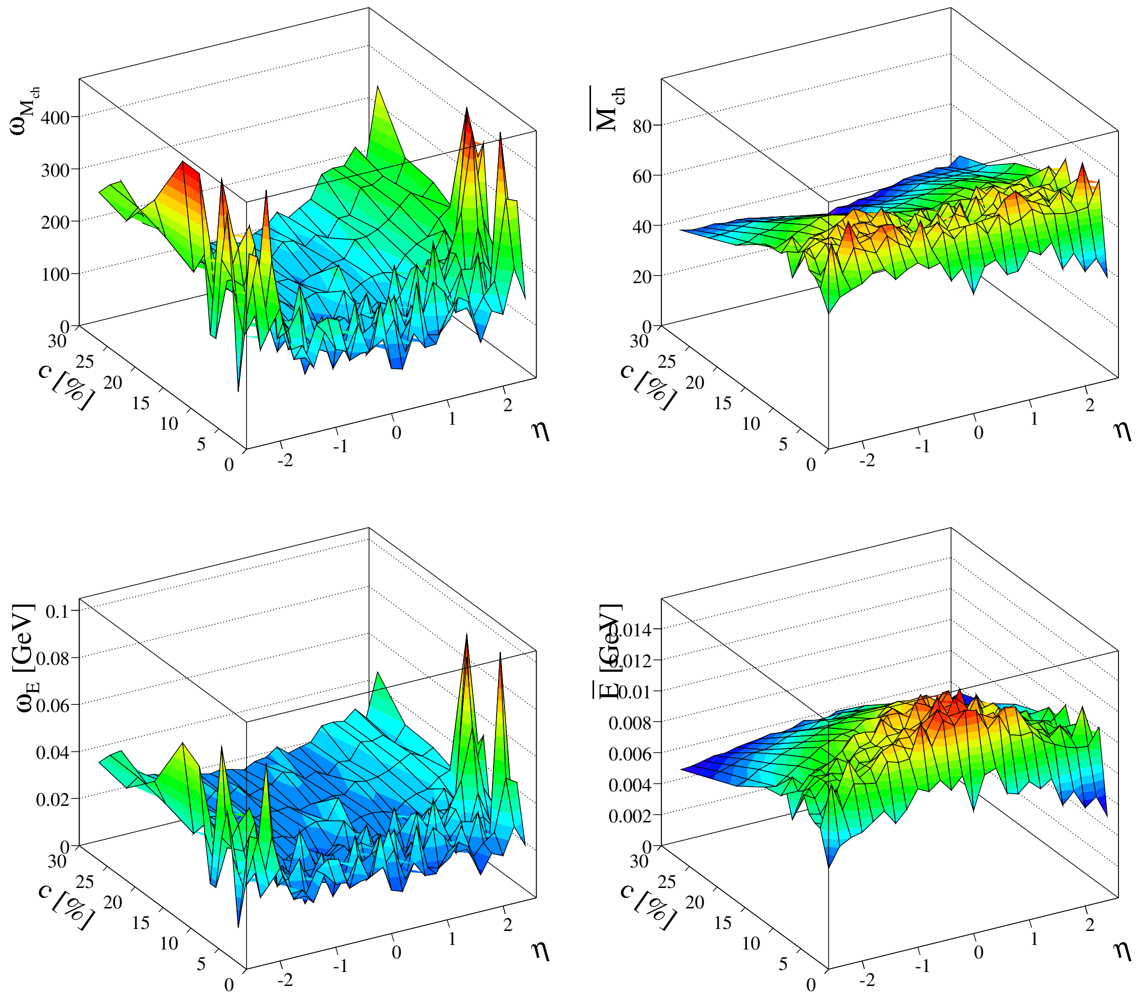

Figure B.3: Reconstructed $\overline{M_{\mathrm{ch}}}$, $\omega_{M_{\mathrm{ch}}}$, $\overline{E}$, and ω_E from BRAG simulation.

B.4 $\overline{M_{\mathrm{ch}}}$ as a Function of $\overline{E}$

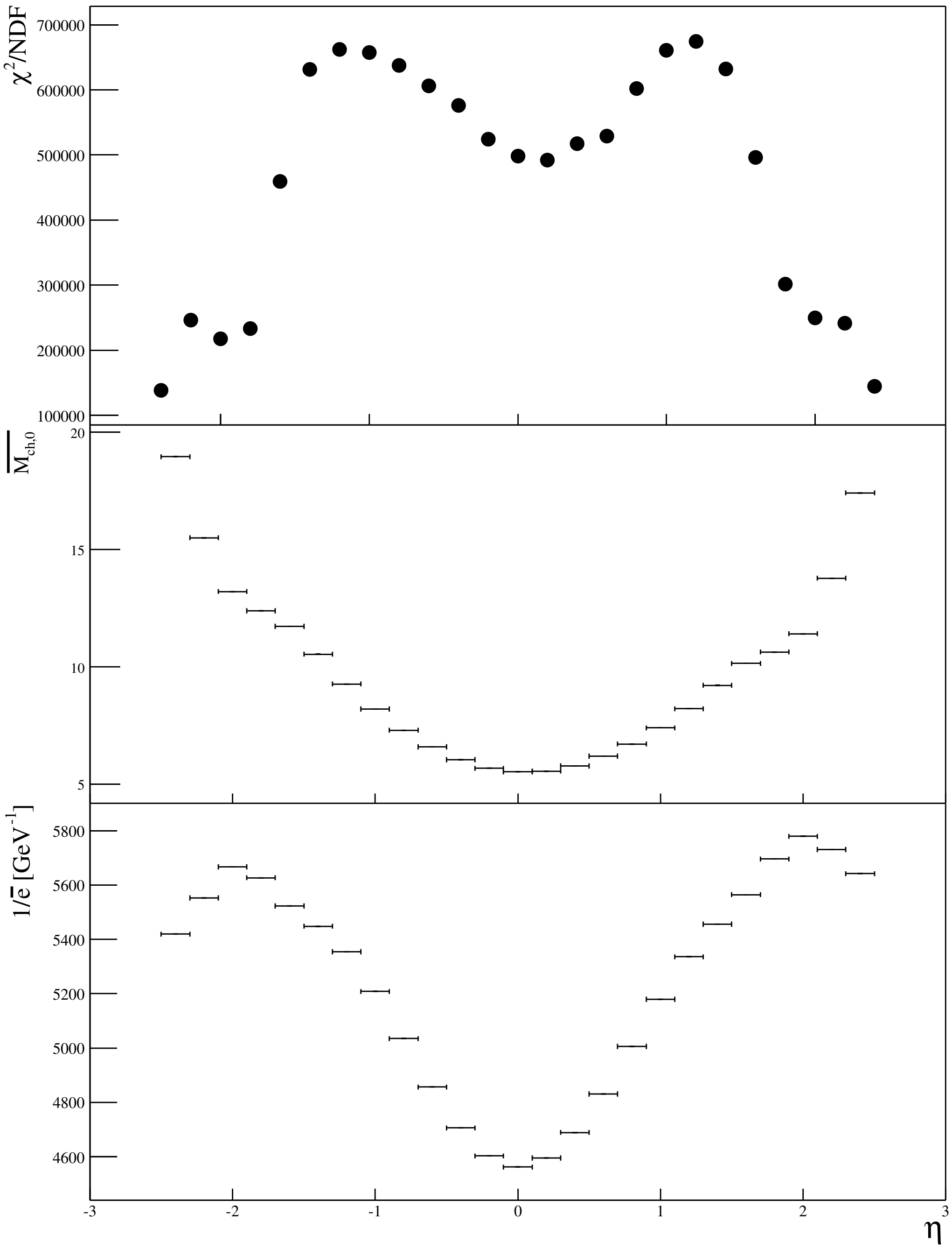

Figure B.4: Fit parameters of $\overline{M_{\mathrm{ch}}}$ fitted to a linear function in $\overline{E}$ for each η bin.

B.5 Occupancy

The occupancy for a detector element, is the probability that at least one particle hit the element in an event [64]. So if one assumes that the number of particles that impinges on a detector element is Poissonian distributed

$$P_\mu(x) = \frac{\mu^x}{x!} e^{-\mu} \quad ,$$

where μ is the mean, or expected number of particles, then the occupancy O is simply

$$O = P(x \geq 1) = 1 - P(0) \quad .$$

For a detector with $\mu = 1$, this evaluates to $O = 63.2\,\%$, while for $\mu = 3$, O becomes $95\,\%$. Figure B.5 show the occupancy O as a function of the expected number of particles μ, assuming Poissonian statistics.

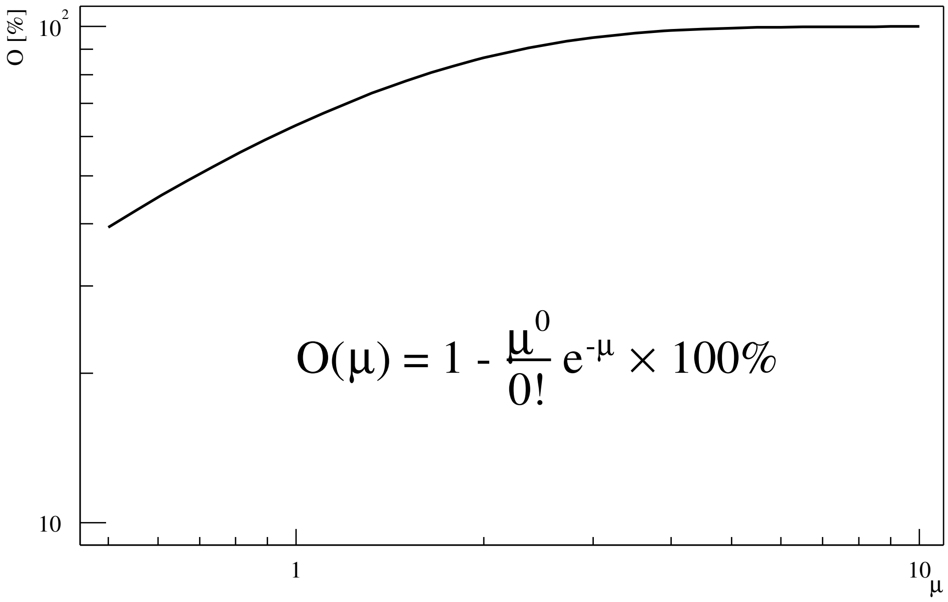

Figure B.5: Occupancy as a function of expected number of particles impinging on a detector element, assuming Poissonian statistics.

B.6 Miscellaneous Figures and Tables

5678	5679	5681	5682	5684	5685	5701	5702	5703	5711
5737	5749	5750	5761	5765	5772	5773	5775	5790	5791
5792	5797	5798	5803	5804	5805	5806	5811	5812	5813
5822	5823	5824	5826	5827	5828	5833	5834	5839	5840
5841	5846	5851	5853	5860	5862	5863	5864	5865	5866
5867	5868	5873	5880	5881	5882	5883	5884	5896	5901
5903	5904	5908	5914	5915	5916	5924	5925	5931	5933
5939	5946	5947	5952	5953	5956	5957	5963	5965	5971
5972									

Table B.1: Run numbers used in the analysis

Ring	0	1	2	3	4	5	6	7	8	9	10
$\bar{\eta}$	0.23	0.38	0.53	0.66	0.79	0.91	1.02	1.28	1.36	1.44	1.51
$\Delta\eta$	0.31	0.30	0.28	0.26	0.24	0.22	0.21	0.17	0.16	0.15	0.14
Ring	11	12	13	14	15	16	17	18	19	20	
$\bar{\eta}$	1.58	1.64	1.70	1.85	1.90	1.95	1.99	2.03	2.07	2.11	
$\Delta\eta$	0.13	0.12	0.11	0.10	0.09	0.09	0.09	0.08	0.08	0.08	

Table B.2: Acceptance of the SMA strips when $v_z \approx 0$

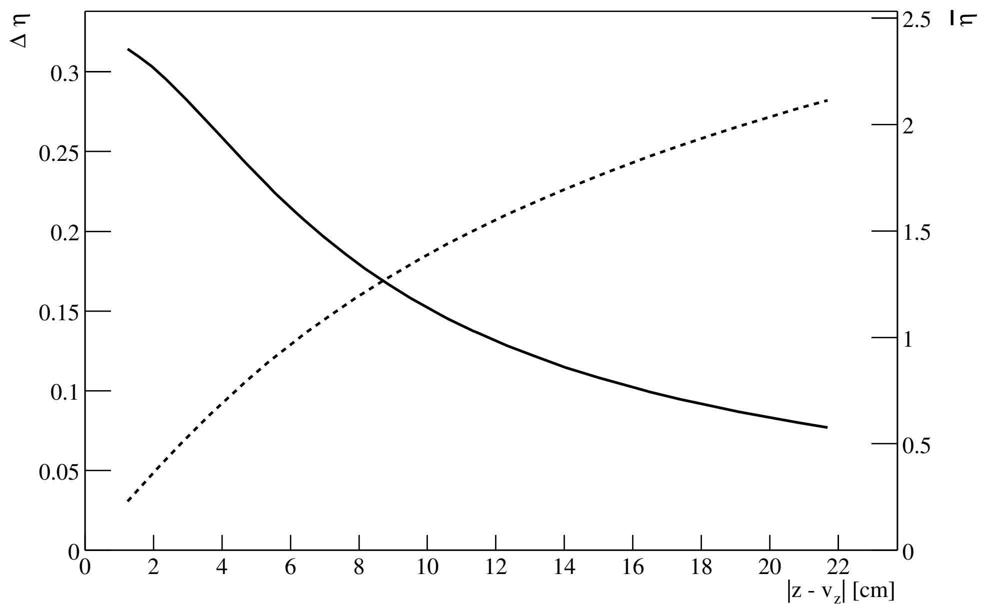

Figure B.6: $\Delta\eta$ (full line) and $\bar{\eta}$ (dashed line) as a function of the distance along the beam line to the interaction point.

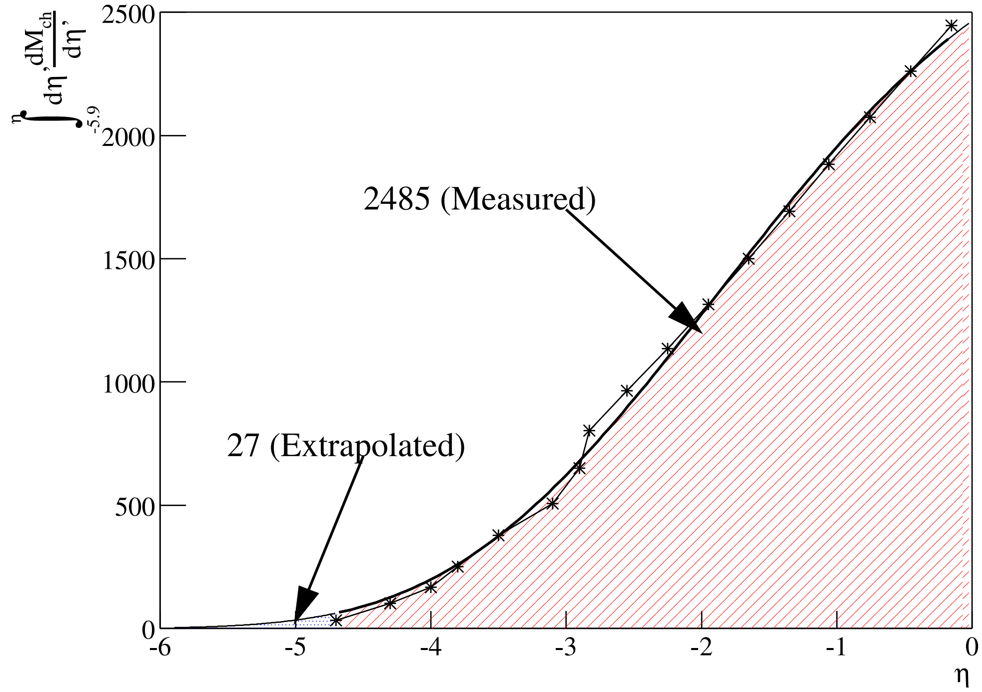

Figure B.7: Integral of Figure 5.6 from η = -4.7 to 0 for the 5 % most central events.

Appendix C

Derivations and the like

C.1 The error on ω

Assuming that $\omega = \omega(\mu_x, \sigma_x^2)$ we find:

$$
\begin{aligned}
\sigma_\omega^2 &= \left(\frac{\partial\omega}{\partial\mu_x}\right)^2 \sigma_{\mu_x}^2 + \left(\frac{\partial\omega}{\partial\sigma_x}\right)^2 \sigma_{\sigma_x^2}^2 \\
&= \left(\frac{\partial}{\partial\mu_x}\frac{\sigma_x^2}{\mu_x}\right)^2 \sigma_{\mu_x}^2 + \left(\frac{\partial}{\partial\sigma_x}\frac{\sigma_x^2}{\mu_x}\right)^2 \sigma_{\sigma_x^2}^2 \\
&= \left(-\frac{\sigma_x^2}{\mu_x^2}\right)^2 \sigma_{\mu_x}^2 + \left(\frac{1}{\mu_x}\right)^2 \sigma_{\sigma_x^2}^2
\end{aligned}
$$

From Bevington we get, assuming that $\sigma_{x_i} = \sigma_x$,

$$\sigma_{\mu_x}^2 = \frac{\sigma_x^2}{N}$$

where N is the sample size, and further,

$$
\begin{aligned}
\sigma_{\sigma_x^2}^2 &= \sigma_x^2 \sum_{i=1}^{N} \left(\frac{\partial\sigma_x^2}{\partial x_i}\right)^2 \\
&= \sigma_x^2 \sum_{i=1}^{N} \left(\frac{1}{N-1}\frac{\partial}{\partial x_i}\sum_{j=1}^{N}(x_j - \mu_x)^2\right)^2 \\
&= \sigma_x^2 \sum_{i=1}^{N} \left(\frac{2}{N-1}(x_i - \mu_x)\right)^2 \\
&= \frac{4\sigma_x^4}{N-1}
\end{aligned}
$$

Inserting that then gives

$$
\begin{aligned}
\sigma_\omega^2 &= \frac{\sigma_x^4}{\mu_x^4}\frac{\sigma_x^2}{N} + \frac{1}{\mu_x^2}\frac{4\sigma_x^4}{N-1} \\
&= \frac{\omega^3}{N\mu_x} + \frac{4\omega^2}{N-1}
\end{aligned}
$$

Assume N is large so that $N - 1 \approx N$, then

$$\sigma_\omega^2 = \frac{\omega^2}{N}\left(\frac{\omega}{\mu_x} + 4\right) \tag{5.10}$$

Finally, if $\omega \approx \mathcal{O}(1)$ and $\mu_x \approx \mathcal{O}(3)$, then we can ignore the ratio in the parenthesis, and we can write

$$\sigma_\omega^2 = \frac{4\omega^2}{N}$$

C.2 Recursive Calculation of Sample Mean and Covariance

Theorem 1 *For all $n > 1$, the sample mean $\bar{x} = \frac{1}{n}\sum_{i=1}^{n} x_i$ after n inputs of the variable x, is given by*

$$\bar{x}^{(n)} = \begin{cases} x_1 & n = 1 \\ \frac{n-1}{n}\bar{x}^{(n-1)} + \frac{1}{n}x_n & n > 0 \end{cases} \tag{C.1}$$

Proof of Theorem 1 Follows by induction:

$n = 1$: trivial.

$n = 2$:

$$\frac{2-1}{2}\bar{x}^{(1)} + \frac{1}{2}x_2 = \frac{1}{2}(x_1 + x_2)$$

Assume that (C.1) holds for $n-1$, then for n

$$\begin{aligned} \frac{n-1}{n}\bar{x}^{(n-1)} + \frac{1}{n}x_n &= \frac{n-1}{n}\frac{1}{n-1}\sum_{i=1}^{n-1} x_i + \frac{1}{n}x_n \\ &= \frac{1}{n}\left(\sum_{i=1}^{n-1} x_i + x_n\right) \\ &= \frac{1}{n}\sum_{i=1}^{n} x_i \end{aligned}$$

□

Theorem 2 *For all $n > 0$ the sample covariance $C_{ij} = \frac{1}{n}\sum_{k=1}^{n}(x_{ik} - \bar{x}_i)(x_{jk} - \bar{x}_j)$ after n inputs of $\mathbf{x}_k = (x_{1k}, \ldots, x_{mk})$, is given by*

$$C_{ij}^{(n)} = \begin{cases} 0 & n = 1 \\ \frac{n-1}{n}C_{ij}^{(n-1)} + \frac{1}{n-1}\left(x_{in} - \bar{x}_i^{(n)}\right)\left(x_{jn} - \bar{x}_j^{(n)}\right) & n > 1 \end{cases} \tag{C.2}$$

Lemma 1

$$C_{ij} = \frac{1}{n}\sum_{k=1}^{n} x_{ik}x_{jk} - \frac{1}{n^2}\sum_{k=1}^{n} x_{ik}\sum_{k=1}^{n} x_{jk}$$

Proof

$$\begin{aligned} C_{ij} &= \frac{1}{n}\sum_{k=0}^{n}(x_{ik} - \bar{x}_i)(x_{jk} - \bar{x}_j) \\ &= \frac{1}{n}\sum_{k=0}^{n}(x_{ik}x_{jk} + \bar{x}_i\bar{x}_j - x_{ik}\bar{x}_j - x_{jk}\bar{x}_i) \end{aligned}$$

Using $\sum_{k=1}^{n} \bar{x}_i = n\bar{x}_i$,

$$
\begin{aligned}
&= \frac{1}{n}\sum_{k=0}^{n} x_{ik}x_{jk} + \frac{n}{n}\bar{x}_i\bar{x}_j - \bar{x}_i\frac{1}{n}\sum_{k=0}^{n} x_{jk} - \bar{x}_j\frac{1}{n}\sum_{k=0}^{n} x_{ik} \\
&= \frac{1}{n}\sum_{k=0}^{n} x_{ik}x_{jk} + \bar{x}_i\bar{x}_j - \bar{x}_i\bar{x}_j - \bar{x}_i\bar{x}_j \\
&= \frac{1}{n}\sum_{k=0}^{n} x_{ik}x_{jk} - \bar{x}_i\bar{x}_j \\
&= \frac{1}{n}\sum_{k=1}^{n} x_{ik}x_{jk} - \frac{1}{n^2}\sum_{k=1}^{n} x_{ik}\sum_{k=1}^{n} x_{jk}
\end{aligned}
$$

□

Proof of Theorem 2 Consider the two variables (x, y). The proof generalises to arbitrary m, and follows by induction:

$n = 1$: trivial.

$n = 2$: equation (C.2) becomes

$$
\begin{aligned}
&\frac{2-1}{2}C_{xy}^{(1)} + \frac{1}{2-1}(x_2 - \bar{x}^{(2)})(y_2 - \bar{y}^{(2)}) \\
&= 0 + (x_2 - \bar{x}^{(2)})(y_2 - \bar{y}^{(2)}) \\
&= x_2y_2 + \bar{x}^{(2)}\bar{y}^{(2)} - x_2\bar{y}^{(2)} - y_2\bar{x}^{(2)} \\
&= x_2y_2 + \frac{1}{2}(x_1 + x_2)\frac{1}{2}(y_1 + y_2) - x_2\frac{1}{2}(y_1 + y_2) - y_2\frac{1}{2}(x_1 + x_2) \\
&= x_2y_2 + \frac{1}{4}(x_1y_1 + x_2y_2 + x_1y_2 + x_2y_1) - \frac{1}{2}(x_2y_1 + x_2y_2) - \frac{1}{2}(x_1y_2 + x_2y_2) \\
&= \left(1 + \frac{1}{4} - \frac{1}{2} - \frac{1}{2}\right)x_2y_2 + \frac{1}{4}x_1y_1 + \left(\frac{1}{4} - \frac{1}{2}\right)(x_1y_2 + x_2y_1) \\
&= \frac{1}{4}(x_1y_1 + x_2y_2) - \frac{1}{4}(x_1y_2 + x_2y_1)
\end{aligned}
$$

On the other hand, using Lemma 1, we get

$$
\begin{aligned}
\frac{1}{2}\sum_{k=1}^{2} x_ky_k - \frac{1}{4}\sum_{k=1}^{2} x_k\sum_{k=1}^{2} y_k &= \frac{1}{2}(x_1y_1 + x_2y_2) - \frac{1}{4}(x_1 + x_2)(y_1 + y_2) \\
&= \frac{1}{2}(x_1y_1 + x_2y_2) - \frac{1}{4}(x_1y_1 + x_2y_2 + x_1y_2 + x_2y_1) \\
&= \frac{1}{4}(x_1y_1 + x_2y_2) - \frac{1}{4}(x_1y_2 + x_2y_1)
\end{aligned}
$$

Assume (C.2) holds for $n-1$, then for n

$$
\begin{aligned}
C_{xy}^{(n)} &= \frac{n-1}{n}C_{xy}^{(n-1)} + \frac{1}{n-1}\left(x_n - \bar{x}^{(n)}\right)\left(y_n - \bar{y}^{(n)}\right) \\
&= \frac{n-1}{n}\frac{1}{n-1}\sum_{k=1}^{n-1} x_ky_k - \frac{n-1}{n}\bar{x}^{(n-1)}\bar{y}^{(n-1)} \\
&\quad + \frac{1}{n-1}\left(x_n - \frac{n-1}{n}\bar{x}^{(n-1)} - \frac{1}{n}x_n\right)\left(y_n - \frac{n-1}{n}\bar{y}^{(n-1)} - \frac{1}{n}y_n\right)
\end{aligned}
$$

where the Theorem 1 is used to rewrite the second term,

$$
\begin{aligned}
&= \frac{1}{n}\sum_{k=1}^{n-1} x_k y_k - \frac{n-1}{n}\bar{x}^{(n-1)}\bar{y}^{(n-1)} + \frac{1}{n-1}\frac{n-1}{n}\left(x_n - \bar{x}^{(n-1)}\right)\frac{n-1}{n}\left(y_n - \bar{y}^{(n-1)}\right) \\
&= \frac{1}{n}\sum_{k=1}^{n-1} x_k y_k - \frac{n-1}{n}\bar{x}^{(n-1)}\left[\bar{y}^{(n-1)} + \frac{1}{n}y_n - \frac{1}{n}\bar{y}^{(n-1)}\right] + \frac{1}{n}x_n\frac{n-1}{n}\left[y_n - \bar{y}^{(n-1)}\right] \\
&= \frac{1}{n}\sum_{k=1}^{n-1} x_k y_k - \frac{n-1}{n}\bar{x}^{(n-1)}\left[\frac{n-1}{n}\bar{y}^{(n-1)} + \frac{1}{n}y_n\right] + \frac{1}{n}x_n\left[y_n - \frac{1}{n}y_n - \frac{n-1}{n}\bar{y}^{n-1}\right]
\end{aligned}
$$

and using Theorem 1 again,

$$
\begin{aligned}
&= \frac{1}{n}\sum_{k=1}^{n-1} x_k y_k - \frac{n-1}{n}\bar{x}^{(n-1)}\bar{y}^{(n)} + \frac{1}{n}x_n y_n - \frac{1}{n}x_n\left[\frac{n-1}{n}\bar{y}^{n-1} + \frac{1}{n}y_n\right] \\
&= \frac{1}{n}\sum_{k=1}^{n} x_k y_k - \frac{n-1}{n}\bar{x}^{(n-1)}\bar{y}^{(n)} - \frac{1}{n}x_n\bar{y}^{(n)} \\
&= \frac{1}{n}\sum_{k=1}^{n} x_k y_k - \left[\frac{1}{n}x_n + \frac{n-1}{n}\bar{x}^{(n-1)}\right]\bar{y}^{(n)} \\
&= \frac{1}{n}\sum_{k=1}^{n} x_k y_k - \bar{x}^{(n)}\bar{y}^{(n)}
\end{aligned}
$$

□

The benefit of using formula (C.1) and (C.2) is that one can calculate $\overline{x_i}$ and C_{ij} on the fly, and that rounding errors, due to finite machine precision, from adding very small and very large number, are minimised.

Glossary

Glossary of common terms and abbriviations. The numbers on the far right refers to the page where the term is used.

A+A 8
: Collisions between nuclei.

ADC 30
: *A*analogue to *D*igital*C*onvertor. Apparatus to convert an analogue signal, as those from an PMT, to a digital signal. Often the term 'ADC' is also used for the actual count from the ADC apparatus.

AGS 7
: The *A*lternating *G*radient *S*ynchrotron facility at BNL.

Asymptotic freedom 3
: The freedom of quarks in the limit of high quark density, or short distances.

b 8
: (Impact parameter) The radius of overlap of two colliding nucleons. Measured in fm.

Baryon 1
: Particles made of 3 (anti)quarks, such as the proton and neutron.

BNL 7
: *B*rookhaven *N*ational *L*aboratories on Long Island, New York, USA.

BRAG 55
: *Br*ahms *G*eant simulation. A computer simulation of the BRAHMS detector. GEANT3.21 is an advanced library that tracks particles through a virtual geometry, possibly resolving interactions and decays. GEANT321 can be used to design and commission detectors, resolve acceptance and efficiency issues, and many other questions where the experimentalist has no direct access to the underlying processes.

BRAHMS 27
: *B*road *RA*nge *H*adron *M*agnetic *S*pectrometer. One of the four experiments at RHIC, designed for a large acceptance in y and $p_{\perp}$. The current work is based on data collected by this experiment.

Čerenkov detector 30
: When charge particles traverse a medium with a speed greater than the speed of light in the medium, it will emit coherent light in form of a cone. Hence, a Čerenkov detector can be used to veto particles with a low velocity, or if one measures the opening angle of the code, one can determine the velocity of the charged particle.

CERN 7

European Organisation for Nuclear Research in Geneva, Switzerland. It used to be *C*onseil *E*uropéen pour la *R*echerche *N*ucléaire, hence the odd abbreviation.

Chirality 4

The handedness of particles. Particles with their spin *aligned* to their momentum vector are said to be *right–handed*; particles with their spin *anti–aligned* are said to be *left–handed*.

Confinement 2

The property of the QCD interaction, that confines the quarks inside the hadrons.

DAQ 30

*D*ata *Acq*uisition. The apparatus and software responsible for collecting and storing data from the individual detectors, to form a full event record.

Dilepton 14

A pair of a lepton and the corresponding anti–lepton, as for example μ^- and μ^+.

Disoriented Chiral Condensates 14

Also DCC. The behaviour of the chiral condensate $\langle\psi\bar{\psi}\rangle$ when the chiral symmetry is explicitly broken, may lead to DCC.

Gauge boson 1

Force mediators, or interaction particles. 'Gauge' because they measure the force of the interaction.

Hadron 1

Particles made up of 2 or more quarks.

Lattice QCD 3

Due to the large coupling constant (strong interaction) of QCD in the limit of low energy and large distances, it is not possible to analytically calculate quantities in QCD. Therefore a method of numerical approximation where space–time is considered discrete (points in a lattice) is used; the method is called Lattice QCD.

Lepton 1

Fundamental particle in the standard model, that determines the chemical properties of atoms and molecules.

LHC 7

The future *L*arge *H*adron *C*ollider facility at CERN.

Meson 1

Particles made of a quark and an anti–quark.

Minimum bias 41

The event sample with as little as possible cuts (bias) applied.

N+N 8

Collisions between nucleons.

Nucleon 1
: The constituents of the atomic nucleus i.e., neutrons and protons.

Occupancy 30
: The occupancy for a detector element, is the probability that at least one particle hit the element in an event.

Participants 9
: Nucleons that interact during the collision.

PMT 30
: *P*hoto *M*ultiplier *T*ube. An apparatus to transform a (weak) light signal into an electronic pulse. PMTs are used in TMA, BB, TOF1, TOF2, TOFW, C1, and the RICH.

Quantum Chromodynamics 2
: The theory of the strong interactions within the standard model.

Quantum Electrodynamics 3
: The theory of electromagnetic interactions within the standard model.

Quantum Electroweakdynamics 3
: The unified theory of electromagnetic and weak interactions. The weak interaction is the one responsible for the radioactive decay of particles.

Quantum Field Theory 1
: The theory that describes the quantum particles in terms of fields

Quark 1
: Fundamental particle in the standard model from which nucleons, and hence matter, is build

Quark–Gluon Plasma 5
: The state of nuclear matter, predicted by QCD, where chiral symmetry is restored, and the temperature and/or density is so high, that the hadrons overlap, and the quarks become asymptotically free, or deconfined.

Range 59
: The range of charged particles, losing energy only through ionisation, in matter is the average length the particle must travel before it comes to a halt.

RHIC 7
: The *R*elativistic *H*eavy *I*on *C*ollider facility at BNL.

Signature 12
: An observation that lends creditability to a given theory of Nature, but does not rule out other contradictory theories. This is in contrast to real evidence, where the observation can not be easily explained without the assumption of the theory.

$\sqrt{s_{NN}}$ 85
: Centre–of-mass energy per colliding nucleon pair. $\sqrt{s} = x$ AGeV is the same as $\sqrt{s_{NN}} = x$ GeV.

Spectators 9
Nucleons that does not interact during the collision.

SPS 7
The *S*uper *P*roton *S*ynchrotron at facility CERN.

Standard Model 1
The collected believes and theories in modern day physics, that physicists work within and from.

Index